The Pennsylvania State University

The Graduate School

College of Earth and Mineral Sciences

High Frequency Transducers from PZT Films

A Thesis in

Materials Science and Engineering
by

Ioanna G. Mina

Submitted in Partial Fulfillment
of the Requirements
for the Degree of

Master of Science

May 2007

The thesis of Ioanna G. Mina was reviewed and approved* by the following:

Susan Trolier-McKinstry
Professor of Materials Science and Engineering
Thesis Adviser

Clive Randall
Professor of Materials Science and Engineering

Thomas Jackson
Professor of Electrical Engineering

Richard Tutwiler
Sr. Research Associate/Associate Professor of Acoustic Science

Gary L. Messing
Department Head of Materials Science and Engineering

*Signatures are on file in the Graduate School.

Abstract

Ultrasonic techniques for the detection of defects in engineering materials, and in imaging in medicine are widespread. Indeed, measured in monetary terms, ultrasound has now become the most used medical imaging technique, having overtaken the use of x-rays, just recently [1]. An increase in the resolution of the ultrasound system would enable detection of smaller mechanical defects in silicon integrated circuits, where these defects may be subsurface and a few microns in dimension. Similar demands exist in medicine. For example, dermatologists are increasingly interested in ultrasound images of the cross-section of the skin. Such images can be used to detect early skin cancer and many other diseases in vivo without the use of painful and scarring procedures, such as biopsy. An imaging technique with a resolution below 0.1mm is required for this purpose[1]. High frequency ultrasound devices in the 50 MHz-1 GHz range can be used for imaging tissues such as the eye, or skin, as well as for nondestructive evaluation of microelectronics devices.

This work is concerned with fabricating such a high frequency piezoelectric transducer arrays using thin film processing techniques. Because of the geometry utilized, the transmit drive voltages can be lowered substantially, so that the analog transmit and receive electronics were implemented in CMOS.

The geometry utilized for one dimensional transducer arrays is a comb - like structure with an aspect ratio of length to width of 10:1, in order to achieve isolation of the desired 31 resonance mode (see Figure i). This is a layered structure of the dielectric layer

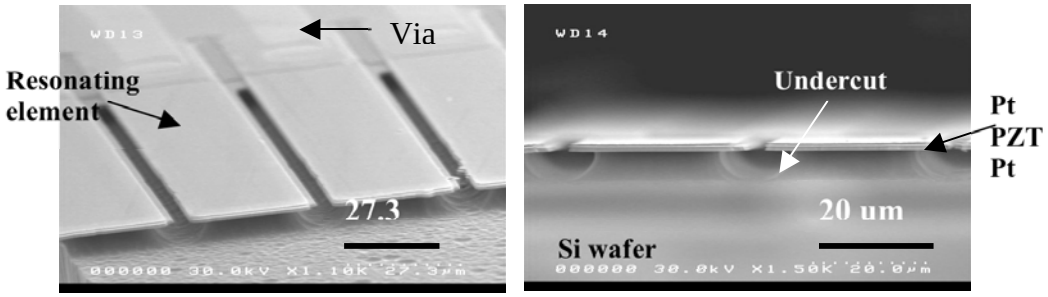

Figure i: One dimensional transducer device: the Si undercut, the vias that connect to the bottom electrodes, and the resonating elemtnts are shown in the SEM images.

(SiN_x or SiO_2), the sputtered Ti/Pt bottom electrodes, PZT, and finally the top electrode. The PZT for this structure is deposited by spin-coating a 2-Methoxyethanol based solution. The structures are partially released from the underlying substrate by etching to form a T-bar shaped transducer. Following the fabrication process, the PZT films showed a dielectric permittivity of >1000 at 1KHz, along with a low dielectric loss. The hysteresis loop measured using the RT-66 also showed good ferroelectric properties, with high remanent polarization. No clear signature of a piezoelectric resonance was detected in small signal impedance measurements as a function of frequency. Finite element modeling suggests that this is a consequence of the small expected change in impedance associated with a small resonating structure with a low Q. These structures are pioneering in their kind as far as device fabrication process for an ultrasound transducer.

Prototype two dimensional arrays were developed by coating metal pillars which are about 40 μm in height and 10 μm in diameter with a 15μm pitch with piezoelectric films (See Figure ii). The metal cores act as the inner electrodes and are addressed via electrical interconnects on the substrate. The high aspect ratio metal pillars were fabricated by electroplating Ni into patterned SU-8 molds on Si substrates. $PbZr_{0.52}Ti_{0.48}O_3$ (PZT) was chosen as the driving material, and was deposited using mist

deposition. This approach can be generalized to prepare a wide variety of high aspect ratio piezoelectric structures which are otherwise difficult to fabricate using conventional processing techniques with bulk ceramics and single crystals.

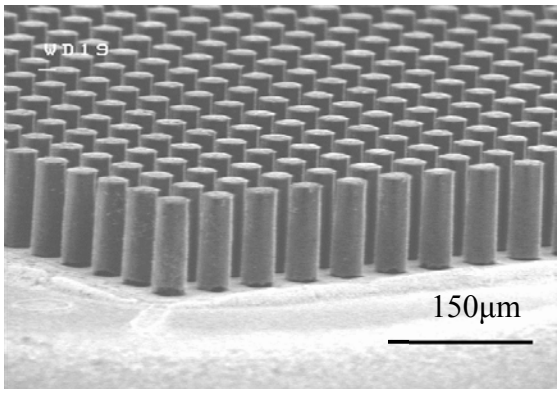

Figure ii: High aspect ratio metal structures for two dimensional ultrasound array fabrication.

In order to achieve high quality crystalline PZT on Ni pillars, the processing conditions which minimize of the formation of NiO or Pb were investigated. For this purpose Ni foils with and without barrier layers were used, and different heat treatment conditions were studied. It was found that use of a 100 nm thick Pt passivation layer on the Ni enabled perovskite PZT films to be deposited without second phases, as determined by X-ray diffraction and transmission electron microscopy.

The fabricated transducer is designed to be close-coupled to a chip with the required drive and receive circuitry. The CMOS transceiver chip designed by collaborators contains a multi-channel data acquisition system which, in conjunction with digital beamforming electronics, will enable focusing and beam steering for the ultrasound system in both transmit and receive modes. It also has analog to digital converters with on-chip buffer memory.

[1] P. A. Payne, J. V. Hatfield, A. D. Armitage, Q. X. Chen, P. J. Hicks, and N. Scales, IEEE Ultrasonics Symposium Proceedings **3,** 1523-1526 (1994).

Table of Contents

List of Tables

List of Figures

Acknowledgments

In doing the work in this thesis I was blessed to work some truly remarkable people: Rick Tutwiler, Tom Jackson, Kyusun Choi, and of course, my advisor Susan Trolier-McKinstry. During our biweekly meetings, coming from different backgrounds, each had a different approach to a subject, which sprouted many interesting discussions on underlying science of the making of the device. Listening to these discussions gave me an understanding on the many different aspects of fabricating a device. I would like to thank my advisor for bringing this brilliant group together, and for making it possible for me to be part of this team.

I would also like to thank Rick Tutwiler for spending time with me to explain to me the concepts of modeling, for his patience in answering all my questions. I am grateful to Kevin Snook for helping me with modeling and device deign and testing concepts, Trevor Clark for helping me do the TEM work, Clive Randall for helping me solve the NiO issue, Paul Moses for designing the sensitive impedance and pulse-echo measurements. I want to thank my officemates for keeping it sane during stressful times with their humor (Tanawadee and Daniel).

Lastly but most importantly, I would like to express my gratitude to my parents and my sisters, my boyfriend Andy, for being so understanding of my nagging, especially during the last two months of the thesis.

1. Literature Review: Ultrasound Technology

1.1 Introduction to Ultrasound Physics

1.1.1 Basic Ultrasound Probe

Ultrasound transducers are devices that operate at frequencies greater than that of human hearing, at approximately >20kHz [1,2,5]. These devices are used in a broad range of applications such as cleaning debris from pipes in places where it would otherwise be hard to reach: cleaning of jewelry, surgical instruments, and laboratory equipment, etc.: nondestructive testing to find flaws: and for underwater sonar transducers. In the last few years, ultrasound has become increasingly important in medicine as an inexpensive, non destructive imaging technique for the human body. Such ultrasound scans rapidly give detailed information on the condition of the organs of interest. No administration of any foreign substances into the body is required for many imaging modes, nor does ultrasound use ionizing radiation, as is in the case for X-rays.

Ultrasound imaging uses high frequency sound waves to visualize the organs and various types of tissue in the body. The sound waves (mechanical energy transmitted by pressure waves in a material medium), are generated using a pulsed transducer that transmits and receives the sound waves. The transducer can be capacitive or piezoelectric. In either case, an electrical signal is used to generate a mechanical vibration, which in turn creates the necessary sound wave. A schematic of a generic transducer is shown in Figure 1-1.

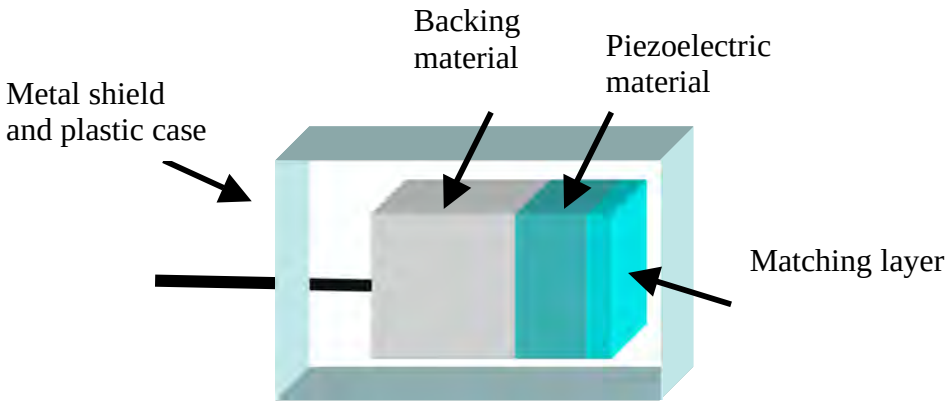

Figure 1-1: Schematic of a generic ultrasound transducer

In many cases, the transducer is made up of the piezoelectric with backing and matching layers. On excitation, sound waves are launched from both the front and back surfaces of the piezoelectric. The backing layer is used to stop the sound waves launched from the rear of the transducer from reflecting back and interfering with the incoming and outgoing signals. The matching layer improves the sound propagation from the human tissue into the probe and vice versa. This becomes necessary because the speed of sound is different in different media. The speed of sound in air is 300m/s; in water it is closer to 1500m/s. Table 1-1 shows some typical values of the speed of sound in parts of the human body.

Table 1-1: Speed of sound in various biological media [9]

Material	Speed of Sound, m/s
Air	330
Bone	4080
Blood	1570
Tissue	1540
Fat	1450

1.1.2 Interaction of Sound with Media

The sound waves that travel through tissue are longitudinal waves. Transverse waves do not travel effectively through soft tissue; they do however, propagate through some solid materials such as steel and bone [1]. For this reason transverse waves have little importance in diagnostic ultrasound (US) imaging. The diagram in Figure 1-2 shows how the sound wave propagates through a medium.

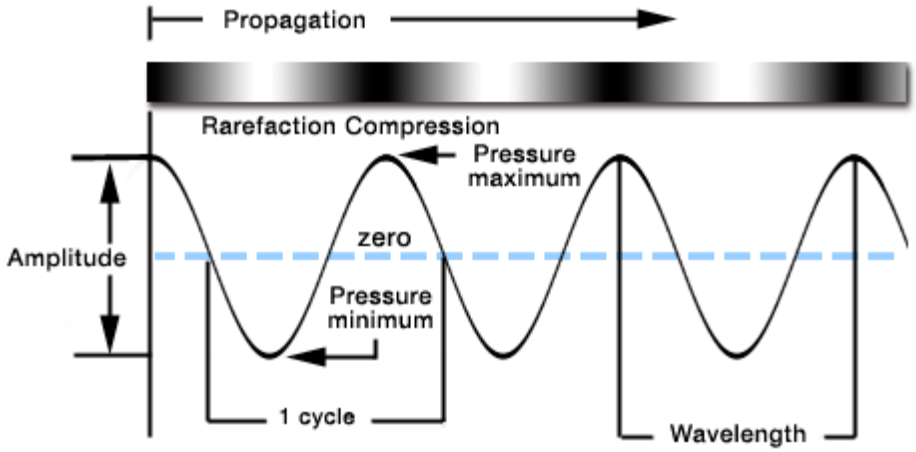

Figure 1-2: The sound wave as it propagates through a medium. The compression and rarefaction points can be represented by a sine curve [2].

The rarefaction and compression periodicity can be represented by a sine curve. The wavelength of this sine curve determines the frequency at which the particular device functions. ***Acoustic pressure level, L_p,*** measured in dB, is used to quantify the strength of a wave; this describes the changes in the density of the medium as the sound wave propagates through it in comparison to a reference sound pressure, p_0. L_p is a logarithmic measure of the rms pressure of a particular noise relative to a reference noise source, i.e.

$$L_p = 10\log_{10}\left(\frac{p^2}{p_0^2}\right) = 20\log_{10}\left(\frac{p}{p_0}\right) \qquad \textbf{Equation 1}$$

The square term in the equation comes from the relationship between pressure and acoustic intensity, ***I.***

$$I = \frac{P^2}{2\rho c}$$ **Equation 2**

where **ρ** is the density of the medium, and **c** is the speed of sound. So, the intensity of the wave increases as the square of the pressure.

The acoustic impedance, Z, is related to the speed of sound and density of medium through the relationship:

$$Z = \rho c$$ **Equation 3**

Reflection and Refraction at Interfaces: When an ultrasound wave is incident on an interface formed by two materials with two different acoustic impedances, some of the energy will be reflected and some will be transmitted. The amplitude of the reflected

$$R = \frac{P_r}{P_i} = \frac{Z_2 - Z_1}{Z_2 + Z_1}$$ **Equation 4**

wave will depend on the difference in impedance values of the two materials forming the interface. For example, consider the case of a sound beam incident on a large flat surface, as shown in Figure 1-3. The ratio of the reflected pressure amplitude to the incident is called the amplitude reflection coefficient, R, and it is given by:

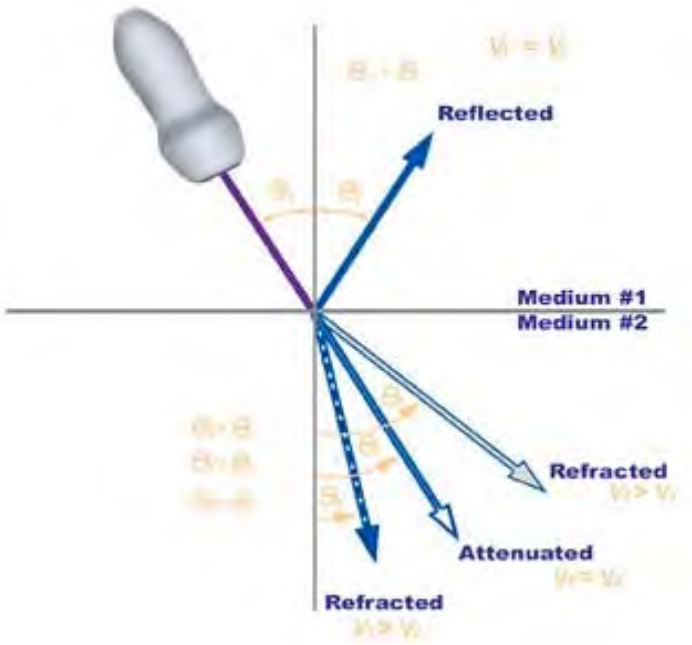

Figure 1-3: Interaction of sound with medium at interfaces [2].

A comparable expression can be described in terms of intensity:

$$\frac{I_r}{I_i} = \left(\frac{Z_2 - Z_1}{Z_2 + Z_1} \right)^2 \qquad \textbf{Equation 5}$$

Table 1-2 shows values for the acoustic impedance of elements of a typical ultrasound transducer, as well as human tissue. The large differences between lead-based piezoelectric ceramics and the human body explain the need for a soft coupling medium (e.g. the matching layer) to minimize the reflection of the pressure wave at the transducer/body interface. The filler, which is a soft polymer that can be used to create a composite with the ceramic, decreases the overall density of the composite, in this way bringing the impedance closer in value to that of the human tissue.

Table 1-2: Values of impedance of a piezoelectric ceramic, air, water, and parts of the human body.

Interface	Z, MRayls	ref
PZT (ceramic)	30	[2]
PVDF	2.7	[10]
Air	0.0004	[11]
Water	1.54	[11]
Fat	1.38	[11]
Muscle	1.70	[11]
Bone	7.8	[11]

Refraction In the case of an incident beam that strikes an interface at a non-normal angle of incidence, the transmitted beam is also refracted due to the difference in the speed of sound in the two media. The angles of incidence and refraction are connected through Snell's law.

$$\frac{\sin\vartheta_t}{\sin\vartheta_i} = \frac{c_2}{c_1}$$ **Equation 6**

So, for example, if the incident beam is at an angle of 30^o to the normal at the bone-soft tissue interface (assuming that the speeds of sound in bone and muscle are 4080m/s and 1540m/s respectively) the transmitted beam angle is 10.9^o, a 19.1^o shift. The clearest image is obtained when the incident beam is normal to the surface. However, more generally, the beam is incident at some other angle. If the sound wave is not collimated, the different angles of incidence reflect and refract by different amounts as they are transmitted, creating a distorted image.

Attenuation and Resolution There are two sources of sound beam *attenuation*: 1) reflection and scattering at interfaces, and 2) absorption. The attenuation coefficients of various tissues are shown in Table 1-3. The attenuation coefficients rise as the frequency increases, and this change depends on the medium in question. The general equation for the attenuation with frequency and depth is:

$$A = \alpha l f \qquad \textbf{Equation 7}$$

where A is the attenuation in dB, α is the attenuation coefficient in dB/MHz*cm, l is the distance from the source in cm, and f is the frequency in MHz.

Table 1-3: Attenuation coefficients of objects in the body [1]

Tissue	Attenuation at 1MHz (dB/cm)
Water	0.0002
Blood	0.18
Liver	0.5
Muscle	1.2

Note that from Equation 7 it can be deduced that as the working frequency of ultrasound increases, the attenuation also increases. This means that the depth of penetration decreases with frequency. At the same time the axial and lateral resolutions improve with increasing frequency as shown in Table 1-4. As a result there is a trade off between depth of penetration and resolution as the frequency scales up. Ultrasound systems used to image large features such as kidneys, livers, and fetuses work in the lower end of the frequency spectrum, in the 2-12MHz range. Ultrasound systems used for imaging smaller objects closer to the transducer surface (such as the interior of the eye)

currently use frequencies of 10-50MHz. The increase in resolution with frequency is extremely important in medical applications for imaging of small structures at low depths. A high resolution ultrasound system would be an invaluable tool for imaging of such structures as lymphatic structures in the breast and the eye, and skin [12]. Resolution is discussed further in section 1.3.

Table 1-4: Table 1-showing how the resolution of ultrasound scales with frequency

Center Freq. (MHz)	Wavelength, (μm)	LR (f# = 2.9) (μm)	LR (f# = 0.7) (μm)	Axial Resolution (μm)
10	154	446.6	107.8	77
30	51.3	148.9	35.9	25.7
50	30.8	89.3	21.6	15.4
100	15.4	44.7	10.78	7.7
500	3.08	8.9	2.16	1.54
1000	1.54	4.47	1.08	0.77

1.1.3 Optimization of Transducer Impedance

A piezoelectric transducer has a frequency at which the coupling coefficient is the highest, ***the resonant frequency*** [1]. For most single element ultrasound transducers, the piezoelectric element is excited in the d_{33} mode, so that the resonance frequency is determined mainly by the thickness of the element. The relationship between transducer element geometry and the piezoelectric coefficients is shown in Figure 1-4.

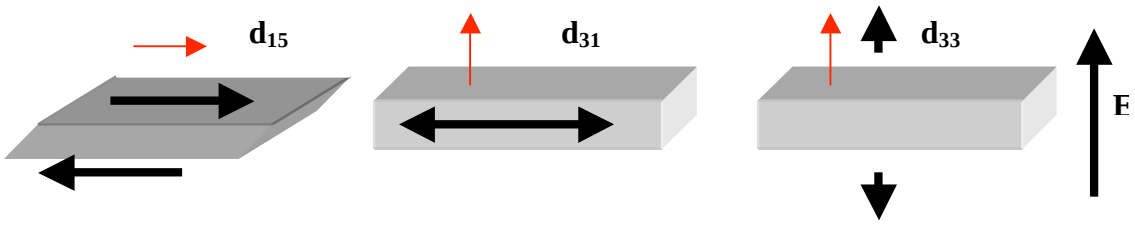

Figure 1-4: A schematic of the deflections induced by various piezoelectric coefficients. Arrows show the direction of displacement. The red arrows show the poling direction.

When the transducer is excited, the element rings at its resonant frequency; this sends a pulse of sound into the medium. For most applications, it is desirable to produce a pulse of very short duration, as this determines the axial resolution of the transducer [1]. This is optimized through damping of excess vibrations, typically via the backing layer (See Figure 1-1). In order for the backing layer to be useful in absorbing transmitted sound waves, it needs to have a similar acoustic impedance to the ceramic. This reduces the reflections at the transducer/backing layer interface so that any energy propagated in the backward direction is transmitted out of the piezoelectric.

An impedance matching layer is placed at the front of the transducer. It improves the sensitivity of the transducer to weak echoes, and provides an efficient way of transmitting the sound waves from the transducer to the tissue and vice versa by reducing reflections at the interface. A single matching layer should have a thickness of exactly one fourth of the ultrasound wavelength, and its impedance, Z_m, should be of an intermediate value between that of the ceramic and the body:

$$Z_m = \sqrt{Z_{st} * Z_t} \qquad \textbf{Equation 1}$$

where Z_t is the impedance of the ceramic, and Z_{st}, is that of the tissue. In order to achieve matching at different frequencies, several matching layers are adhered to the face of the element.

1.2 Composite Ultrasound Transducers

While piezoelectric ceramics are very efficient means of generating ultrasound waves, they have several disadvantages in biomedical transducers. These include high acoustic impedance and lower bandwidths. Several of these difficulties can be ameliorated if a piezoelectric composite is used as the transducer[8]. First, piezoelectric/polymer composites have a lower acoustic impedance than ceramics, which means that they are better impedance matched to the human body. This will decrease the problems associated with attenuation. Second, composites can be made to have much higher frequency bandwidths. Thirdly, they seem to be more sensitive than single element transducers[8].

1.2.1 Types of Ultrasound Arrays

The schematic in Figure 1-1 shows a single element transducer. Single element transducers are infrequently used in medicine except at high frequencies, (e.g. for artery and eye imaging) where array transducers are difficult to fabricate. At lower frequencies, transducer arrays are widely employed. There are three common types of arrays used for ultrasound probes, linear or curved arrays, phased arrays, and annular arrays. A schematic of each is shown in Figure 1-5

1.2.1.1 Linear and Curvilinear Arrays: In current medical ultrasound transducers, linear arrays typically consist of about 128-1024 elements. An impulse is produced by activating one or more of these elements. The beam travels perpendicular to the face of the array. Thus, the linear array produces a rectangular image field, while the curved array produces a trapezoidal image field [1]. A sub-class of the linear array is the 1.5D Array. These arrays that have many elements in one dimension, just as in a linear array, but also have a few elements in the other direction.

1.2.1.2. Phased Arrays: These typically consist of 128 elements. Individual sound pulses are produced by activating some or all of the elements in the array. The sound wave can be steered in different directions using time delay methods [1]. A more complete description of this process is described in section 1.8.

1.2.1.3 Annular Arrays: These consist of a circular "target and bull's eye" arrangement of elements. Sound waves travel along a surface which is perpendicular to the surface of the array. The beam here can be steered mechanically.

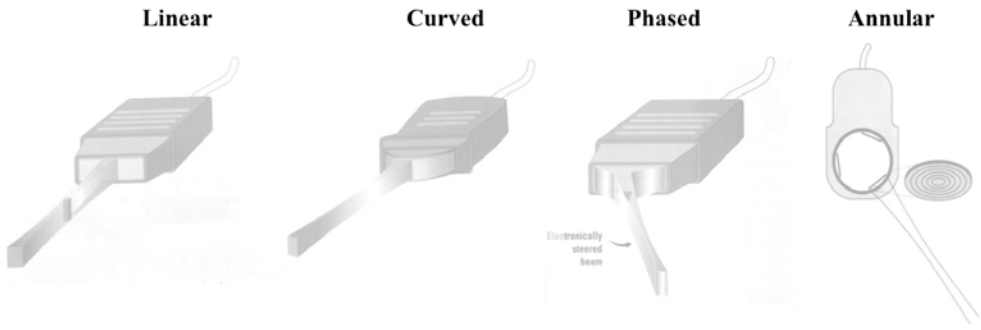

Figure 1-5: Representation of the most common types of arrays used in ultrasound transducers. From right to left: linear, curved, phased, and annular arrays [1,2]

1.3 Spatial Resolution in Ultrasonic Imaging

1.3.1 Bandwidth (BW)

A transducer emits a range of frequencies, with the center frequency being the strongest. This range of frequencies is termed the ***frequency bandwidth***, [1] and it is approximately a bell shaped curve. For a given resonance frequency, the shorter the pulse duration, the wider the frequency bandwidth. This is shown in Figure 1-6. Another measure of the frequency bandwidth is the ***transducer quality factor***, Q. The Q is defined as the ratio of the transducer center frequency to its bandwidth. For a fixed center frequency, the wider the frequency bandwidth, the lower the Q. Generally, for imaging lower Q transducers are desirable [1], because the large bandwidth means that more than a single frequency can be used, for excitation and reception.

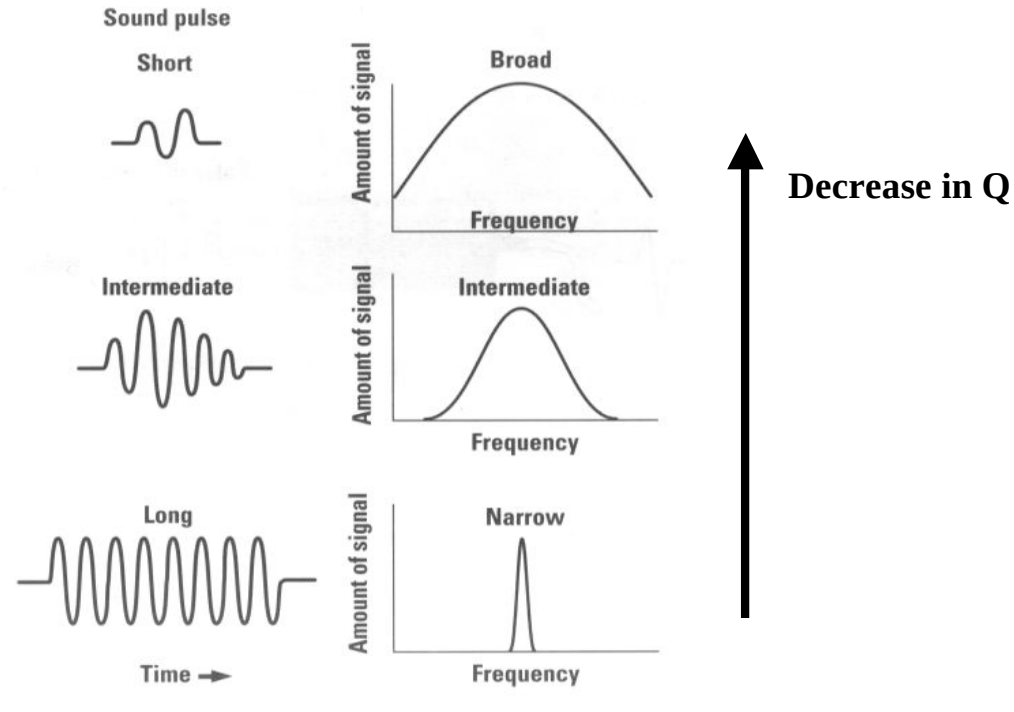

Figure 1-6: Correlation between bandwidth and pulse duration[1]

An ultrasound image is constructed using echo arrival times to determine the depth of any reflecting element. The further an object is from the transducer the longer it takes for the echo from it to come back. The beam axis position is used to determine the lateral location of reflectors.

1.3.2 Axial Resolution

Axial resolution refers to the minimum reflector spacing along the axis of an ultrasound beam that can be resolved. Axial resolution is determined by the pulse duration, PD (see Figure 1-7). The axial resolution is described by Equation 8, where c is the speed of sound, and Δf is the pulse bandwidth at a given dB level (usually -6dB). The pulse duration is the time required for the transducer "ringing" to decrease to a negligible level following each excitation [1].

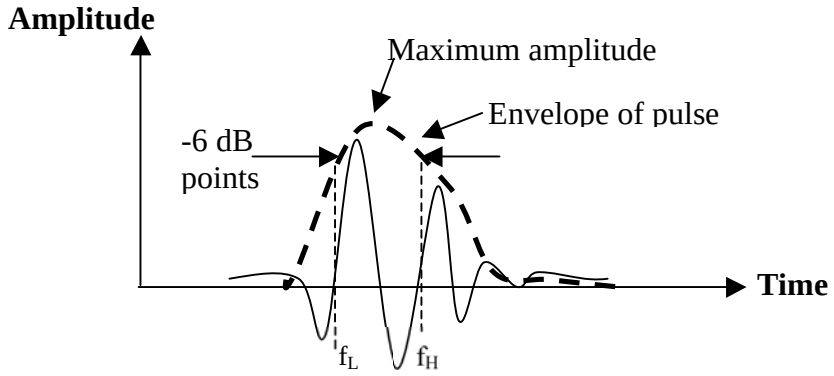

Figure 1-7: Pulse duration: Ringing down of transducer with time

The equation of lateral resolution can be represented as

$$\delta_{axial} = 2c(\ln 2)\left(\frac{1}{\pi \Delta f}\right) \qquad \textbf{Equation 9}$$

where c is the speed of sound, and $\Delta f=f_H-f_L$ at the given dB level. The pulse duration is equal to the number of cycles, Nc, in the pulse multiplied by the ultrasound wave period:

$$PD = Nc * T = \frac{Nc}{f} \qquad \textbf{Equation 10}$$

If the time difference between two signals arriving from two reflectors at different positions along the beam axis is greater than the pulse duration, then two echoes are distinguished on the display. Reduced pulse duration, for this reason, will improve the axial resolution. For a given transducer frequency, short pulses are obtained by rapidly damping the ringing of the transducer, making Nc small. The relationship between PD, axial resolution, and BW is summarized in Table 1-5:

Table 1-5: Relationship between axial resolution, pulse duration and frequency bandwidth in ultrasound [1]

PD	Axial resolution	FBW
Long	Poorer	Narrow
Short	Better	Wide

1.3.3 Lateral Resolution

The lateral resolution refers to the ability to resolve two closely spaced reflectors that are positioned perpendicular to the axis of the beam. Thus, the lateral resolution is related to the beam width. If the reflectors are far enough apart, i.e. if they are separated by more than the beam width, then they are resolved. In Figure 1-8 one can see how two

objects in the same beam path can and cannot be resolved. Lateral resolution is described by Equation 10

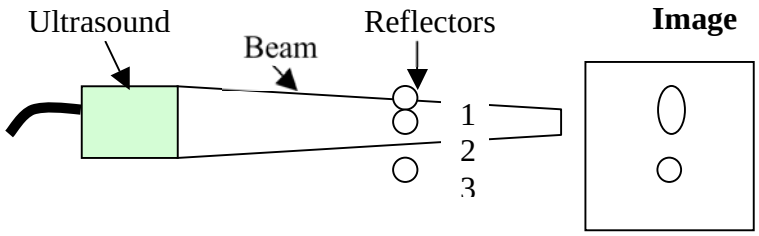

Figure 1-8: Limits of lateral resolution

where f# is the focal number, A is the aperture, f is the frequency, and F is the focus (minimum beam width).

$$\delta_{lateral} = 1.02\frac{cF}{fA} = 1.02\frac{c}{f}(f\#) \qquad \textbf{Equation 10}$$

1.3.4 Slice Thickness

Ultrasonic imaging is, in principle, capable of imaging volumes in space. However, there are often cases where a two-dimensional "slice" of tissue is useful to a clinician. This is illustrated in Figure 1-9. The slice thickness describes the thickness of the section of tissue that contributes to echoes visualized on the image. Slice thickness depends on the size of the beam perpendicular to the image plane, rather than in the image plane as in lateral resolution. This, of course, is the same as lateral resolution for circular transducers, such as discs or annular arrays. For the most part, in linear, curved, and phased arrays the slice thickness and the lateral resolution are different. This is

because the electronic focusing, discussed in the next section, for these transducers reduces only the in-plane width of the beam, i.e. the lateral resolution. The slice thickness is about the size of the scanhead up close to the array, narrows down at the focal distance, and broadens considerably beyond the focal distance [1].

1.3.4 Improving the Resolution and Slice Thickness

Figure 1-9 shows the three axes of the ultrasound beam in a 3D image. As described above, the lateral resolution depends on the beam width in the image plane. By decreasing the beam width, more closely spaced objects can be resolved. Axial resolution depends on the pulse duration. The pulse duration depends on the frequency of the transducer and on the design of the probe, i.e. the matching and backing layers. The slice thickness depends on the fixed focal length lens attached to the array. In annular arrays, or in 1.5 D and 2D arrays this distance can be decreased using electronic focusing.

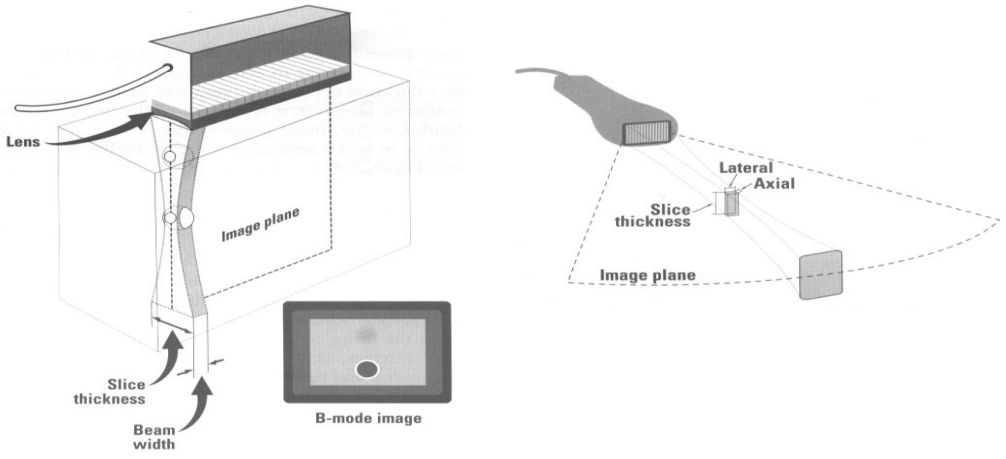

Figure 1-9: A schematic showing the image plane, the slice thickness, and the lateral and axial resolutions [1].

1.4 Beam Directivity

A transducer is often divided into a collection of point sources (Huygen sources). In the near field, the point sources interfere, adding up in some areas and cancelling in other areas. So the point-to-point variations in the near field are more prominent than in the far field beam, which is smoother and far better behaved [1].

1.4.1 Near Field Versus Far Field

The near field is also called the Fresnel zone. It is characterized by fluctuations in the amplitude from one point in the beam to another. The beam remains well collimated in the near field, even narrowing down a bit for axial points approaching the near-field length [1].

The region of the beam beyond the near field of a single element transducer is called the far-field, or Fraunhofer zone. Here the beam is smooth without the fluctuations found in the Fresnel zone (see Figure 1-10). The beam in the far field also diverges.

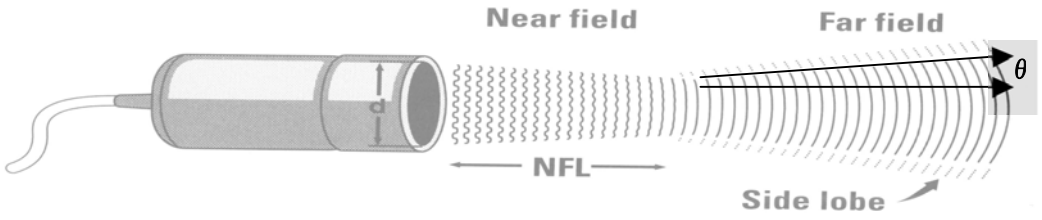

Figure 1-10: The near field and far field regions of the beam[1]

The near field length (NFL) depends on the diameter of the transducer element, d, and the wavelength, λ by [1]:

$$NFL = \frac{d^2}{4\lambda}$$ **Equation 11**

The far field divergence angle, shown by the angle θ in Figure 1-10, also depends on the wavelength and transducer size. It is given by the relationship:

$$\sin \vartheta = \frac{1.2\lambda}{d}$$ **Equation 12**

Thus, the divergence angle is less severe at higher frequencies, where the wavelength is smaller. Also, the divergence angle is less when large diameter transducers are used. In high frequency applications, the divergence angle is large due to the size of the probes (higher frequencies require smaller elements as discussed later). This restriction can be lifted through the use of large number of elements.

1.5 Focused Transducers

If an element in a transducer is small enough, it acts as a point source of the sound wave. Thus, the beam width becomes quite large far from the transducer. In order to rectify this problem, it is important to focus the ultrasonic beam. This can be done either actively (electronically) or passively (i.e. through a lens).

1.5.1 Single element focusing

In single element transducers, focusing can be done in two ways: either by using a lens or by using a curved transducer. Focusing narrows the beam profile and increases the amplitude of echoes from reflectors over a limited axial range [1]. The ***focal distance*** is the distance from the transducer to the point where the beam is the narrowest. The focal

zone corresponds to the region over which the width of the beam is less than two times the width at the focal distance (see Figure 1-11). This is the area where the lateral resolution is optimum.

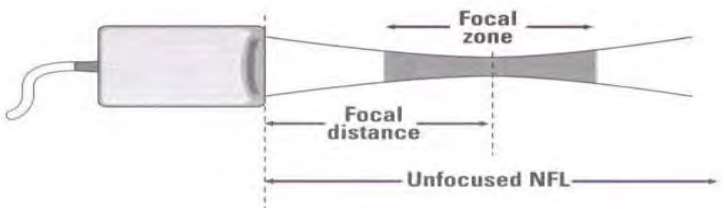

Figure 1-11: The geometry of a single element beam[1]

If d is the diameter of the transducer and F the focal distance, the beam width at the focal distance can be approximated as

$$W = \frac{1.22\lambda}{d} \qquad \textbf{Equation 12}$$

Due to this wavelength dependence, higher frequency transducers have narrower beams at the focal region than lower frequency probes. For a single element transducer, the focal distance is fixed during the manufacturing process, for transducer arrays it can be adjusted electronically.

1.5.2 Focusing in Transducer Arrays

An array transducer consists of a group of closely spaced piezoelectric elements, each with its own electrical connection to the ultrasound instrument. This enables

elements to be excited individually or in groups. The signals received by the individual element are amplified separately before being combined.

Array transducers provide two advantages:

1 Linear, curved and phased arrays enable electronic beam steering (not annular).

2 They enable electronic focusing and beam forming, providing control of the focal distance and the beam width throughout the image field.

1.6 Electronic Beam Control

With linear and curved arrays, a group of elements is involved for each beam; with sectored and annular arrays all the elements are activated for transmission and detection [1]. Arrays where the elements can be individually addressed can be used to electronically focus and steer the beam. In one-dimensional arrays the steering and focusing can be performed in two dimensions, and two-dimensional arrays can be steered and focused in three dimensions.

1.6.1 Electronic Focusing

Focusing is achieved by causing the sound beams from individual elements in an array to interfere constructively along a narrow beam path, and interfere destructively elsewhere. This is typically accomplished by manipulation of individual signals applied to different elements. When all elements in the array are excited synchronously the resulting beam is directional but unfocused. Electronic focusing is achieved by introducing time delays during the application of pulses to the individual elements as shown in Figure 1-12. The time delay acts as if the lens on the transducer has changed, in

this way changing the shape of the beam. The focal distance of an array can be varied electronically by changing the electronic delay sequence.

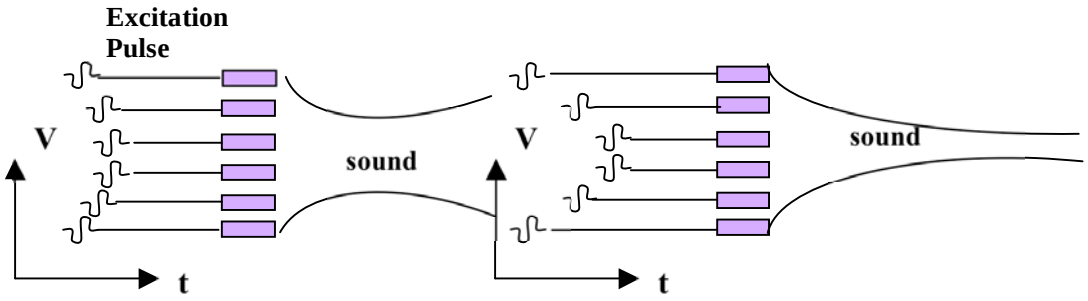

Figure 1-12: Time delayed focusing of the beam. If the time delay in addressing the outer and inner elements is longer the beam is focused at a longer distance away from the transducer, then if the time delay is shorter.

In the same manner, beam steering can also be performed. The longer delays travel a shorter path before they interfere then the shorter delays, in this way electronically steering the beam. This is shown schematically in Figure 1-13.

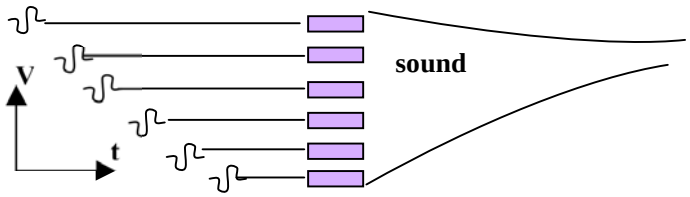

Figure 1-13: Electronic beam steering is done making sure that the sound waves arriving at the required point in space do so in phase. This is done by addressing the elements further from the focal zone first, and the elements closer to the focal zone are addressed last.

1.6.2 Multiple Transmit Focal Zones

Another feature enabled by array transducers is simultaneous ***multiple transmit focal zones***, which greatly expands the focal region of the instrument. This can be achieved by transmitting sound beams at multiple positions along the beam axis (the depth axis). For example, if there are three transmit focal zones set up by sending pulses

to three different depths, then images from three different pathlengths will be collected. During each pass, echoes are collected only from the zone corresponding to the transmit focal depth for that pass. The resulting image has optimal lateral resolution at each depth [1]. This gives a three dimensional image of the specimen.

1.6.3 Dynamic Receive Focus

Signals arriving from a single reflector may not arrive in phase to all of the individual transducer elements, due to the different distances. Thus, they may partly cancel each other out (similar to electronic focusing, see Figure 1-12). This can be corrected electronically if the signals are brought back into phase before summing. This is done by setting up appropriate time delays depending on the reflector depth [1].

In order to focus the received signals from different depths within the specimen, focusing is done dynamically. That is, when a sound pulse is launched, the receiving focal distance is first set up to receive signals from near objects (since they will be returning first), as the time increases and the echoes from further objects begin to arrive, the focal distance is automatically changed by electronically changing the focus of the array to encounter deeper reflector echoes. The result is an extended focal depth that is much greater than for a single element transducer [1].

1.6.4 Dynamic Aperture

In order to keep the lateral resolution nearly constant over the entire image region, variations in the beam width along the axis can be minimized in array transducers using the ***dynamic aperture*** concept. For a fixed aperture size, the beam width varies with depth. In an array transducer, the size of the aperture can be manipulated by changing the

number of elements activated. A small receiving aperture is applied shortly after the ultrasound pulse is launched into the tissue; as the echoes return from deeper structures the number of elements used to collect the signal is increased, thus increasing the aperture [1].

1.7 Unwanted Radiation

1.7.1 Side lobes

A side lobe is energy in the far field that is not part of the main beam. If they are strong, side lobes degrade lateral resolution, as ghosts are created in the image. Figure 1-14 and Figure 1-15 show the geometry of the main beam and side lobes at different angles.

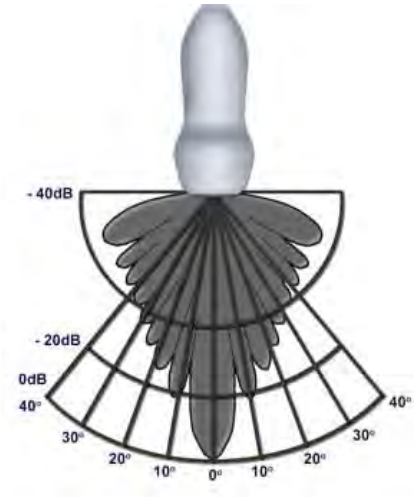

Figure 1-14: The wave front generated by a transducer [9]

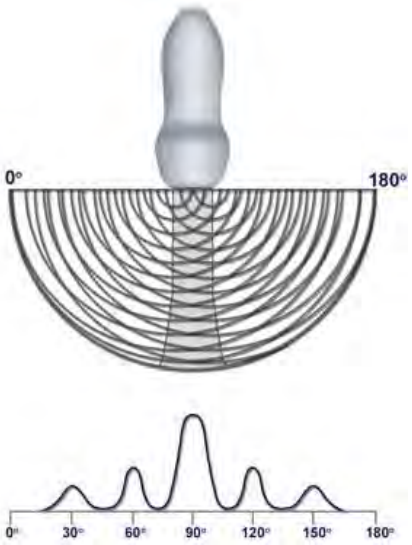

Figure 1-15: Sound intensity generation and side lobes generated by a transducer [9].

A single element transducer producing continuous sound has side lobes that are about 14% of the main beam [1]. Side lobes of this strength are not good in most ultrasound studies because they significantly reduce resolution [1]. This can be avoided if the transducer is pulsed rather than operated continuously. In this case side lobes for different frequencies in the pulse spectrum appear at different angles, cancelling each other out. Further reduction of the side lobes can be done by strengthening the beam in the center of the transducer and weakening it on the sides. This is called ***apodization***. With transducer arrays apodization can be performed through beam forming [1].

1.7.2 Grating Lobes

With arrays, additional grating lobes and clutter may degrade the image quality. Grating lobes result from the division of the transducer into smaller individual elements that are regularly spaced across the aperture. The distance between each element and the central lobe depends on the position of the element; in this way the elements in the center of the array are closer to the central lobe then the elements further away from the center.

In this case, all the elements constructively interfere to produce the central fringe. However, there are other positions on the angle axis at which there will be interference maxima, and the angle at which they emerge from the transducer depends on the frequency and element spacing through [13]

$$\left|\frac{df(\sin\psi - \sin\psi_o)}{c}\right| = i \qquad \textbf{Equation 13}$$

where f is the frequency, c is the speed of sound, and d is the element spacing. The first maximum happens when $|\sin\psi - \sin\psi_o| = 0$, which corresponds to the central maximum. However, other solutions occur at $df = \frac{c}{2}$, with the second maximum being at ψ and ψ_0 at angles $\pm 90^0$. As the operating frequency of the transducer increases with the same spacing, d, the grating lobes will occur at smaller values of $|\sin\psi - \sin\psi_o|$, and closer to the steering angle[13]. For this reason, as the frequency increases in order to avoid grating lobes the element spacing must be as small as possible. This necessitates spacing the elements at ½ wavelength or less [1].

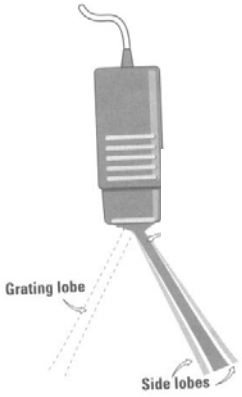

Figure 1-16: Grating lobes on transducers [1]

In the case where the element pitch is more than λ/2, beam steering is still possible, however, the steering angle will be limited up to the angles where the first grating lobes are situated. The steering angle will increase as the pitch decreases.

1.8 Ultrasound Probe Modeling

Transducers form the heart of the ultrasound system -- converting the electrical driving pulse into an acoustic beam that is projected into the soft tissues of the human body, and then detecting the weak echoes reflected by organ boundaries and internal structures. The piezoelectric must meet severe demands -- interfacing with the drive/receive electronics, performing the electromechanical energy conversion, projecting the strong acoustic pulse into tissue, and gathering the weak echoes[14]. In each of these roles, the piezoelectric composite allows the device engineer to tailor the material properties -- adjusting the electrical impedance to that of the electronic chain, enhancing the electromechanical coupling, moving the acoustic impedance close to that of tissue, and shaping the transducer to focus the beam. A single material design does not optimize all the required properties simultaneously [8]. The next section discusses two important aspects that need to be considered when designing an ultrasound transducer - transducer design and materials selection.

1.8.1 Piezoelectric Composites

In the majority of the currently available high frequency ultrasound systems the probe is a single element transducer. This is mainly due to the complexity of the task of making and contacting a high frequency array of elements because of the decrease in the size of the element in comparison to the low frequency probes. Despite this, composites

offer several key advantages over single element probes. In this section some those issues are discussed.

Composites offer several key advantages -- high electromechanical coupling constant, higher sensitivity, and an acoustic impedance close to that of tissue. There are several types of composites, as shown in Figure 1-17 [15]. Of these, the most important for medical transducer applications are the 1-3 composites, such as the PZT rods in a polymer, and the 2-2 composites, the layered structures. Figure 1-18hows the variation of the material properties important to the performance of the thickness-mode transducers as a function of ceramic volume fraction in 1-3 composites [14]. Critical properties include the thickness mode electromechanical coupling constant and the specific acoustic impedance. These curves are based on a simple physical model of the thickness-mode oscillations in piezocomposite plates [8].

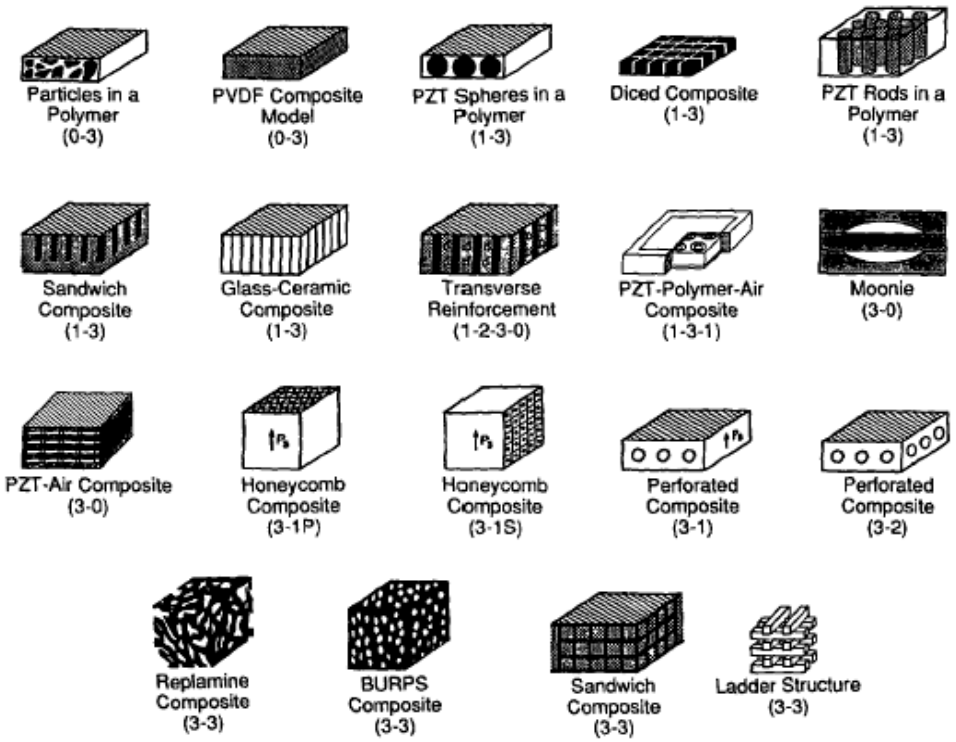

Figure 1-17: Schematic diagram of various piezoelectric-polymer composites [15]

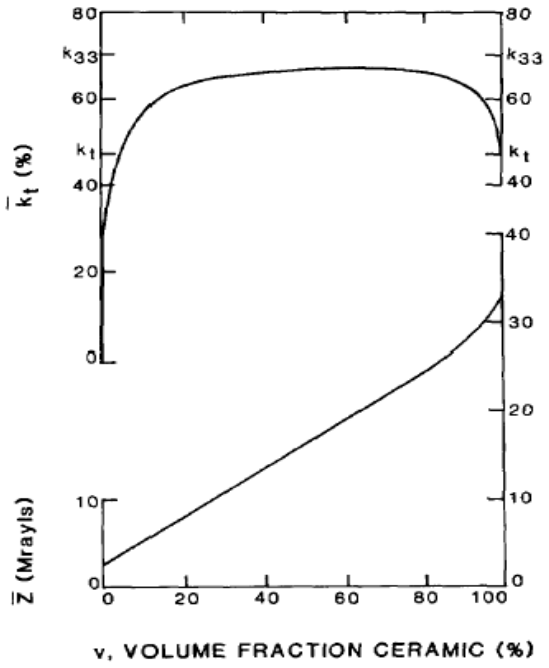

Figure 1-18: Variation of the composite's thickness-mode electromechanical coupling, k_t and specific acoustic impedance. Z, with the ceramic volume fraction in a 1-3 piezoelectric/polymer composite [14]

It is not surprising to see that the impedance of the piezoelectric-polymer composite is lower than that of the ceramic alone, due to the decrease in the density of the composite in comparison to that of the ceramic (see Figure 1-18). Notice, however, that according to this graph, the coupling coefficient of the ceramic-polymer composite is higher than that of the ceramic. This, at first, may seem counterintuitive; as you decrease the amount of active material that performs the energy conversion, it might be expected that the energy conversion is decreased. However, because a ceramic is partially clamped by its surroundings, a soft polymer matrix provides a more compliant environment for the piezoelectric. This partial relief of the lateral clamping accounts for the increased thickness mode electromechanical coupling constant of a properly designed

piezocomposite. Clearly, this argument breaks down in the high power limit when the material is driven to saturation [8].

The second advantage of the composites over the single element ceramics is the increased sensitivity. When operating in the hydrostatic mode, i.e. when the incident stress is equal on all sides, the tensor coefficients are represented as $\mathbf{d_h = d_{33} + 2d_{31}}$ and $\mathbf{g_h = g_{33} + 2g_{31}}$. A figure-of-merit, the $\mathbf{d_h * g_h}$ product, is often reported as a measure of the sensing capability of the piezoelectric element or to compare different hydrophone materials[14]. The sensitivity of a piezoelectric is taken to be equal to the open circuit voltage that it generates due to an applied stress, or g*t, where g is the relevant piezoelectric voltage tensor coefficient and t is the thickness of the piezoelectric element. The sensitivity needs to be sufficiently high so that the generated signal can be detected above the background noise. In practice, the generated signal is small and has to be enhanced by an appropriate charge or voltage amplifier. The sensitivity is maximized when the g coefficient is maximized. The g coefficient is related to the d coefficient through the dielectric constant, K, as follows:

$$g = \frac{d}{K\varepsilon_0} \qquad \textbf{Equation 14}$$

where ε_o is the permittivity of free space. Typically, a large dielectric constant, or capacitance, is desirable for sensors in order to overcome the load associated with the cables[14]. Unfortunately, an increase in dielectric constant results in a lower voltage coefficient, as seen in Equation 14.

It is important to note that in monolithic ceramics, $d_{31}= d_{32}$. For the various PZT compositions, $d_{33} \sim -2d_{31,}$ therefore, d_h is nearly zero[14]. In a properly designed composite the d_{31} and the d_{33} are decoupled. Since the ε_{33} of PZT is much greater than that of the polymer, the ε_{33} of the 1-3 composite becomes the ε_{33} of PZT times the volume fraction of PZT. This lowers the overall dielectric constant of the composite phase with respect to the PZT, increasing the g_h coefficient. This approach is described in Klicker et al[16], and is based on the assumption that the dielectric constant and piezoelectric coefficients of the polymer are negligible in comparison to those of PZT.

The third advantage of the composites over single element transducers is the lower acoustic impedance, which matches better to the impedance of the body. Recalling that a material's acoustic impedance is the square root of the product of its density and elastic stiffness provides intuitive insight into the improvements achieved by replacing stiff, heavy ceramic by a light, soft polymer. The acoustic match to tissue (1.5 Mrayls) of the typical piezoceramic (20 -30 Mrayls) is thus significantly improved by forming a composite structure [8]. Too high of a volume fraction of a polymer, however, will ultimately result is a lowered coupling coefficient, which would decrease the sensitivity and shrink the bandwidth. Therefore, care must be taken in determining the optimum amounts of ceramic and polymer [14].Furthermore, by isolating the elements of transducer with the soft polymer the crosstalk can be substantially reduced. It was shown that this can be done even by patterning the electrodes alone without cutting the continuous sheet of composite [17]. Figure 1-19 provides a schematic representation of a linear array formed in this fashion by Smith et al [17]. The same figure compares the measured continuous

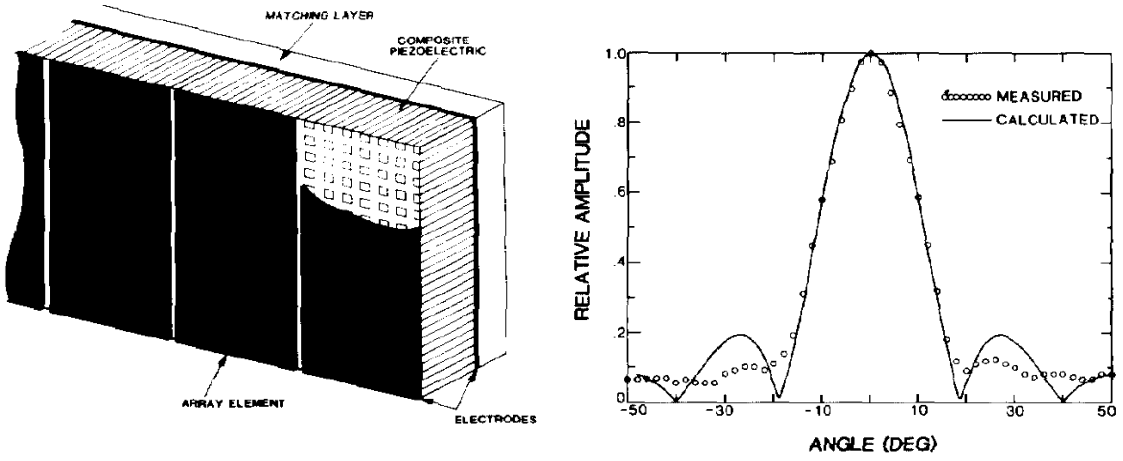

Figure 1-19: Acoustic crosstalk in an undiced array. a) schematic of a linear array with elements defined by the electrodes, b) measured CW radiation patternfrom a single element of the array (circles) and calculated pattern of an isolated element (solid) [1,8]

wave (CW) radiation pattern of a single element of an undiced linear array to the theoretical value for an isolated element. In addition to the excellent interelement isolation shown by the agreement with theory for the main lobe, the side lobes are even further reduced below the theoretically expected value. This is due to good design [8].

In an undiced array there is refraction at the interfaces between the high acoustic speed piezoelectric and the lower acoustic speed matching layer and again at the matching layer tissue interface. The effect of this refraction is to concentrate the acoustic beam toward the normal to the interface. By proper choice of the velocities for the piezoelectric and the matching layer, this Snell's law effect can be designed to fall just outside the main acoustic lobe, thus suppressing unwanted side lobes [8].

1.8.2 Electronically Focused Arrays

Array transducers are desired for several reasons, including clinical convenience, increased frame rates, improved real-time blood flow measurement, and the capability to

focus the beam dynamically. If the elements can individually be contacted and addressed with a specified time delay, the beam can be electronically focused and steered. In one dimensional linear arrays the focusing can be done in two dimensions and with a two dimensional array in three dimensions.

One of the most heavily studied piezocomposites is the "rods in a polymer" 1-3 composite. Early samples were produced by forming PZT into long cylindrical rods, aligning those ceramic rods parallel to each other in a fixture, casting a polymer around them, and then slicing off disks perpendicular to the rods. This method is effective for making samples with rod diameters of about two hundred microns or more [8]. Finer spatial scales are increasingly difficult using this method.

The dice-and-fill technique is perhaps the most widespread fabrication method for materials used in medical ultrasonic applications. Deep grooves are cut into a solid ceramic block, a polymer is cast into these grooves, and the resulting composite disk is sliced off the ceramic base. Mechanical dicing saws are quite effective for rod scales ranging down to fifty microns [8]. Pushing below fifty micron becomes increasingly difficult, as the rods are quite fragile, and wear on thin saw blades becomes an important factor [8]. Finer spatial scales can be achieved using laser machining to cut the grooves. Despite the associated higher costs, this is a viable approach to reach scales of ten microns, perhaps lower [8]. A cut-fill-cut-fill strategy alleviates some of the problems with rod fragility at the cost of making the second cut through a ceramic-polymer combination more challenging [8]. Slicing the formed composite off its ceramic base and polishing to a final thickness also presents problems in machining a brittle ceramic and soft polymer simultaneously [8].

1.9 Material Selection

Transducers can be self focusing single elements, or they can have multiple elements in the form of 1, 1.5 and 2 dimensional arrays where focusing and beam steering can be achieved electronically. For proper beam steering, arrays require that the element pitch be on the order of the half the wavelength of the ultrasound in the propagating medium. The speed of sound in water is 1500 m/sec and is close to that of human tissue (see Table 1-1). Therefore, a pitch of 15-5μm is required for a 50-150 MHz array respectively.

Dielectric constant is another important parameter to consider during transducer design, as it is related to the capacitance and it directly affects the impedance matching with the electronics. The relative dielectric constant may be measured at constant (zero) stress and is called the free dielectric constant, ε^T. It can also be measured at constant (zero) strain, the so called clamped dielectric constant, ε^S. The free and clamped dielectric constants are related through [2]:

$$\varepsilon^S = \varepsilon^T (1 - K^2) \qquad \textbf{Equation 15}$$

where K is the electromechanical coupling coefficient[2]. In turn the dielectric constant, or relative permittivity, ε, (whether it is free or clamped will depend on the frequency) is related to the capacitance through

$$C = \frac{\varepsilon \varepsilon_0 A}{t} \qquad \textbf{Equation 16}$$

where ε_0=8.85 x 10^{-12}F/m is the permittivity of free space, A, is the area of a capacitor plates, and t is the thickness. The impedance of a capacitor is equal to

$$Z_c = \frac{1}{j\omega C}$$ **Equation 17**

Since the elements of an array are much smaller than a single element transducer, the dielectric constant of the piezoelectric material becomes more important if the electrical matching of the array elements is to be optimized. For this reason, a high permittivity material should be used to fabricate the array [18]. Possible materials for transducers include bulk polycrystalline ceramics (e.g. PZT[19]) single crystal ceramics e.g: lithium niobate ($LiNbO_3$[20]) relaxor materials PMN-PT (Lead magnesium niobate-lead titanate[21]), PVDF (polyvinyldine fluoride [22]) polymers, ceramic/polymer composites [23] and sol gel films [24]. Some materials that are commonly used for transducer fabrication and their properties are listed in Table 1-6

Proper material selection is of primary importance in designing and fabricating an ultrasound probe. The desired properties will depend on the choice of transducer geometry, whether it is a single element or an array probe. Single element transducers with a larger area to thickness ratio require a piezoelectric material with a lower dielectric constant for proper electrical impedance matching, while array transducers require a much higher dielectric constant because of the reduced area of an individual element. In both cases high electromechanical coupling coefficients, low mechanical and dielectric losses, and a low acoustic impedance are desirable [19].

A number of different materials have been characterized for single element high frequency transducers. PVDF and co-polymer polyvinyldine fluoride-trifluoroethylene (PVDF-TrFE) have been demonstrated to work quite well at frequencies up to 100 MHz [19,25]. Although the electromechanical coupling of these materials is fairly low relative to

piezoelectric ceramic materials, they do have a number of advantages. In particular, their low acoustic impedance matches well to tissue and their low dielectric constant allows for a larger transducer area for a match to 50 ohm electronics. The larger area results in better lateral resolution in single elements [19].

Piezoelectric materials for multi-element arrays have different requirements from single element transducers. Because of the small area relative to the thickness, array transducers require a high dielectric constant material for electrical impedance matching to the electronics. This effectively excludes piezoelectric polymers such as PVDF, the nylon materials, and the $PbTiO_3$ ceramics [19] (See Table 1-6)

Table 1-6: Material properties comparison chart:

Single crystal	d_{33},	K_t	K_{33}	ε_r^T	Z, MRayls	Ref.
PZN9.5%PT		0.64	0.83	1550	22	[26]
PMN35%PT			0.93	4540	28	[26]
$LiNbO_3$	6	0.49	0.16	30		[10,27]
$KNbO_3$	62	0.68	0.75	92	34.7	[28]
Ceramics						
PZT 5-H	1400	0.50	0.73	3640	30	[26]
PZT-8	220	0.48	0.70	1000	30	[2,29]
$PbTiO_3$		0.49		200		[10]
$Pb(Zr_{0.52}Ti_{0.48})O_3$	220		0.67	800		[30]
$Pb(Mg_{1/3}Nb_{2/3})O_3$-33PT	690	0.5-0.63	0.73	5000		[29,30]
Films						
PZT 52/48 (1-3um)	60-130	≤0.53		300-1300		[31,32]
ZnO	5.9			10.9		[31]
AlN	3.9			10.5		[31]
Polymers						
PVDF	20	0.14	0.12	6.5	2.7	[10]

1.10 Ferroelectrics

Most of the key piezoelectric materials for ultrasound applications are ferroelectric. Ferroelectricity is observed in crystals whose direction of spontaneous polarization can be reoriented between crystallographically defined states by the application of an external electrical field (~10^6-10^8 V/m) [33,34]. This property is observed in some crystals that have a polar axis. A region of the material in which the spontaneous polarization is uniform (or at least nearly so) is referred to as a domain. Because polarization switching occurs via domain wall motion, the measured polarization is a hysteretic function of the electric field (See Figure 1-20). Most ferroelectrics have a

transition temperature, called the Curie point, T_c, above which the crystal does not exhibit ferroelectricity. Near the Curie point, the dielectric, elastic, optical, and thermal constants show anomalous behavior [35]. This is due to the distortion in the crystal as the phase structure changes [34]. All ferroelectrics are also piezoelectric. Piezoelectricity is a phenomenon exhibited by some noncentrocymmetric crystals whereby an electric polarization is induced in the materials upon the application of stress (direct effect). Conversely, it is the development of an induced strain which is directly proportional to an applied electric field (converse effect) [33].

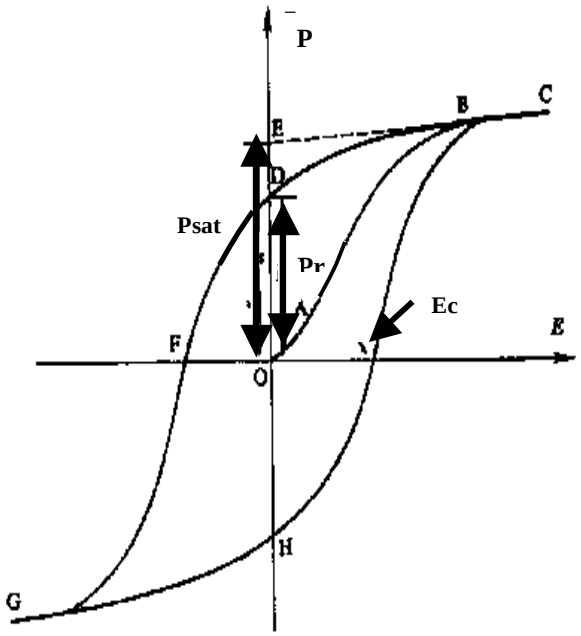

E_c- Coercive field
P_r- Remanent polarization
P_{sat}- Saturation polarization

Figure 1-20: The polarization vs. electric field hysteresis of a ferroelectric material

Piezoelectricity exists in some naturally occurring crystals such as quartz and Rochelle salt, and it can be induced in polymers such as some nylons and copolymers of vinylidene Fluoride (VDF) with trifluoroethylene (TrFE), or with tetrafluoroethylene (TeFE). However, for many commercial applications, polycrystalline ferroelectric

ceramics such as lead zirconate titanate (PZT) are preferred. Compared to single crystals, ceramics offer the advantage of high strength and ease of fabrication in general, especially into complex shapes and large area pieces.

Ferroelectric oxides with the perovskite, tungsten bronze, pyrochlore, and bismuth titanate layer structures generally have high dielectric constants and high electromechanical coupling coefficients. In addition, all contain corner-linked oxygen octahedral networks centered on Ti^{4+}, Nb^{5+}, or other d^0 ions. These transition-metal ions are highly polarizable and are responsible for the ferroelectric effect and the high permittivity and piezoelectric constants in some materials. With reference to the periodic table, there are two major groups of active ions, both of which are near electronic "crossover" points where different types of atomic orbitals are comparable in energy and where hybrid bond formation is prevalent. [33]. The first group, Ti^{4+}, Nb^{5+}, and W^{6+}, consists of d^0 ions octahedrally coordinated to oxygen. For Ti^{4+}, the electronic crossover involves the 3d, 4s, and 4p orbitals, which combine with the sigma and pi orbitals of its six oxygen neighbors to form the $(TiO_6)^{8-}$ complex [33]. The bond energy of the complex can be lowered by distorting the octahedron to a lower symmetry [33]. This leads to permanent molecular dipole moments, ferroelectricity, large dielectric constants, and piezoelectricity. A second group of active elements contributing to polar distortions in ceramic dielectrics are the lone-pair ions having two electrons outside a closed shell in an asymmetric hybrid orbital [33]. Among oxides, the most important of these lone-pair ions are Pb^{2+} and Bi^{3+}, which are involved in a number of ferroelectrics ($PbTiO_3$, $Bi_4Ti_3O_{12}$, $PbNb_2O_6$) with high Curie temperatures. In many of these compounds, Pb and Bi have

asymmetric coordination polyhedra with oxygen and therefore contribute to the spontaneous polarization [33].

Lead zirconate titanate, $Pb(Zr,Ti)O_3$ Lead zirconate titanate belongs to the class of perovskites (see Figure 1-21), one of the most important structures exhibiting the ferroelectric effect. Lead zirconate titanate (PZT) is a binary solid solution of $PbTiO_3$ and $PbZrO_3$, both of which have perovskite-like structures [35]. Both lead and oxygen ions

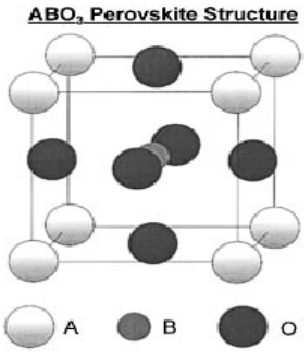

A- Pb is 12 coordinated

B- Zr, Ti are randomly distributed on the octahedral sites

O- is 6 coordinated

Figure 1-21: Perovskite structure in PZT [3]

have radii of about 1.4 Å. Together they make up a cubic array, having a lattice parameter of about 4 Å [33]. Octahedrally coordinated titanium or zirconium ions randomly occupy the lattice position near the center of the unit cell, oxygen atoms are near the four corners, and the lead atoms are positioned on the corners of the cell (see Figure 1-21).

$PbTiO_3$ has a tetragonal symmetry, and is a ferroelectric below T_c, and $PbZrO_3$ has an orthorhombic symmetry, and is an antiferroelectric below T_c. The phase diagram for PZT is shown in Figure 1-22. At high temperatures PZT exhibits the cubic perovskite structure, and is a paraelectric. On cooling below T_c, for most Zr/Ti ratios, it forms a

ferroelectric structure which is either a rhombohedral phase with the spontaneous polarization oriented in the

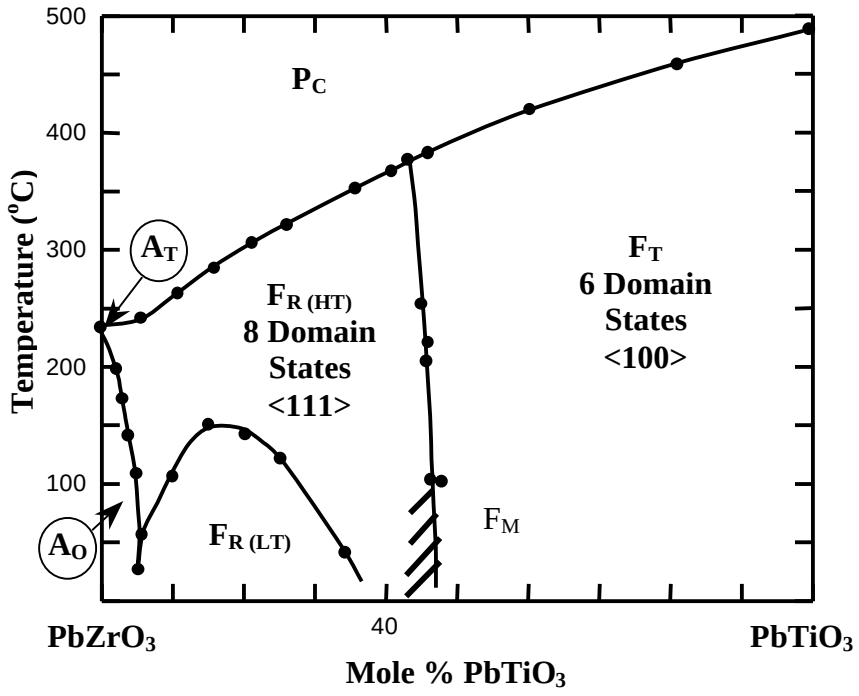

Figure 1-22: The PZT phase diagram (Jaffe et al.) showing the MPB for the $PbZrO_3$ - $PbTiO_3$ system[2,6,72,6,7]

<111> orientation, or a tetragonal phase with the polarization aligned in the <001> directions. At compositions with Zr/Ti >95/5 the composition becomes antiferroelectric with a double hysteresis loop. On the morphotropic phase boundary, MPB, which has a Zr/Ti composition of 52/48, upon cooling to room temperature PZT undergoes a displacive phase transition with atomic displacements of about 0.1 Å [33]. At this composition poling is comparatively easy due to the ability of the spontaneous polarization to switch between 14 available orientations of the <111> and <100>[35]. Moreover, at the morphotropic phase boundary, the polarizability of the material is

unusually high (Figure 1-23), leading to the maxima in the dielectric, piezoelectric, and compliance constants. Noheda et al. have suggested the presence of a low temperature monoclinic phase on the MPB which may also influence both the poling efficiency and the polarizability [7].

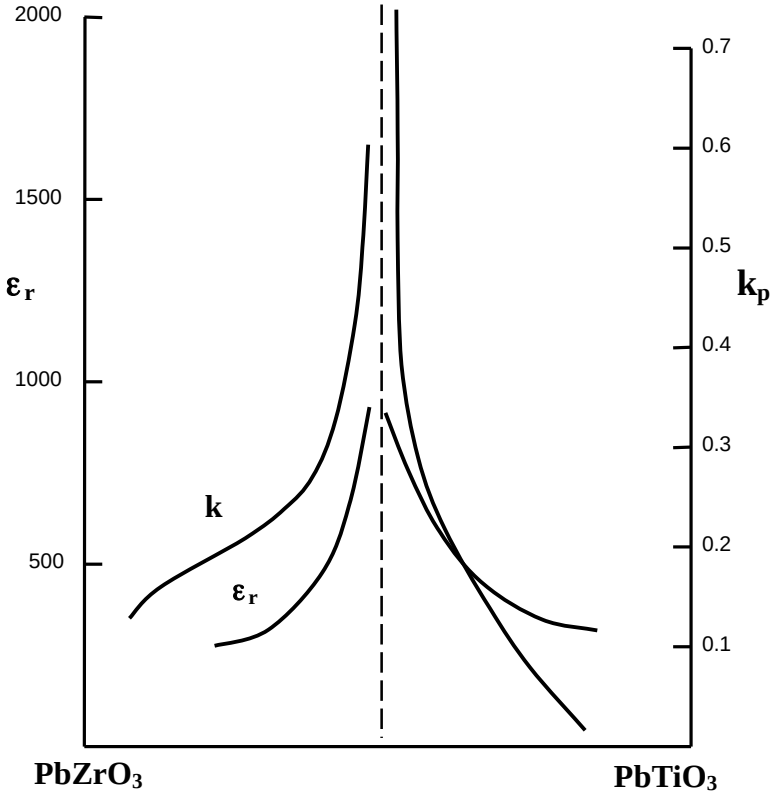

Figure 1-23: The effect of composition on the dielectric constant and electromechanical coupling factor k_p in PZT ceramics. After [2]

Polycrystalline ferroelectric ceramics (Curie point group ∞m) such as PZT initially contain numerous domains within each grain. These domains form upon cooling through the Curie temperature in order to minimize the total elastic and electrical energy in the ceramic [36]. Thus, polycrystalline ferroelectrics do not exhibit the piezoelectric effect spontaneously. Piezoelectricity can be induced, however, by applying a dc electric field larger than the saturation field but below the breakdown field. This produces a net

polarization within the ceramic or film. When the electric field is removed some of the domains will depolarize, but the majority of the domains remain aligned resulting in remanent polarization in the material [36].

1.11 The Chemical Solution Method for Transducer Fabrication

Conventionally, ultrasound transducers are fabricated by lapping and thinning bulk ceramics or single crystals to the desired thickness, and then mechanically dicing them into elements. A 1-3 piezocomposite operating at 50MHz must be on the order of 30μm in thickness[37], with ceramic pillars less then 10μm wide with a kerf below 5 microns in order to obey the $<1/\lambda$ rule for beam steering. Dice-and-fill cannot be used to make such structures because the saw blades are limited to around 15 microns minimum thickness[37]. Relaxing these design constraints removes the ability to focus electronically[37].

Among the alternative methods for production of high frequency transducers are those based on lithography and etching of bulk materials, and those based on thin and thick film methods for achieving the correct thickness.

In terms of utilizing thin films to achieve the target thickness range, chemical solution deposition (CSD) methods for depositing piezoelectric films have been extensively pursued. CSD is widely used for the deposition of varying thickness, dense complex oxide films [18,38]. The transducer elements can later be defined using lithography techniques. In most cases, the PZT thickness that can be achieved on Si substrates using CSD is limited to about 10 microns, unless some porosity is introduced into the films [39,40]. Thus, dense films are typically limited to frequencies of >75MHz, unless mass loading is

used to decrease the resonance frequency [41]. It is encouraging that strong piezoelectric performance can be achieved [42].

Several groups have utilized films as a mean to fabricate high frequency ultrasound transducers. Zhihong et al. [43] prepared thick PZT films by adding powder to a sol-gel solution of PZT. As a result they could spin coat a 7μm film with 10 deposition steps. One of the main problems associated with this approach is the high percent of porosity in the resulting films, which degrades the piezoelectric and dielectric properties, in comparison to a conventional sol-gel process. Permittivities of 800 were obtained only after presintering powders and heat treating the films at 800 °C, suggesting that the either the densification was incomplete, or that there were low dielectric constant barrier layers that developed. In contrast, sol-gel films can be densified at temperatures as low as 600 °C with a resulting dielectric constant of over 1000. Lucaks et al. [42] also used a composite sol-gel method. The dielectric constant of these composite films was 220 (again due to low density), and the resulting impedance was 10-15 Ohms at the center frequency. Had the dielectric constant of the films been higher, the films would have been better impedance matched to the 50 Ohm electronics. Despite this, the transducers were functional in the frequency range of 70-160MHz with a minimum insertion loss of -46dB at 72MHz. Array transducers were produced by the same group [44] using a laser to dice the films. Kline-Schoder et al. [45,46] used physical vapor deposition to grow PZT films with a thickness of 9μm. The design frequency of the device is >75MHz. The active element and electrodes in this construction were layered to create a multilayer "sandwich".

Other groups have used alternative materials to fabricate high frequency transducers. For example, Payne et al. [47] used piezoelectric polymers. Ferroelectric polymers, such as PVDF, have the advantage of high flexibility and low acoustic impedance, low coupling coefficients, and diminished dielectric constant [48]. Ito et al. [49] use rf magnetron sputtering of ZnO to prepare films that were 10 μm thick. Grooves were etched to create the arrays using an anisotropic etchant that preferentially etches the c-plane of ZnO. The resulting array resonated at 100MHz. Chapter 1.13 describes in more detail the literature on the high frequency ultrasound technology.

The work in this thesis focused on dense PZT films deposited on larger structures in order to increase the resonance frequency. In the next section, CSD procedures for the production of dense PZT films are discussed.

1.11.1 CSD of PZT Films

The fabrication of thin PZT films via sol-gel involves four basic steps: (i) synthesis of the precursor solution; (ii) deposition, (iii) pyrolysis of organic species (typically 300-400 °C), and (iv) higher temperature heat treatment for densification and crystallization of the coating into the desired oxide phase (600-1100 °C) [7].

The choice of the starting reagents of the solution determines many of the properties of the solution itself, as well as some of the properties of the final film. Some of the things that need to be taken into account are the extent of oligamerization and cation interaction, the type and number of ligands, intermixing of the metals, network formation versus individual phases, wetting of the substrate, the pyrolysis temperature, weight loss during heat treatment, and the stress development of the film [3].

Many routes have been proposed for PZT solution preparation. The route proposed by Milne et al. [50] uses 1,3-propanediol as the solvent for the reaction. Yi et al. and Schwartz et al. [51] used chelating agents such as 2,4-Pentadione, acetic acid or amine compounds. The metalorganic decomposition method proposed by Vest [52] utilizes large species such as lead 2-ethylhexanoate, zirconium neodecanoate, and titanium dimethoxy dineodecanoate in a xylene solvent. These increase the stability of the solution by creating larger ligands [51,53].

For the synthesis of sol-gel PZT solutions, the method first proposed by Budd et al. and further developed by several authors [54] produces good thick and thin film PZT. In this method the starting reagents are zirconium n-propoxide, titanium isopropoxide, and lead acetate tri-hydrate. In this case, lead acetate is preferred due to the instability of the lead alkoxide and its limited availability [3]. The solvent used is 2,4-Methoxyethanol (2MOE). The flow chart for the PZT synthesis is shown in Figure 1-24.

Caruso et al.[4] investigated the reactions taking place during PZT synthesis using nuclear magnetic resonance spectroscopy and Fourier transform infrared analysis. It is suggested that after dehydration and alcolysis of the lead precursor the acetate group is mostly, but not completely, substituted by a methoxyethanol ligand. Even after dehydration of lead by increasing the temperature to 115 ^{o}C under reduced pressure [39], some water still persists. After ligand exchange in 2MOE the propoxide groups on the titanium are fully substituted to form $Ti(CH_2CH_2OCH_3)_4$. The Zr precursor formed is a polynuclear structure where the propoxide groups are fully substituted by the methoxyethanol groups.

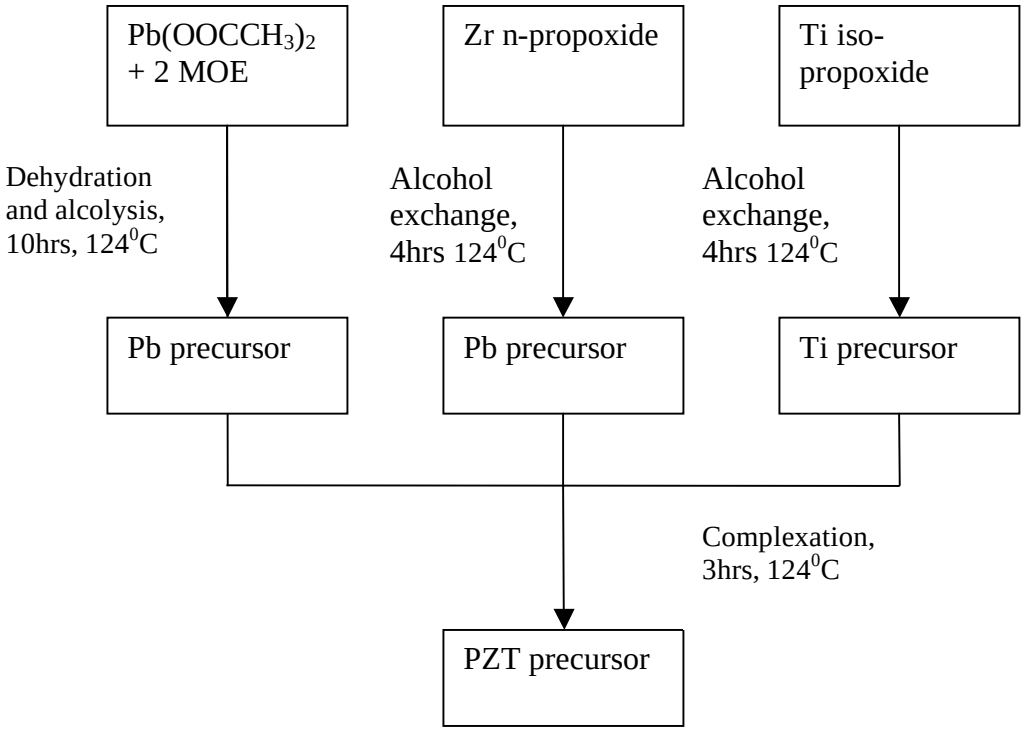

Figure 1-24: Flow diagram of the PZT synthesis as presented by Caruso et al. [1]

The Zr precursor as suggested by Caruso et al. is depicted in Figure 1-25.

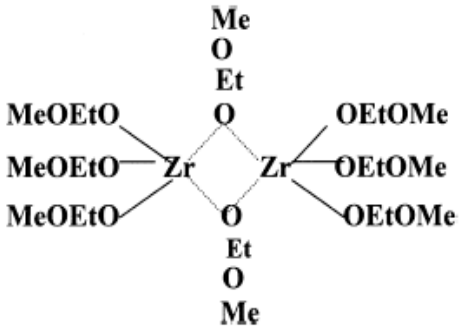

Figure 1-25: The Zr precursor after alcohol exchange [4]

Et- Ethyl group
Mt-methyl group

After refluxing all the precursors in MOE for several hours, the resulting alcoxide species formed is $PbZr_{0.5}Ti_{0.5}(OCH_2CH_2OCH_3)_6$ [3]. In the solution a polycondensation reaction takes place, and oligomers are formed as a result. This reaction is catalyzed by water which could come from the incomplete lead precursor dehydration. The hydrolysis

and polycondensation process can be represented by the following reactions as described by Schwartz [3]:

Hydrolysis:

$M(OR)x + H_2O \rightarrow M(OR)_{x-1}(OH) + ROH$

Condensation (alcohol elimination):

$2M(OR)_{x-1}(OH) \rightarrow M_2O(OR)_{2x-3}(OH) + ROH$

Condensation (water elimination):

$2M(OR)_{x-1}(OH) \rightarrow M_2O(OR)_{2x-2} + H_2O$

Acetic acid, sometimes added or formed from the acetate, undergoes an esterification reaction which results in expulsion of water. Therefore, the small amounts of acetate and water present help to form polymeric chains that stabilize the solution. High amounts of both acetate and water will result in destabilization of the solution and subsequent precipitation [3].

1.12 Film Deposition

1.12.1 Spin Coating

Spin-coating and dip-coating can both be employed for film preparation. Generally dip-coating is the less expensive of the two, but spin-coating allows for the regulation of film thickness and uniformity. The thickness of the individual layer deposited depends on the viscosity of the solution. This is influenced by the concentration of the solution and the ligand used. Wolf [39] reported a fired thickness of 0.2 μm for an

individual layer of 0.75 M solution of MOE based PZT when the substrate was spun at 1500 rpm for 30 s. Increased thickness can be achieved by multiple depositions.

1.12.2 Liquid Source Misted Chemical Deposition

This technique [55] entails converting a sol-gel solution into a fine aerosol consisting of ~0.25 micron sized particles[56] mixed in an inert gas. The droplets are deposited onto a substrate by applying an electric field between the spindle on which the substrate is located in the chamber and a steel mesh attached to the lid of the chamber above the substrate. The advantage of this technique is a superior step coverage over that of conventional sol-gel spinning [57].

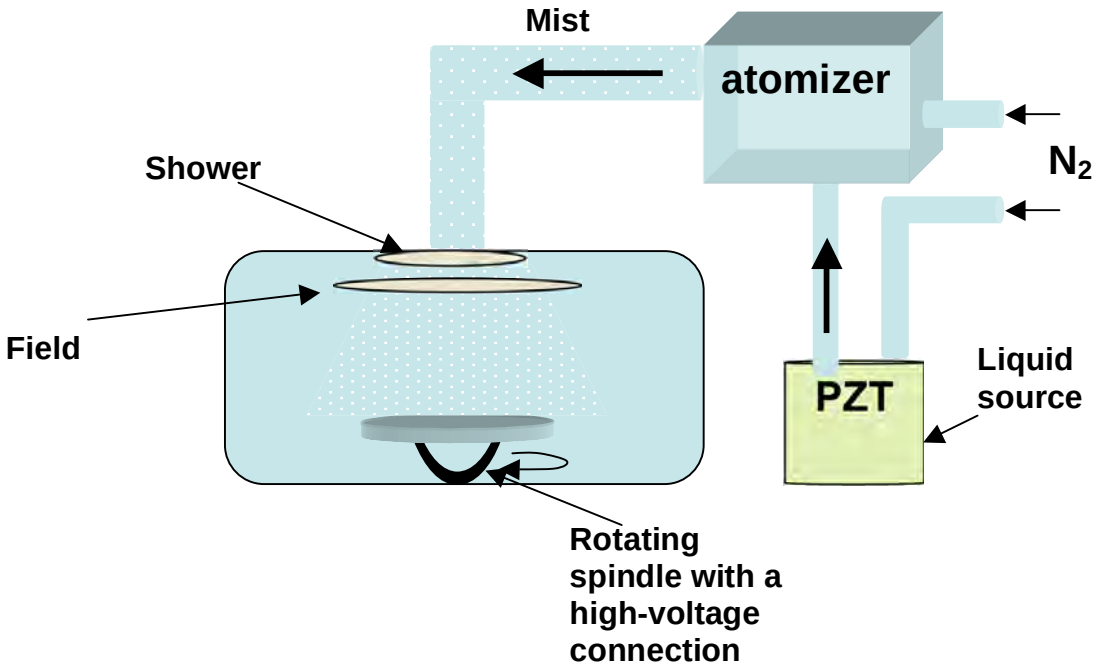

Figure 1-26: LSCMD system schematic

1.12.3 Pyrolysis and Crystallization

After deposition on the substrate the film must be pyrolyzed at 200-400 ^{o}C on a hot plate to burn off any organic species. The organic constituents are removed prior to

the collapse of the amorphous network, which minimizes cracking [3]. The M-O-C and M-O-H bonds with the organics are broken, and the M-O-M [3] bonds must be formed. When this takes place, the film shrinkage is 50-70%.

After the pyrolysis step the PZT film is still amorphous, and must be subjected to rapid heating at high temperatures in order for it to crystallize with minimum amounts of a secondary pyrochlore phase. Temperatures of 500-700 ^{o}C and heating rates of 5 to 7500 ^{o}C/min are achieved using a thermal annealing furnace (RTA) [3]. A polycrystalline film with the perovskite structure is formed by the nucleation and growth process on Pt-coated Si substrates.

One of the downfalls of films in comparison to bulk and single crystal materials is the lower dielectric constant and piezoelectric properties. This is attributed to three possible reasons: small grain size (on the order of 0.04-0.26μm [58]), point defects, and effects of substrate clamping [40]. If the main reason for this decrease is substrate clamping then some of the properties could be regenerated upon separation of the transducer elements and partial etching of the substrate.

1.13 Overview of High Frequency Ultrasound Technology

In this section existing high frequency array ultrasound systems are reviewed. Polymer, single crystal, and ceramic devices are described, in both film and in bulk form. Emphasis is placed on material quality, coupling coefficient, bandwidth, acoustic impedance, and electrical impedance matching to 50 Ohm electronics.

1.13.1 Ceramics: Linear Arrays

Lukacs et al.[59] describe the fabrication and characterization of a linear 64 element piezoelectric array for operation around 28 MHz. In order to fabricate the array, the authors used a 30µmx80µmx3mm PZT bar. Laser micromachining was employed to fabricate 64 elements with 74-micron pitch and an 8-micron kerf. The elements were sandwiched between two matching layers, and were attached to a thick aluminum backing layer as show in Figure 1-27. The ground electrode was placed on top, while individual access to the 64 signal electrodes was underneath the PZT. The k_{33} coupling coefficient was determined to be 0.71. A single pulse generator was used to generate a 30V bipolar pulse across each element. The average centre frequency was 28.1MHz with an 83% BW. The pulse lengths at -6dB and -20dB were 49 and 99 ns, respectively.

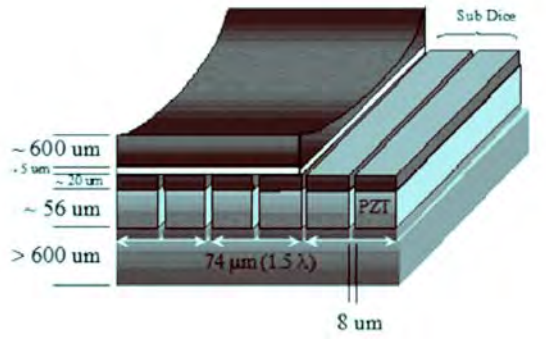

Figure 1-27: Schematic of array structure showing a concave lens, two matching layers, a PZT layer and a backing layer. This array pitch is 74 microns [59]

The acoustic pressure generated was 590 kPa at 10 mm, and the average crosstalk across 6db BW was -40dB for the n±1 element, -47dB for the n±2 element and -61dB for the n±3 element. These results agreed well with the PZFlex simulations.

Another linear 64 element 2-2 composite array is described by Cannata et al. [60] This was fabricated by mechanically dicing a fine grain, high density Navy type VI PZT ceramic. The composite was then back-filled with an epoxy containing 17 vol% Al_2O_3 particles. The pitch of the elements in the array was 50μm (See Figure 1-28). Elevation, or off – axis focusing was achieved using a cylindrical epoxy lens. The resulting center frequency was 34 MHz with a 57.8% bandwidth at -6 dB. The average -20 dB pulse length was 102 ns. The maximum combined electrical and acoustic crosstalk between elements was less then -24dB. The resolution in the human body was 0.1mm. The summary of the properties is shown in Table 1-7.

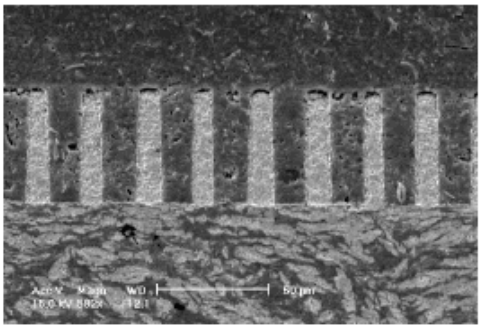

Figure 1-28: An SEM image of the composite.

The darker portion of the image is the filler and the lighter are the PZT posts. The bottom is the silver epoxy backing layer [60].

Table 1-7: Summary of properties of a 35MHz composite from Cannata et al [60].

Property
Number of elements 64
Average center frequency 34 MHz
Highest/lowest center frequency 35.8 MHz / 24 MHz
Average bandwidth (-6 dB) 57.8 %
Average sensitivity 769 mV
Average -20 dB pulse length 102 ns
Electrical impedance magnitude (at 35 MHz)* 35 ohms
Electrical impedance phase angle (at 35 MHz)* -24deg
Focal point 9.5mm

Similar results were also reported by Michau et al.[61] This group fabricated a 128 element linear array 1-3 composite with a centre frequency of 30MHz. The array has a

100µm pitch and a 2mm elevation aperture. The final thickness after dicing, adding the filler, and lapping was 47µm. The device is shown in Figure 1-29.

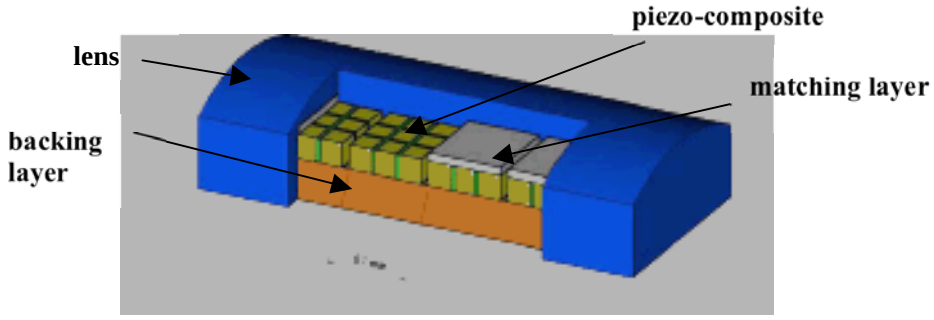

Figure 1-29: Schematic of the device fabricated by Michau et al. [61]

The impedance of the device matches that of a commercial high frequency imaging system. For this reason they used a high dielectric constant piezoelectric to match the 50 Ohm electronics. The properties of the device are summarized in the Table 1-8.

Table 1-8: Summary of results for the ultrasound transducer developed by Michau et al.[61]

Center frequency (-6dB)	27.3MHz
k_t	0.57
Dielectric constant	920
Bandwidth (-6dB)	74%
Average Pulse Length (-20dB)	113ns

As mentioned earlier, one of the major problems associated with fabrication techniques that involve dicing is the limitation of the spacing and size of transducer that can be achieved. Not only is the frequency capped by this limitation, but also the ability to beam steer as the sizes and required wavelengths shrink. Although this can be overcome to some extent by using laser micromachining, the machining needs to be

carried out at low power to avoid degrading the ceramic. This leads to longer machining times. Cross-sectional tapering and material re-deposition can also be a problem [37].

Hackenberger et al. [62] fabricated linear arrays using tape cast PZT sheets separated by epoxy as the filler. In order to fabricate these, green tapes of PZT ceramic powder dispersed in a polymer matrix 25-50μm thick were stacked alternately with a carbon layer. The polymer binder was then slowly burned out. This also volatilized the carbon layer to define the kerf space. The samples were then sintered, and the kerf space formed by the decomposition of the fugitive phase was back filled with the epoxy. The resulting structures are shown in Figure 1-30.

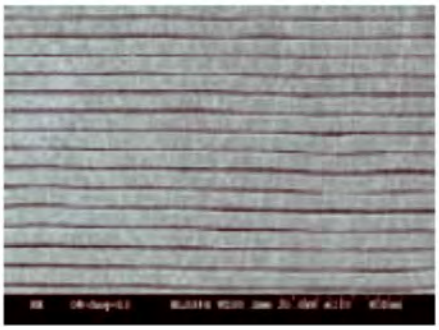

Figure 1-30: SEM image showing the layers of tape cast films with the epoxy fabricated by Hackenberger et al. [62]

To reduce the kerf spacing below λ/2, in order to avoid lateral coupling, the stacks were formed by heat assisted uniaxial pressing. Hackenberger et al. [62] give data on a 20MHz centre frequency array, and claim to be able to fabricate up to 30MHz. The measured centre frequency was 21MHz, the bandwidth was 71%, and the insertion loss was -14dB for a transducer with a 38μm element thickness and a 7μm kerf. They also showed images of transducer elements with 22μm element thickness and a 4.5μm kerf. These are some of the best published results with a high bandwidth and low loss.

Lukacs et al. [18,24,38] developed an ultrasound array with a center frequency of 40-100MHz utilizing composite sol-gel technology. They used an acetate based PZT solution and added PZT powder into it in order to create thicker layers. Using spin coating they made a film of 20μm thickness. Due to the use of powder in their process, the surface of the films was too rough for successful electrode deposition. In order to overcome this, the films were planarized by polishing. Cr/Au electrodes were sputtered and the film was poled at 9V/μm at 180C. The etching of the film to create the arrays was done using an ultraviolet Nd:YAG laser. The authors fabricated a linear transducer array with an element pitch of 15μm. Despite the promising computational results, the only experimental results reported were the resonance modes as a function of frequency as the impedance, Z, and phase angle, Θ.

M. Lukacs and Jianhua et al. [63] describe a method of fabricating 20-40MHz frequency transducers using the IPhB (Interdigital phase bonding) method. In comparison to the other techniques it can achieve smaller kerf and ceramic widths, allowing for higher frequency design (See Table 1-9).

Table 1-9: Table 1-comparing various methods that have been used to fabricate high frequency arrays and their resolution limits.[63]

Method [ref]	Pitch (μm)	Ceramic width (μm)	Kerf width (μm)
IPhB	25	15	4, 15
Tape lamination [64]	33	28	5
Laser cutting [65]	33	25	8
IPB [66]	40	36	4
Dice and fill [67]	50	26	24

A schematic representation of the IPhB method is shown in Figure 1-31. First, two pieces of PZT ceramic are diced using a conventional saw. The two pieces are then mated together so that the two sets of PZT "teeth" interleave and are epoxied in place. By lapping away both sides, a 2-2 composite with a pitch on the order of the thickness of the dicing saw blade can be made. For typical blades of 25 - 30μm in thickness, the element can be made as thin as about 30μm and should be lapped to a thickness of larger than 50μm. This results in structures useful at frequencies 20 - 40MHz. Even smaller pitches can be achieved if four PZT plates are diced as in Figure 1-31 step A and are interdigitated as in step B. The interdigitated PZT pairs are lapped only on one side as in step C and the exposed surface is diced a second time with the same pitch as the first dicing stage but with the blade spatially shifted (phase shifted) by a fraction of the original pitch to the original dicing positions as in step D. The two diced composites are interdigitated with epoxy as in step E. Finally, by lapping away both sides of the interdigitated piece, a 2-2 composite structure with a pitch that is less than the blade thickness is made.

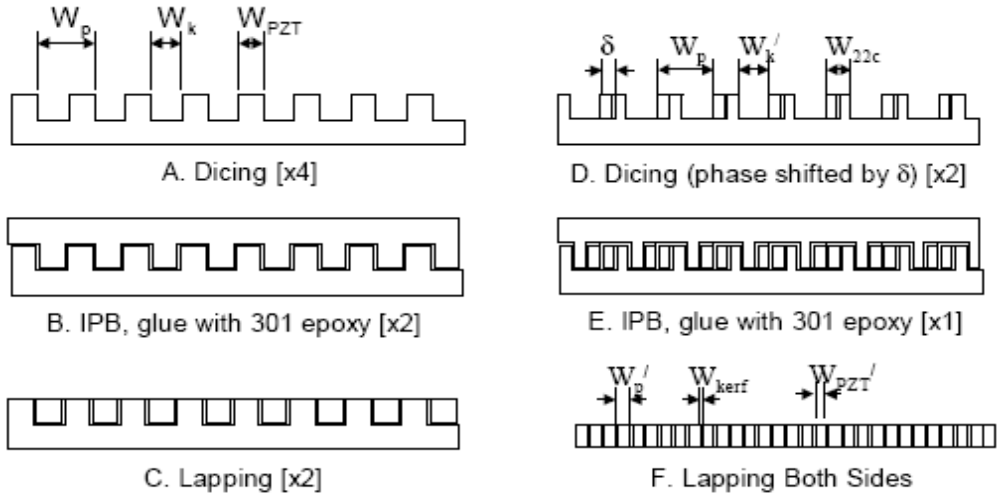

Figure 1-31: Process flow for the fabrication of an ultra-fine pitch composite using the IPhB method.[63]

The SEM images of the fabricated composite are shown Figure 1-32. These have 19 μm wide PZT elements with a 24μm pitch. The PZT volume fraction is 81%.

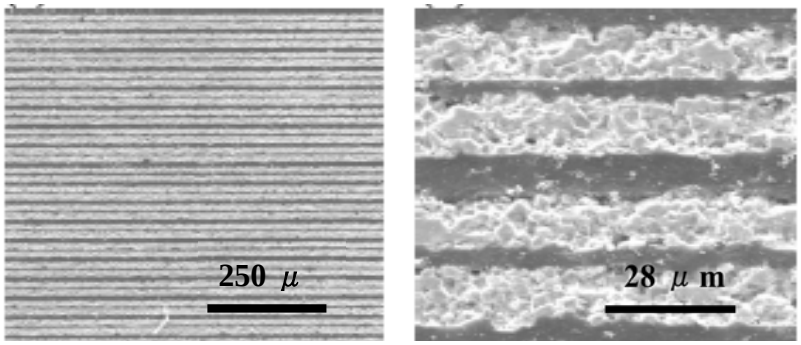

Figure 1-32: Figure 1-30: SEM image of the arrays fabricated by Jianhua et al. [39] using the IPhB method

Such a sample could be considered for a 50 MHz array with a < 1.0λ water pitch or for a sub-diced (two elements as a group) 30 MHz linear array with 1.0λ water pitch. The clamped dielectric constant of the material was 930, and the k_{33} was measured to be 0.62. The -6 dB frequency was 58MHz with a 33% bandwidth.

1.13.2 2-Dimensional Arrays

Jiang et al. [68] used dry etching of single crystal piezoelectrics to fabricate transducer arrays. The process is schematically shown in Figure 1-33. As can be seen, lithography is used to define a Ni hard mask on the $PbMg_{1/3}Nb_{2/3}O_3$-$PbTiO_3$ crystal surface. They then used reactive ion etching to create high aspect ratio posts. The structures were backfilled with epoxy to create the 1-3 composite, and finally the composites were lapped to the desired thickness and electroded. Impedance and phase angle spectra peaks give a value of 0.72 for the coupling coefficient. The authors do not state the dimensions of the elements in the paper.

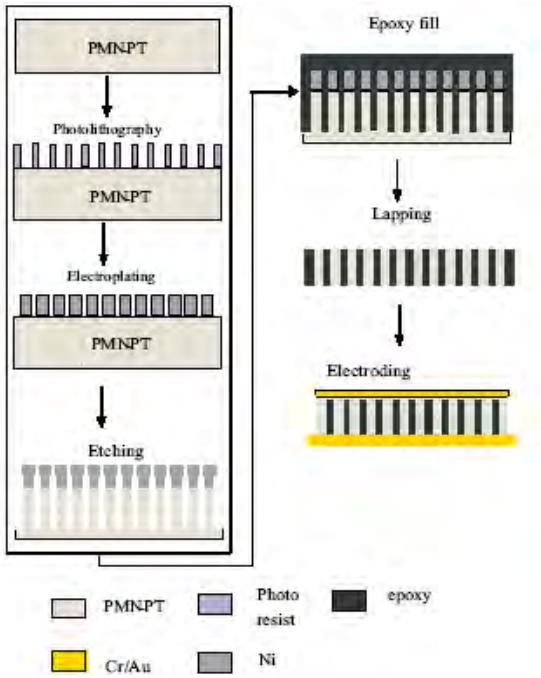

Figure 1-33: A schematic of the transducer fabrication process using single crystal piezoelectrics from [68]

Abrar et al. [37] describe a fabrication process of high aspect ratio piezoelectric structures for 1-3 composites. They use a three-step process. In the first step they mill a combination of a fine PZT-5H ceramic powder solvent and binder/plasticizer to generate a ceramic paste suitable for molding. The paste is then cast into a tape of approximately 1mm thickness. A section of the tape is then embossed into a solid polymer mold. The mold is then dissolved in a solvent. The resulting array is shown in Figure 1-34. The pillars are then embedded in a polymer, and electrodes are applied.

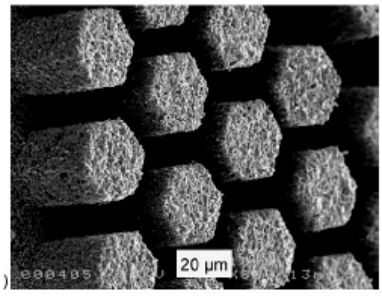

Figure 1-34: Ceramic pillars for 1-3 composite ultrasound. From A. Abrar et al.[37]

The authors fabricated pillars with aspect ratios of 2-10 and pillar heights of 50 to 850 microns. The work was concentrated on pillars of elliptical shape with major diameter of 65 microns and minor of 50 microns. The final thickness of the pillars after lapping was 760 microns, resulting in an aspect ratio of 12. The interelement pitch is not mentioned. The measured center frequency was 2.4 MHz with a -3dB bandwidth of 0.67MHz.

This approach avoids resulting to the use of dicing, and so achieves very high aspect ratio structures, that could potentially be used for high frequency applications. Despite this, the achieved frequency was low, and the bandwidth of the transducer was extremely narrow, making it functional only in a narrow frequency range.

1.13.3 Polymer Arrays

Payne et al. [32,69] fabricated a linear array using a piezoelectric polymer, which could be situated in close proximity to the electronics. A monolithic 16-channel programmable pulse generator chip was fabricated in 1.5 μm CMOS technology. On this chip, time delays with 1ns time resolution and a dynamic range of 2^{19} were achieved. In order to fabricate the transducer, an alumina substrate with screen-printed gold patterns was used. The piezoelectric polymer film was glued to the surface of the substrate, and the electrodes were defined using photolithography. Each array element was 0.2 mm wide and 7 mm long with an inter-element gap of 0.05 mm. The alumina substrate had 32 bonding pads on two of the four sides, and two bonding pad extensions were used for easy connection to the electronics. The ground electrode was formed by vacuum coating the other side of the piezoelectric film through the central opening of the alumina substrate. Conductive epoxy or paint was used to attach an electrical lead to this ground electrode. A square tube was glued to the lower side of the alumina substrate and epoxy-

based backing materials having acoustic impedances close to that of the polymer were filled into the hollow back side of the substrate. The schematic of the transducer is shown in Figure 1-35.

Pulse echo measurements showed that the center frequency of the transducer falls at 32MHz, with a bandwidth of 20MHz (at -3dB), and a pulse duration of 80ns. One of the main advantages of this device is that it can be integrated with a CMOS chip, with both receive and transmit electronics. The authors, however, did not achieve the element spacing of half the wavelength required for electronic steering.

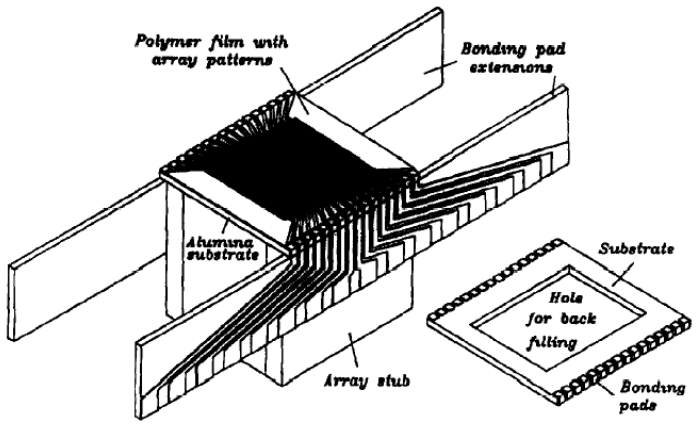

Figure 1-35 A piezoelectric polymer array transducer integratable with a CMOS chip [32,69]

1.13.4 Annular Arrays

In many cases, it is difficult to achieve full focusing capabilities in linear or 2d array transducers at high frequencies. As a result, a number of groups have explored annular array transducers. Beam focusing is done by addressing the inner rings with a time delay with respect to the outer rings. Unfortunately, electronic beam steering cannot be performed with an annular array. Brown et al. [70] describe fabrication of an annular array transducer functional at 50MHz. This transducer was 2mm in diameter, and was

made up of 7 equal area elements. Rather than defining the elements with grooves, the authors simply patterned the electrodes using photolithography. Contacts to the elements were established using wire bonding. PZT-5H was used as the active element, and a 9μm thick PVDF layer was applied to the face to serve as the backing layer. The transducer center frequency was 50MHz with a 50% bandwidth. The resolution was tested on a miniature spherical target at the depth of 5.5 mm (f/2.75). The -6 dB lateral resolution at this depth is 96 microns, which is only slightly poorer then the maximum theoretical resolution of 91 microns. The authors also tested the device on an embryo mouse (See Figure 1-36).

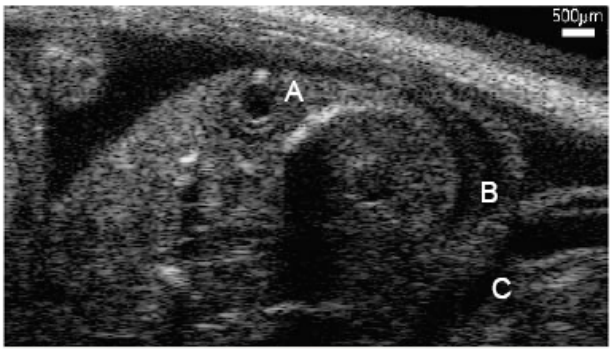

Figure 1-36: Embryo mouse 15.5 days into the gestational period from Brown [70]. The embryonic eye (A) is visible. The uterine wall and amniotic sac (B) are also clearly visible as well as the top portion of a second embryo (C) in the bottom right of the image.

One of the main advantages of this method is the fact that this device is kerfless. Thus, one of the main problems in high frequency ultrasound fabrication is bypassed; there is no longer a need for cutting element to micron-sized dimensions. However, as Lockwood et al [71] reported a year later, the individual elements were not isolated from each other. The resulting high cross-talk across the array increases the effective element width, and results in an increase in the secondary lobe level.

A similar approach was adopted by Gottlieb et al. [72]. 8 P(VDF-Tr-FE) elements with equal areas were separated by 30um kerfs. In order to fabricate the transducer, a 9μm thick ferroelectric polymer film was bonded to a two-sided polyamide flexible circuit with annular electrodes on the top surface. Each annulus had several electroplated microvias that connected to electrode traces on the bottom side of the flex circuit. The average two way insertion loss was -33.5 dB after compensating for diffractive and attenuating losses. The measured average center frequency and bandwidth of an element was 55 MHz and 47%, respectively. The measured crosstalk between adjacent elements was -29dB. After beam forming the lateral resolution at -6dB was 108μm at the focus. The construction schematic is shown in Figure 1-37.

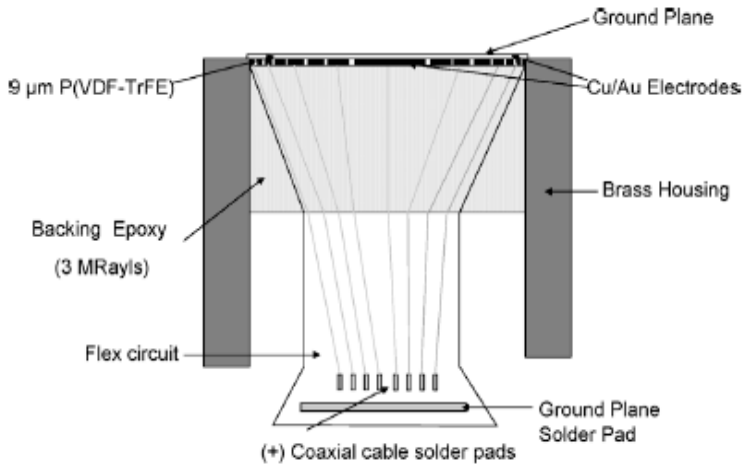

Figure 1-37: Annular array of ferroelectric polymer. After Gottlieb et al. [72]

1.13.5 Thin Film Approaches

Zhou et al. describe the process of fabrication of an array tonpilz transducer using sol-gel lead zirconate titanate as the driver element (see Figure 1-38). The structure was

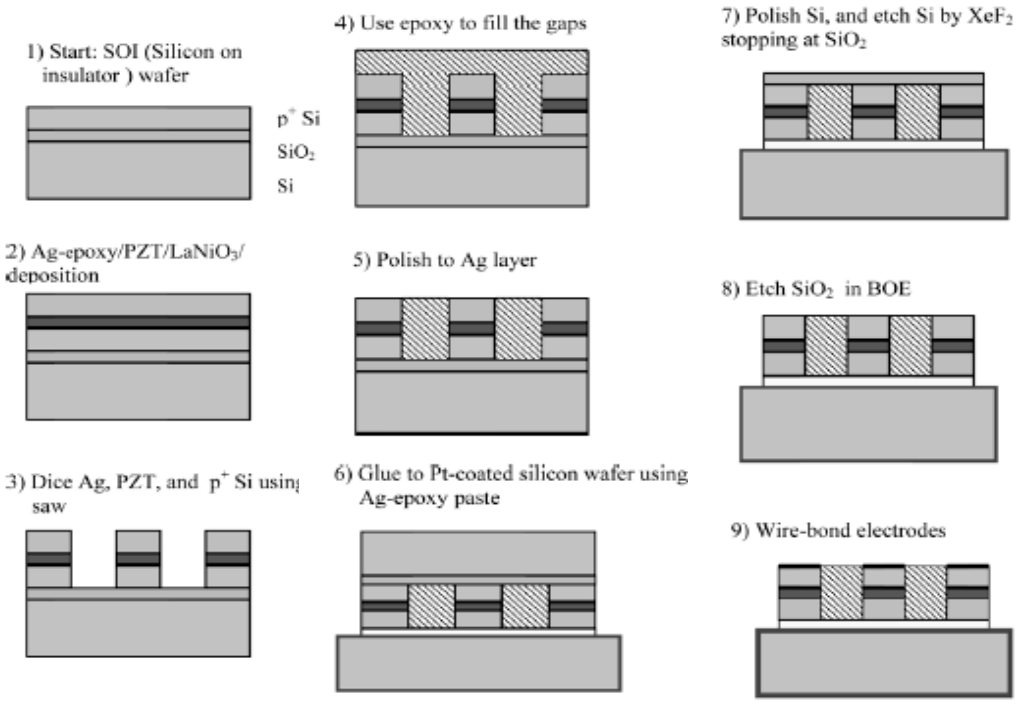

Figure 1-38: Schematic of transducer fabrication process used by Zhou et al. [41]

built using silver/PZT/Lanthanum nickelate ($LaNiO_3$)/silicon on insulator (SOI) substrates. $LaNiO_3$ was used as the bottom electrode, and it was deposited using metalorganic decomposition method (MOD) by spin coating to a thickness of 0.3µm.

The PZT film was grown on the electrode layer by repeated deposition of MOE based solution until the desired thickness of 7µm was achieved. The screen-printed silver layer (which served ultimately as the tail mass) was 35-40µm thick. This layered structure was then diced using a 65µm blade, and the cuts made were about 95µm deep. Each element was about 180 X 180µm. Epoxy was used as filler between the elements. Using conductive epoxy, the silver surface was then bonded to another Pt coated Si substrate. The Si and SiO_2 were then removed from the back of the original substrate using XeF_2 and buffered oxide etches, respectively. The schematic of the device fabrication process

is shown in Figure 1-38. The center frequency falls around 47MHz. No pulse-echo testing is reported.

Other thin film transducers are described by Ito [49,73] and Kleine-Schoder [45,46]. The device fabricated by Kleine-Schoder et al.[46] is shown in Figure 1-39. This is a multilayer PZT array deposited using PVD. The process entailed deposition of Pt electrode pads onto a 50μm thick alumina substrate using a mechanical mask. Another shadow mask was used for the deposition of PZT. The PZT and electrodes were deposited alternatively, and after each deposition of PZT the film was annealed in air. Once the multilayer structure was grown, a backing layer was applied using epoxy, and the transducers were sliced to define the individual elements. The device was cut as far as the epoxy at the bottom, but not through it, in order to provide acoustic isolation without detaching the individual elements. Finally the contact pads are wire bonded to electrical connections, and an impedance matching layer is applied. The dimensions of the array elements are approximately 75 μm wide, 1.2 mm long, 120 μm thick. The kerf width is approximately 30 μm and results from the dicing saw blade. The transducer center frequency was aimed at <75MHz. The multilayer structure was presumably created in order to decrease the driving voltage of the piezoelectric.

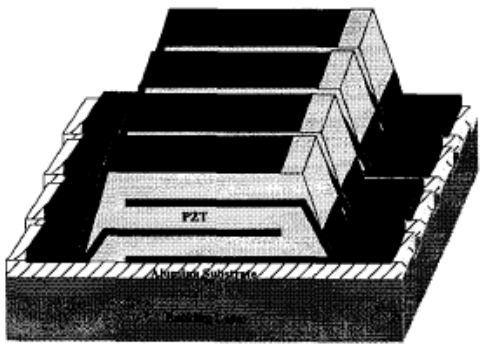

Figure 1-39: Multilayer ultrasound device fabricated using PVD by Kleine-Schoder et al.[46]

Although no acoustic data were shown for the PZT device, a comparable ZnO transducer reported by the same authors was shown to operate properly. The device shown in Figure 1-40 has ZnO strips about 90 μm wide and 2 mm in length, and the film thickness is 12 μm. The spacing between the elements is approximately 10 μm. The pulse echo measurements on this device show a centre frequency of around 150 MHz, and the bandwidth at -12 dB is about 110 MHz (73%).[46] However, the pitch is larger than that required for beam steering at 100MHz (approximately 7.5 μm). This is much smaller then the 100μm used. Usually, a pitch larger than ½ λ will create grating lobes which limit the steering angle.

The device fabricated by Y. Ito [49] is similar to the ZnO device reported by Kline-Schoder, the interelement spacing is, however, created by etching. After a photoresist etching mask of the desired pattern was formed, the top gold electrode was etched in an aqueous solution of iodine, ammonium iodide, and 2-propanol. The chromium adhesion layer was etched off in a mixed acid, which is an anisotropic etchant of ZnO.

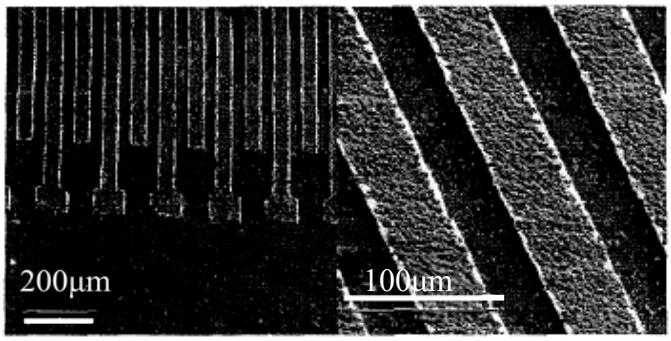

Figure 1-40: ZnO array made by Kline-Schoder et al. [46]

The elements formed were 90μm wide, 3.2mm long, and 10μm thick. The pitch of the elements is 100μm. Again, the pitch is large and grating lobes could present a potential problem.

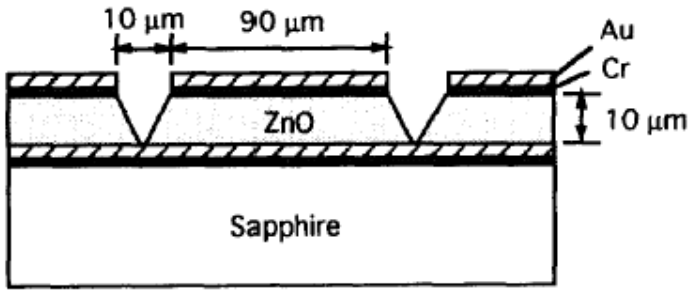

Figure 1-41: A 100MHz transducer proposed by Y. Ito et al. [49]

1.13.6 Piezoelectric Micromachined Ultrasound Transducers (pMUTS) and Capacitive MUTS (cMUT) Arrays

Finally, it would be unfair not to mention some of the efforts taking place on the fabrication of pMUTS and cMUTS. These are microfabricated devices using either electrostatic (cMUT) or piezoelectric (pMUT) elements to generate the sound. In order to increase the amplitude of the deflection from the thin film, flexural elements are used. The fabrication of a pMUT array is described in a patent by Klee et al. [74] from Philips. The device design is shown in Figure 1-42. Unfortunately no data are published on this device.

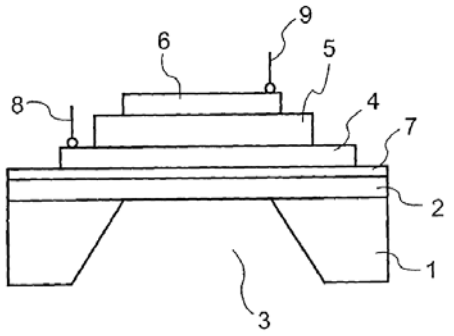

1. Substrate
2. Membrane
3. Opening
4. Electrode
5. Piezoelectric layer
6. Electrode

Figure 1-42: A pMUT construction by Klee et al. [74]

Another p-MUT device was reported by Babrowski and Muralt et al. [75] [76] This device was also fabricated using Si wafers with Ti/Pt electrodes. The PZT was deposited using sol-gel spin coating, and Cr/Au was used for the top electrodes. The elements of the 1x 16 linear array were 1mm to 300μm wide, so the resonance frequency was lower then the resonance frequency that is attempted in this project, and it was centered at 20 kHz to 750 kHz respectively. The membrane is suspended on SiO_2/Si bridges. A single membrane element was approximately $1mm^2$ in size. The distance between the elements is not mentioned by the authors.

The basic building block of a cMUT is a capacitor cell consisting of a metallized membrane (top electrode) suspended above an electrode (such as the heavily doped silicon substrate shown in Figure 1-43).

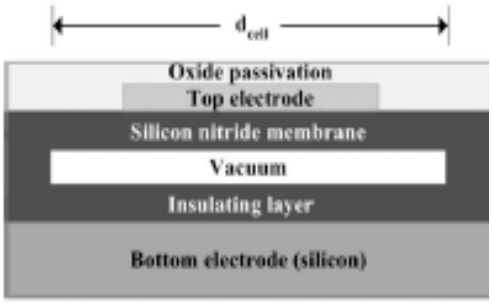

Figure 1-43: A single resonator in a cMUT element, after Oralkan et al. [77]

During CMUT operation, a direct current voltage is applied between the metallized membrane and the substrate, and the membrane is pulled down by the electrostatic force. If the membrane is also driven with an alternating voltage, this generates ultrasound. In order to receive, the biased membrane is subjected to the sound wave and a current output is generated due to the capacitance change under constant bias voltage [78]. The amplitude of this current output is a function of the frequency of the

incident wave, the bias voltage, and the capacitance of the device. The efficiency of a CMUTs can be expressed as the product of the device capacitance to the electric field strength across the gap beneath the membrane [78].

Oralkan et al. [77,78] fabricated a 128 X 128-element 2-D CMUT array with through-wafer via interconnects and a 420μm element pitch. As an experimental prototype, a 32X64-element portion of the 128X128-element array was diced and flipchip bonded onto a glass fanout chip. An 8X16-element portion of the array was used in the experiments. A 4X4 group of elements in the middle of the 8X16-element array was used in transmit, and the remaining elements were used to receive the echo signals. The echo signal obtained from a spherical target was centered at 4.37 MHz with a 100% bandwidth, whereas the frequency spectrum for the echo signal from the parallel plate phantom was centered at 3.44 MHz with a 91% fractional bandwidth.

Figure 1-44 shows a schematic of the cMUT array fabricated by Oralkan et al. [77]. CMUTs are fabricated using standard silicon IC technology; therefore, it is possible to make large arrays using photolithography. Individual electrical connections to transducer elements are provided by through-wafer interconnects. The top electrode is common to all the elements in the array, and the back electrodes are isolated islands of doped polysilicon on the silicon substrate, each electrically accessible from the back side. The dimensions of the ultrasound elements are given in Table 1-10.

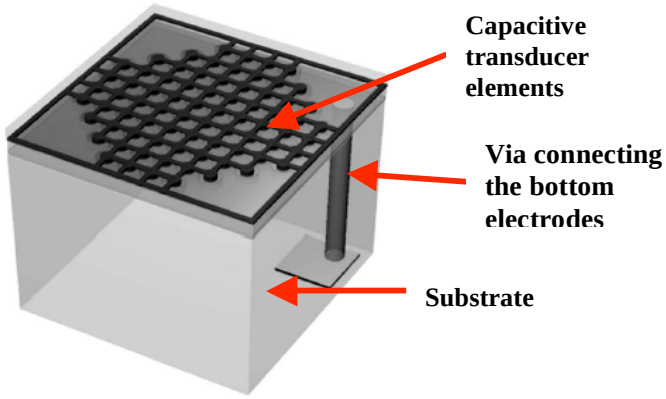

Figure 1-44: A cMUT fabricated by Oralkan et al. [77]

Table 1-10: Physical dimensions of the 2-d cMUT arrays fabricated by Oralkan et al. [77]

Element pitch (d), μm	420
Size of an element, μm $\times$ μm	400 $\times$ 400
Number of cells per element	76
Cell diameter (d_{cell}), μm	36
Membrane thickness (t_m), μm	0.65
Gap thickness (t_g), μm	0.1
Insulating layer thickness (t_i), μm	0.2
Silicon substrate thickness, μm	400

1.13.7 Single Crystal High Frequency Array

Q. Zhou et al. report a successful attempt to fabricating a 44MHz ultrasonic needle for Doppler ultrasound. The design cross-section is shown in Figure 1-45. The device was fabricated using a (001) poled single crystal PMN-33PT. The sample was lapped to 50 microns and matching layers were applied and lapped to 10 microns. A conductive backing material was also lapped to 3 mm. The design was then housed, and the housing was isolated from the needle using polyamide. Au electrodes were sputtered electrical impedance of the transducer was 47 Ohms. The phase angle was -38^0, and the calculated k_t of the device was calculated to be 0.55. A 1.2mm device was used to measure the pulse-echo response. The center frequency and bandwidth at -6dB were

measured to be 44MHz and 45% respectively. The two way insertion loss was -15dB. The transducer was then tested for imaging abilities on rabbit eyes.

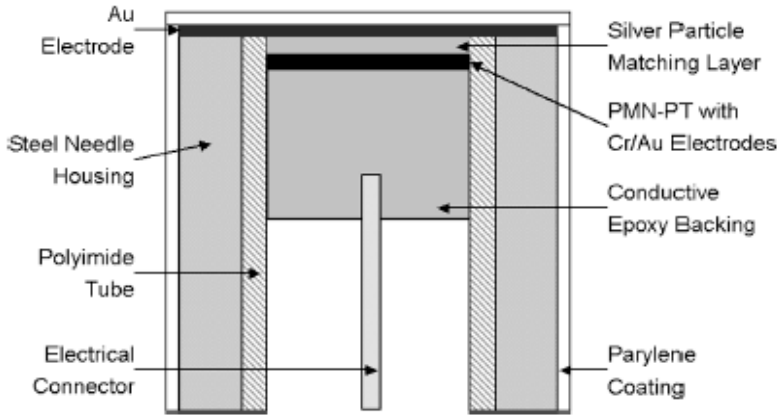

Figure 1-45: Design cross-section of the single element ultrasonic needle reported by Zhou et al.[79]

One such image is shown in Figure 1-46 Doppler type systems are extremely important for measuring such things as the blood flow through arteries, and this device was determined to be functional for the use at high frequencies.

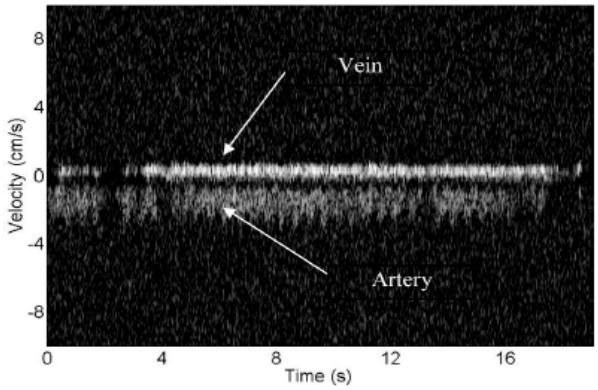

Figure 1-46: An image of an artery and a vain in rabbit's eye imaged using a 44MHz single element transducer by Zhou et al.[79]

Table 1-11 summarizes the works on high frequency imaging discussed in this thesis, and some of the important parameters achieved in each work.

Table 1-11: A summary of the results of high frequency ultrasound systems

Array type	Freq. (MHz)	BW (-6dB)	material	Electr. focus.*[1]	Electr. focus.[2]	Pitch (μm)	Author
Linear	28.1	83%	PZT ceramic	no	yes	74	[59]
linear	34	57.8	PZT ceramic	no	no	50	[60]
linear	27.3	74	PZT /polymer composite	no	yes	100	[61]
linear	21	71	Ceramic PZT films	no	no	[48]	[62]
linear	40-60		Composite sol-gel	no	yes	20	[18,24,38]
linear	58	33	IPhB	no	no	24	[63]
2d	20-45		Single crystal PMN-PT	yes	no	17	[68]
2d	2.4	0.64 (-3dB)	PZT film	yes	yes		[37]
linear	32	~60 (-3dB)	PVDF	no	yes	0.2mm	[32,69]
annular	45	50	PZT		yes	2mm aperture, 7elements	[70]
annular	55	47	PVDF		yes	1mm aperture, 8 lements	[72]
2d	47		Sol-gel	no	yes	180	[41]
linear	150	~75 (-12dB)	ZnO	no	yes	100	[46]
pMUT	0.02-0.75		PZT sol-gel			yes	[75 76]
cMUT 2d	3.4-4.4	100	Si/SiO_2 $/SiN_x$	no	yes	420	[77]

[1] This determines if electronic focusing for the full range of angles without being limited by grading lobes can be achieved at the specified dimensions, i.e. if the pitch of the elements is less than half a wavelength
[2] This determines if electronic focusing was part of the design. This can be achieved if the elements can be individually electroded and addressed at specified time intervals

1.14 Statement of Work

High frequency ultrasound systems are of considerable interest for high resolution imaging of living tissues. However, at present, it is difficult to achieve the required λ/2 interelement spacing in combination with impedance matching above ~30 MHz. Due to the large grain size of many bulk ceramics, they are extremely hard to dice into very fine structures without chipping, and grain pull out. A 50 MHz phased array would incorporate elements spaced on 15 μm centers and separated by 5 μm kerfs. At present, this kerf cannot be achieved by dicing. Moreover, the resulting 10 μm wide elements would have a clamped capacitance of approximately 3 pF, assuming a PZT-5H equivalent ceramic was used in the design [48]. This is too small to readily match to 50 Ohm electronics. Current bulk fabrication approaches becomes impossible for array transducers near 1GHz, since the dimensions shrink with increasing frequency of operation.

Thus, the goal of this thesis is to explore thin-film based approaches to fabricating high frequency ultrasound arrays. The major advantage of films is the ease of fabrication of extremely thin layers. This allows the capacitance to be large enough for impedance matching at high frequencies. Lead zirconate titanate thin films should also permits a drive of voltage below 5V. This enables the transmit and receive circuitry to be integrated onto a CMOS chip. This, in turn, does away with the large cabling that is normally required. Removing the cables drastically decreases the overall size of the device the transducer and a CMOS chip, which both together are only a few millimeters in size. Of particular interest is the design of such a thin film based transducer as well as the

materials science issues associated with processing PZT films on easily micromachined substrates such as Ni.

References

[1] J. A. Zagzebski, *Essentials of Ultrasound Physics* (Mosby, 1996).

[2] B. Jaffe, W. R. C. Jr., and H. Jaffe, *Piezoelectric Ceramics* (R. A. N., Marietta, OH, 1971).

[3] R. W. Schwartz, Chem. Mater. **9,** 2325-2340 (1997).

[4] R. Caruso, O. D. Sanctis, A. Frattini, C. Steren, and R. Gil, Surface and Coatings Technology **122,** 44-50 (1999).

[5] M. Gustafsson, Thesis, Lulea University of Technology, 2005.

[6] L. E. Cross, Ferroelectric Ceramics – Tutorial Reviews, Theory, Processing and Applications (1993).

[7] B. Noheda, D. E. Cox, G. Shirane, J. A. GAnzalo, L. E. Cross, and S.-E. Park, Applied Physics Letters **74,** 661-663 (1999).

[8] W. A. Smith, IEEE Ultrasonics Symposium Proceedings **2,** 755-766 (1989).

[9] http://www.echo-web.com/html/edu-interactive-studies.htm.

[10] J. Z. Zhao, C. H. F. Alves, K. A. Snook, J. M. Cannata, W. H. Chen, R. J. Meyer, Jr., S. Ayyappan, T. A. Ritter, and K. K. Shung, IEEE Ultrasonics Symposium Proceedings **2,** 1185-1190 (1999).

[11] T. S. Curry, J. E. Dowdey, and R. C. Murry, *Christensen's Physics of Diagnostic Radiology*, 4 ed. (Lea & Febiger, Philadelphia, 1990).

[12] P. A. Payne, Journal of Physics E (Scientific Instruments) **18,** 465-473 (1985).

[13] J. S. Markwell, (FTSA, 1996).

[14] W. A. Smith, A. Shaulov, and B. A. Auld, IEEE Ultrasonics Symposium Proceedings**,** 642-647 (1985).

[15] A. Safari, Journal de Physique III **4,** 1129-1149 (1994).

[16] K. A. Klicker, J. V. Biggers, and R. E. Newnham, Journal of the American Ceramic Society **64,** 5-8 (1981).

[17] A. Shaulov and W. A. Smith, IEEE Ultrasonics Symposium Proceedings**,** 648-651 (1985).

[18] M. Lukacs, M. Sayer, and S. Foster, Medical Imaging: Ultrasonic Transducer Engineering Proceedings **3341,** 272-282 (1998).

[19] M. J. Zipparo, K. K. Shung, and T. R. Shrout, IEEE Ultrasonics Symposium Proceedings. **2,** 1663-1667 (1997).

[20] D. A. Knapik, B. Starkoski, C. J. Pavlin, and F. S. Foster, IEEE Ultrasonics Symposium Proceedings **2,** 1457-1460 (1997).

[21] S. Michau, P. Mauchamp, and R. Dufait, IEEE Ultrasonics Symposium Proceedings **2,** 1269-1272 (2002).

[22] S. J. Carey, C. M. Gregory, M. P. Brewin, M. J. Birch, S. Ng, and J. Hatfield, IEEE Ultrasonics Symposium Proceedings **3,** 1930-1933 (2004).

[23] W. A. Smith and B. A. Auld, IEEE Transactions on Ultrasonics Ferroelectrics and Frequency Control **38,** 40-47 (1991).
[24] M. Lukacs, M. Sayer, D. A. Knapik, R. Candela, and F. S. Foster, IEEE Engineering in Medicine and Biology Society Proceedings **1,** 615-616 (1995).
[25] F. S. Foster, K. A. Harasiewicz, and M. D. Sherar, IEEE Transactions on Ultrasonics Ferroelectrics and Frequency Control **47,** 1363-1371 (2000).
[26] P. D. Lopath, P. Seung-Eek, K. K. Shung, and T. R. Shrout, ISAF Proceedings **2,** 543-546 (1996).
[27] S. Zhang, R. Xia, L. Lebrun, D. Anderson, and T. R. Shrout, Materials Letters **59,** 3471-3475 (2005).
[28] N. M. Kari, T. A. Ritter, S. E. Park, T. R. Shrout, and K. K. Shung, IEEE Ultrasonics Symposium Proceedings **2,** 1065-1068 (2000).
[29] S.-E. Park and T. R. Shrout, IEEE Transactions on Ultrasonics Ferroelectrics and Frequency Control **44,** 1140-1147 (1997).
[30] R. E. Eitel, PhD Thesis, The Pennsylvania State University, 2003.
[31] S. Trolier-McKinstry and P. Muralt, Journal of Electroceramics **12,** 7-17 (2004).
[32] P. A. Payne, J. V. Hatfield, A. D. Armitage, Q. X. Chen, P. J. Hicks, and N. Scales, IEEE Ultrasonics Symposium Proceedings **3,** 1523-1526 (1994).
[33] J. F. Tressler, S. Alkoy, and R. E. Newnham, Journal of Electroceramics **2,** 257-272 (1998).
[34] A. R. West, *Solid State Chemistry and its Applications* (John Wiley & Sons, Chichester, 1984).
[35] A. Safari, R. K. Panda, and V. F. Janas, Key Engineering Materials **122-124,** 35-70 (1996).
[36] D. Damjanovic and R. E. Newnham, Journal of Intelligent Material Systems and Structures **3,** 190-208 (1992).
[37] A. Abrar, D. Zhang, B. Su, T. W. Button, K. J. Kirk, and S. Cochran, Ultrasonics **42,** 479-484 (2004).
[38] M. Lukacs, M. Sayer, and S. Foster, IEEE Ultrasonics Symposium Proceedings **2,** 1709-1712 (1997).
[39] R. A. Wolf, M.S. Thesis, The Pennsylvania State University, 1998.
[40] S. Trolier-McKinstry, (Personal Communication, 2007).
[41] Q. Zhou, J. M. Cannata, R. J. Meyer, Jr., D. J. Van Tol, S. Tadigadapa, W. J. Hughes, K. K. Shung, and S. Trolier-McKinstry, IEEE Transactions on Ultrasonics, Ferroelectrics and Frequency Control **52,** 350-357 (2005).
[42] M. Lukacs, M. Sayer, and S. Foster, IEEE Transactions on Ultrasonics Ferroelectrics and Frequency Control **47,** 148-159 (2000).
[43] W. Zhihong, Z. Weiguang, Z. Hong, M. Jianmin, C. Chen, Z. Changlei, and T. Ooi Kiang, IEEE Transactions on Ultrasonics Ferroelectrics and Frequency Control **52,** 2289-2297 (2005).
[44] M. Lukacs, Y. Jianhua, P. Guofeng, R. C. Garcia, E. Cherin, R. Williams, J. Mehi, and F. S. Foster, IEEE Transactions on Ultrasonics, Ferroelectrics and Frequency Control **53,** 1719-1729 (2006).
[45] R. J. Kline-Schoder, D. B. Kynor, M. D. Jaeger, A. A. Winder, and C. Desilets, IEEE Northeast Bioengineering Conference Proceedings**,** 87-91 (1999).

[46] R. J. Kline-Schoder, D. B. Kynor, M. D. Jaeger, A. A. Winder, and C. S. Desilets, Medical Imaging: Ultrasonic Transducer Engineering **3664,** 221-228 (1999).
[47] P. A. Payne, J. V. Hatfield, A. D. Armitage, Q. X. Chen, P. J. Hicks, and N. Scales, in *Integrated ultrasound transducers*, 1994, p. 1523-1526 vol.3.
[48] W. Hackenberger, P. W. Rehrig, T. Ritter, and T. Shrout, IEEE Ultrasonics Symposium Proceedings **2,** 1101-1104 (2001).
[49] Y. Ito, K. Kushida, K. Sugawara, and H. Takeuchi, IEEE Transactions on Ultrasonics Ferroelectrics and Frequency Control **42,** 316-324 (1995).
[50] Y. L. Tu and S. J. Milne, Journal of Materials Research **10,** 3222-3231 (1995).
[51] G. Yi, Z. Wu, and M. Sayer, Journal of Applied Physics **64,** 2717-2724 (1988).
[52] R. W. Vest and J. Xu, IEEE Transactions on Ultrasonics Ferroelectrics and Frequency Control **35,** 711 (1988).
[53] K. D. Budd, S. K. Dey, and D. A. Payne, Proceedings of the British Ceramic Society on Electronic Ceramics **36,** 123 (1984).
[54] M. Kosec, B. Malic, and M. Mandeljc, Materials Science in Semiconductor Procesing **5,** 97-103 (2003).
[55] L. D. McMillan and C. A. P. d. Araujo, (Patent No. 690940, 1992).
[56] www.primaxxinc.com.
[57] M. D. Losego, B.S. Thesis, The Pennsylvania State University, 2003.
[58] J. Cheng and Z. Meng, Thin Solid Films **385,** 5-10 (2001).
[59] M. Lukacs, Y. Jianhua, P. Guofeng, R. Garcia, E. Cherin, R. Williams, F. S. Foster, and J. Mehi, Ultrasonics Symposium Proceedings **1,** 105-108 (2005).
[60] J. M. Cannata, Q. F. Zhou, and K. K. Shung, Ultrasonics Symposium Proceedings **2,** 894-897 (2004).
[61] S. Michau, P. Mauchamp, and R. Dufait, IEEE Ultrasonics Symposium Proceedings **2,** 898-901 (2004).
[62] W. Hackenberger, S. Kwon, P. Rehrig, K. Snook, and S. Rhee, Ultrasonics Symposium Proceedings **2,** 1253-1256 (2002).
[63] Y. Jianhua, M. Lukacs, K. Harasiewicz, and S. Foster, Ultrasonics Symposium Proceedings **3,** 1962-1965 (2004).
[64] T. A. Ritter, T. R. Shrout, R. Tutwiler, and K. K. Shung, , IEEE Transactions on Ultrasonics Ferroelectrics and Frequency Control **49,** 217-230 (2002).
[65] M. Lukacs, M. Sayer, G. Lockwood, and S. Foster, IEEE Ultrasonics Symposium Proceedings **2,** 1209-1212 (1999).
[66] R. Liu, K. A. Harasiewicz, and S. Foster, IEEE Transactions on Ultrasonic Ferroelectrics and Frequency Control **48,** 233-47 (1990).
[67] J. M. Canata and K. K. Shung, IEEE Ultrasonic Symposium Proceedings**,** 1658-62 (2003).
[68] X. Jiang, J. R. Yuan, A. Cheng, G. Lavallee, P. Rehrig, K. Snook, S. Kwon, W. Hackenberger, J. Catchmark, J. McIntosh, and X. Geng, Solid-State Sensors, Actuators, and Microsystems Workshop Proceedings**,** 384-387 (2006).
[69] J. V. Hatfield, N. R. Scales, A. D. Armitage, P. J. Hicks, Q. X. Chen, and P. A. Payne, Sensors and Actuators A: Physical **41,** 167-173 (1994).
[70] J. A. Brown, C. Morton-Demore, F. S. Foster, and G. R. Lockwood, IEEE Ultrasonics Symposium Proceedings **1,** 760-763 (2004).

[71] C. E. M. Démoré and G. R. Lockwood, IEEE Ultrasonics Symposium Proceedings **1** 113-6 (2005).
[72] E. J. Gottlieb, J. M. Cannata, H. Chang-Hong, and K. K. Shung, IEEE Transactions on Ultrasonics Ferroelectrics and Frequency Control **53,** 1037-1045 (2006).
[73] Y. Ito, K. Kushida, K. Sugawara, and H. Takeuchi, IEEE Ultrasonics Symposium Proceedings**,** 1117-1125 (1993).
[74] M. Klee, T. Schlenker, O. Dannappel, H.-P. Loebl, G. Schmitz, and J. Fraser, (Koninklijke Philips Electronics Patent 6972510 B2, 2005).
[75] P. Muralt, N. Ledermann, J. Paborowski, A. Barzegar, S. Gentil, B. Belgacem, S. Petitgrand, A. Bosseboeuf, and N. Setter, IEEE Transactions on Ultrasonics, Ferroelectrics and Frequency Control **52,** 2276-2288 (2005).
[76] J. Baborowski, P. Muralt, N. Ledermann, S. Petitgrand, A. Bosseboeuf, N. Setter, and P. Gaucher, Applications of Ferroelectrics Proceedings**,** 483-486 (2002).
[77] O. Oralkan, A. S. Ergun, C.-H. Cheng, J. A. Johnson, M. Karaman, U. Demirci, K. Kaviani, T. H. Lee, and B. T. Khuri-Yakub, IEEE Transactions on Ultrasonics Ferroelectrics and Frequency Control **50,** 1581-1595 (2003).
[78] O. Oralkan, A. S. Ergun, J. A. Johnson, M. Karaman, U. Demirci, K. Kaviani, T. H. Lee, and B. T. Khuri-Yakub, IEEE Transactions on Ultrasonics Ferroelectrics and Frequency Control **49,** 1596-1610 (2002).
[79] J. M. Cannata, J. A. Williams, Z. Qifa, T. A. Ritter, and K. K. Shung, Ultrasonics, Ferroelectrics and Frequency Control, IEEE Transactions on **53,** 224-236 (2006).

2. Experimental Procedure: Solutions and Characterization Techniques

2.1. *Introduction to the Development of High Frequency Arrays*

Several approaches were considered as methods to produce high aspect ratio piezoelectric elements suitable for ultrasound applications. Because it is difficult to fabricate thin films in the 10 – 50 micron thickness range [1], the approach adopted here is to deposit thinner films onto larger support structures which control the resonance frequency. In order to target a 50MHz center frequency, three types of transducers were considered: tubes, posts, and the xylophone structures.

The tubes were fabricated using micromachined silicon templates in which small diameter, deep pores were etched. Solutions of the piezoelectric and electrode were coated onto the template using vacuum assisted infiltration. After this, the mold was removed using XeF_2, and an array of PZT pillars with $LaNiO_3$ electrodes was left behind. It is possible to prepare very high aspect ratio piezoelectric structures of potential use for high frequency ultrasonic transducers in this manner, since very high aspect ratio mold structures can be prepared in Si.

The second approach was to use a 2D array of metal pillars that were created using electroplating of metal into a prefabricated photoresist mold. After the resist was removed, the metal pillars were coated with PZT using mist deposition, which creates conformal coatings on high aspect ratio structures. The electrical excitation of this structure should be from the core metal to the outer electrode that covers the PZT.

The xylophone structure is a 1D array. For this thesis, the prototype linear array consisted of 10 elements, which are T-bar resonators made using a silicon wafer with an electrode/PZT/electrode stack. Larger contact pads are connected to the elements for wire bonding. The prototype of this structure is to resonate at ~50MHz in the width mode.

2.2 Solution Fabrication

Two types of solutions were used in the course of this thesis: the morphotropic composition of lead zirconate titanate, $Pb(Zr_{0.52}Ti_{0.48})O_3$, otherwise known as PZT for the piezoelectric layer, and lanthanum nickelate, $LaNiO_3$ (LNO) for the electrodes.

A 2- methoxyethanol based PZT solution was used for all the spin or dip coating processes. Depositions in the mist tool were done using a purchased solution from Nippon Ferro Technology C., Ltd, Japan. This is also a 52/48 zirconium to titanium ratio solution.

The LNO electrode solution was used for the deposition of inner and outer electrodes on the tubes fabricated from silicon templates. All other electrodes on the devices were either deposited by sputtering of Pt using the Kurt J. Lesker tool at the Keck Smart Materials Integration Laboratory at Penn State or using ion beam deposition of Cr and gold (which was done in the electrical engineering department by our collaborators).

2.2.1 $LaNiO_3$ Solution Synthesis

This solution synthesis procedure was developed by H. Nagata, a postdoctoral scholar at Penn State's Materials Research Institute [2]. To prepare 100 ml of $LaNiO_3$ solution, 12.991 g of the Ni source, Ni (II) acetate tetrahydrate, $Ni_2(H_2COOH)_2*4H_2O$,

(Aldrich Chemical Co., Milwaukee, WI) was mixed in a beaker in 45 ml of acetic acid and was left to dissolve for 2-5 hours with constant stirring. The La source, 7.466 g of lanthanum acetate, $La(H_2COOH)_3*xH_2O$ (Aldrich Chemical Co., Milwaukee, WI), and an additional 45 ml of acetic acid (Aldrich Chemical Co., Milwaukee, WI), and 4 ml of formamide (Aldrich Chemical Co., Milwaukee, WI) were then added to the Ni solution. The solution was then left to mix for several hours, under constant stirring, until it became clear.

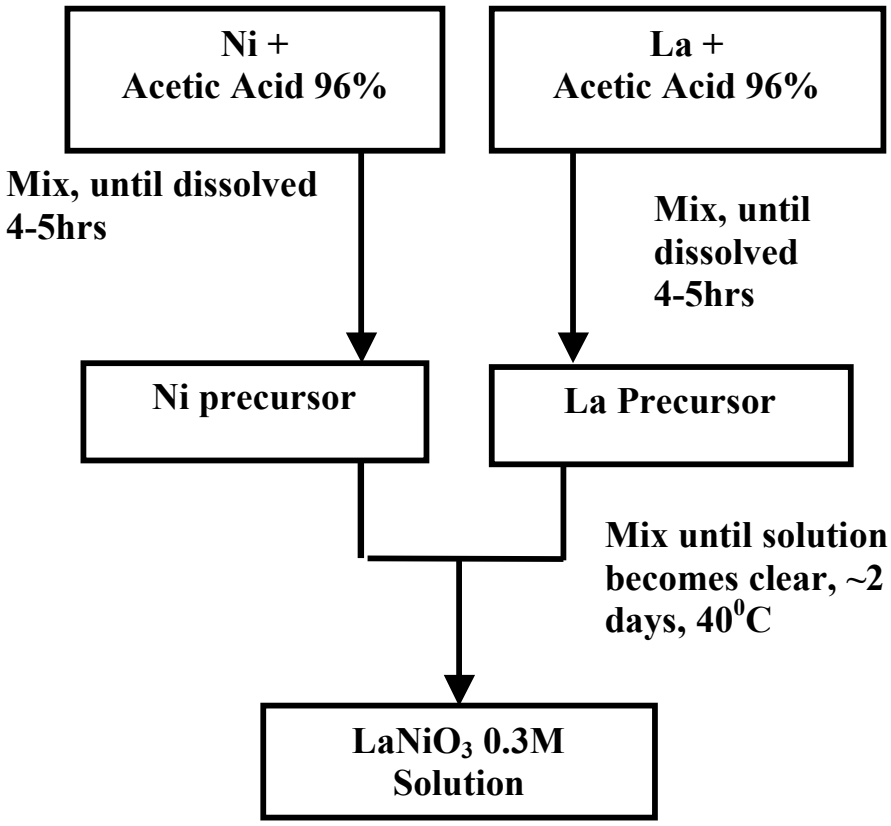

Figure 2-1: Flow chart of $LaNiO_3$ solution preparation

2.2.2 $PbZr_{0.52}Ti_{0.48}O_3$ with 20% excess Pb Solution Preparation

In order to prepare 120 ml of 0.75 M $PbZr_{0.52}Ti_{0.48}O_3$ solution, 40.97 g of lead acetate trihydrate ($Pb(CH_3CO_2)_2 \cdot 3H_2O$), (Aldrich Chemical Co., Milwaukee, WI) was

weighed in a glove box under an argon atmosphere. 100 ml 2-MOE, 2-methoxyethanol ($CH_3O(CH_2)_2OH$), (Aldrich Chemical Co., Milwaukee, WI) was added, and to facilitate dissolution, the mixture was refluxed in a silicone oil bath in an argon atmosphere by slowly raising the temperature from room temperature to 120 ^oC. Slow dehydration of the lead precursor under vacuum was carried out at 120 ^oC until a white powder remained in the flask. While the lead precursor was dehydrating, 13.25 ml of titanium iso-propoxide ($Ti[OCH(CH_3)_2]_4$), (Aldrich Chemical Co., Milwaukee, WI) and 21.0 ml of zirconium n-propoxide, ($Zr[O(CH_2)_2CH_3]_4$), (Aldrich Chemical Co., Milwaukee, WI) were mixed in a beaker containing 60 ml 2-MOE in a glove box under an argon atmosphere. The beaker was then sealed with a paraffin film and was allowed to mix for 20 minutes using a stir bar. The Zr/Ti precursor was then poured into the flask containing the dehydrated lead precursor, and the mixture refluxed under argon for two hours at 120 ^oC. The solution was dehydrated at 120 ^oC in vacuum until $\leq$ 60 ml of solution remained. The solution was transferred to a 120 ml bottle; to it was added 27 ml of 2,4-Pentadione (Aldrich Chemical Co., Milwaukee, WI) and 4 ml of acetic acid (Aldrich Chemical Co., Milwaukee, WI). To achieve a 0.75 M solution, 2-MOE was added to bring the level up to the 120 ml mark [31]. A flow diagram of the process is given in Figure 1.

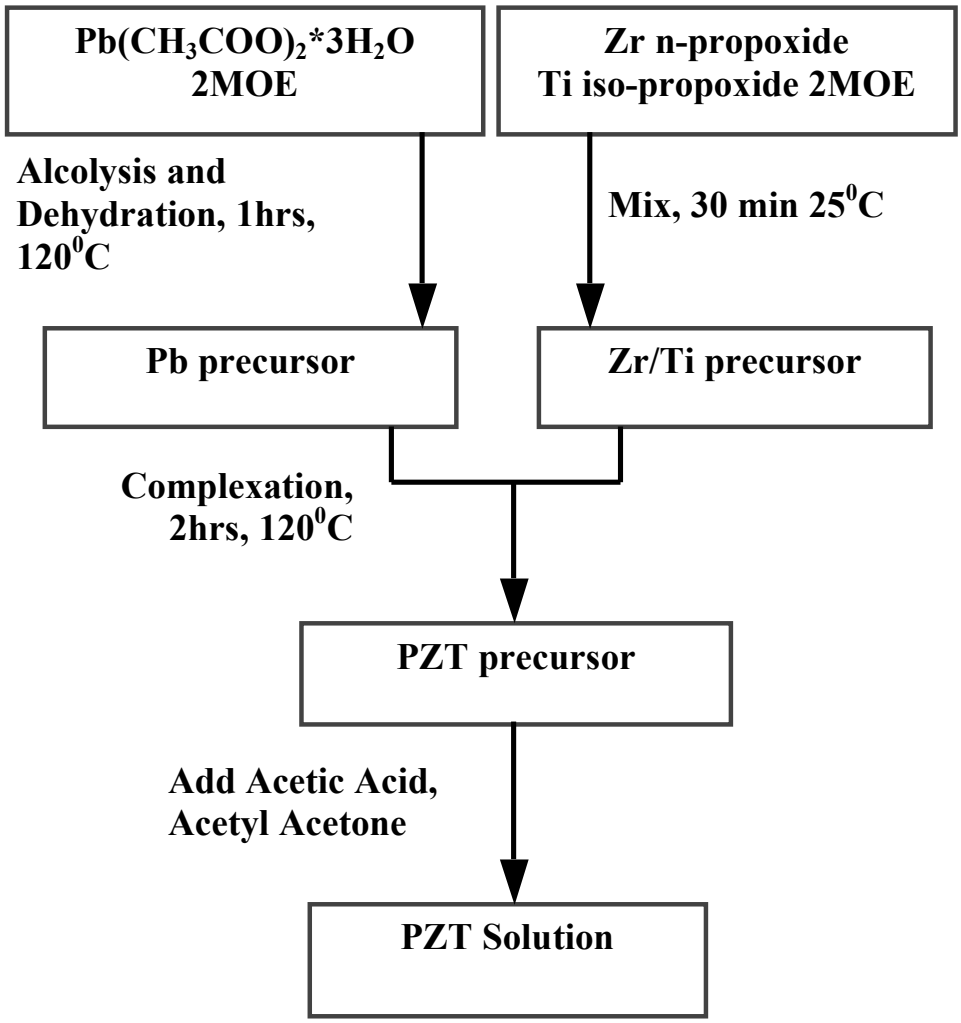

Figure 2-2: Flow chart of the PZT solution preparation.

2.3 Film Deposition

2.3.1 Spin-Coating

Spin coating was used to apply a uniform layer of solution on the surface of the substrate. Solutions were dispensed through a syringe with a 0.1 μm Whatman filter (Aldrich Chemical Co., Milwaukee, WI) and the substrate was spun at 1500-2500 rpm for 30 s using a PWM32 photoresist spinner (Headway Research, Inc., Garland, TX).

2.3.2 Liquid Source Misted Chemical Deposition (LSMCD)

This process was used for deposition of PZT 52/48 onto the nickel posts using solutions that were purchased from Nippon Ferro Technology., Japan. This was performed in a Primaxx 2F deposition tool. The tool was set at 0.3 sccm at 8kV potential between the field screen and the substrate at 1atm pressure. The deposition was performed for 180 seconds per layer, which on a flat substrate resulted to approximately 280Å. Additional details on the tool operation are given elsewhere [3].

2.4 Crystallization of Films

After the application of each layer, the films were subjected to a series of heat treatments to drive off the organic, densify, and eventually, to crystallize the film. The first and second pyrolysis steps, each typically 60 seconds in duration, were performed using a hot plate at 300°C and 450°C, respectively. A crystallization anneal was performed for each layer in a Heatpulse 610 rapid thermal processing (RTP) unit (AG Associates, Sunnyvale, Ca) at 700°C for 60 s. Each layer produced a film of approximately 0.18 μm thickness.

2.5 Characterization Techniques

2.5.1 Scanning Electron Microscopy (SEM)

Scanning electron microscopy was used to examine the surfaces of Ni foils, to determine the microstructures of films at various points during the processing, and to

follow the steps in the mold infiltration process. The instrument used was a S-3500N scanning electron microscope (Hitachi Ltd., Tokyo, Japan).

2.5.2 Electrical Characterization

Electrical measurements on the PZT samples were undertaken to ascertain their electrical quality. For this purpose, contact was made to the top and bottom electrodes. For test capacitors, top electrodes were prepared by sputtering 500Å of Pt. Sputtering was performed in a Kurt J. Lesker sputtering system at 2.5 mTorr Ar gas and 200W power. Low field measurements of capacitance (used to determine relative permittivity) and dielectric loss tangent of the PZT films were made using a 4192A LF impedance analyzer (Hewlett-Packard, Palo Alto, CA). Measurements were carried out at frequencies of 1 kHz to 1MHz and an oscillation voltage of 30 mV_{rms}. Polarization – electric field hysteresis loops were measured on the RT66 (Radiant Technologies, Albuquerque, NM). Comparable data were collected on elements of transducer arrays.

2.5.3 X-Ray Diffraction (XRD)

The X-rays of the samples were taken on Scintag x-ray diffractometer (Scintag, Inc., Sunnyvale, CA). Ni-filtered Cu Kα radiation was used and x-ray diffraction data were collected between 20° and 60° 2θ at a rate of 2° 2θ/min.

2.5.4 Spectroscopic Ellipsometry

In order to characterize the oxidation of Ni foils as a function of annealing temperature, the samples were analyzed using spectroscopic ellipsometry. The angle of incidence and angle of polarization for the measurements were 70° and 30° respectively.

The data were measured over the 250 to 750 nm wavelength range. This data were then modeled to determine the surface roughness of the samples and the amount of oxide present.

References

[1] R. A. Wolf, M.S. Thesis, The Pennsylvania State University, 1998.

[2] H. Nagata, S. W. Ko, E. Hong, C. A. Randall, S. Trolier-McKinstry, P. Pinceloup, D. Skamser, M. Randall, and A. Tajuddin, Journal of the American Ceramic Society **89,** 2816-2821 (2006).

[3] M. D. Losego, B.S. Thesis, The Pennsylvania State University, 2003.

3. One Dimensional Transducer Array

3.1 Introduction

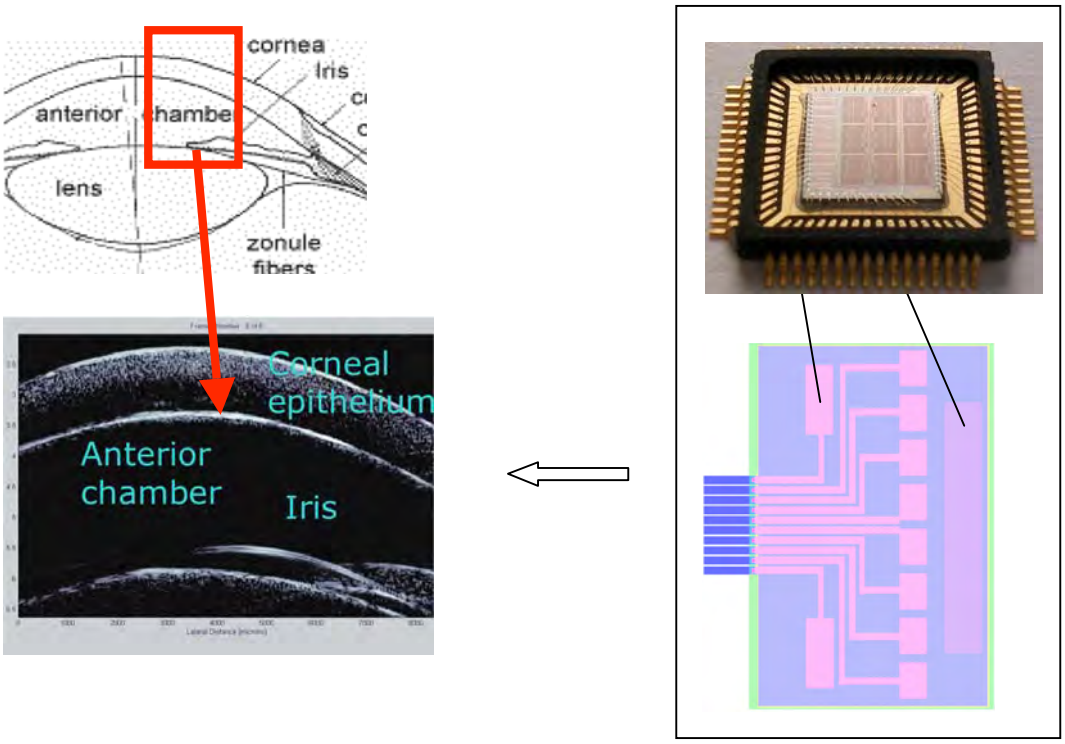

Figure 3-1: Right: A schematic of the ultrasound system with electronics for high frequency imaging. Left: A high frequency image (50MHz) of the eye where the corneal epithelium, the anterior chamber and the iris are visible.

Figure 3-1 is a schematic showing the parts of the first generation ultrasound system, including a linear transducer array and the associated electronics. In order to fabricate the transducer, a surface micromachining approach was adopted. Conventional ultrasound probes are fabricated using bulk ceramics or single crystals that are mechanically diced to create the elements. However mechanical dicing limits the element spacing, especially as the structures become more complex. Because of the larger thicknesses of the individual elements, the driving voltages of these transducers are large, which means that the drive electronics cannot be put on the same chip as the receive electronics. Thus, the goal of this work is to miniaturize the device, and

determining a way to put all the electronics on a CMOS chip would be of great advantage.

In order to achieve the small driving voltages of ~5V, the thickness of the piezoelectric needs to be small, on the order a few microns or less. In this work, the piezoelectric layers were built up using thin film technology. Because the deposition process starts from a solution state, the layers of the piezoelectric can be extremely thin, and the final thickness is made up by cycling the deposition steps.

In order to fabricate the 1D transducer, the film is then taken through a series of masking and lithography steps to define the transducer shape and the electrical interconnects. By using lithography, a transducer with small thickness and dimensions was created for low driving voltages, and higher frequencies.

3.2 One-Dimensional Transducer Modeling

The 1D transducers were designed to be xylophone bar arrays that vibrate in the width mode. By aligning in parallel several of these bars, in this case ten, and exciting them at separate times, the ultrasound wave constructively interferes to focus the beam at a required point of depth. By changing the time delay in firing the inner and outer elements, one can change the point of beam focus.

To estimate the dimensions that would provide appropriate resonance frequencies, the frequency constants of PZT and the dimensions of the transducer were employed. More accurate models were done using KLM, Field II, and finite element analysis, and the final dimensions were based on that. The thickness frequency constant N_t for PZT-8 is 1882Hz•m and the width and length (N_p) is 2170 Hz•m [1]. These

frequency constants were chosen since thin film PZT typically shows limited levels of domain wall motion, so that it behaves as a hard piezoelectric [2].

For the modeling, it was assumed that the PZT is approximately 0.5μm in thickness. Figure 3-2 shows how the resonance frequency changes with dimension for the thickness mode and the length extension mode, using the planar frequency constant. This suggests that the lateral dimension of a device designed to operate at 50 MHz should be on the order of ~40 to 50 microns.

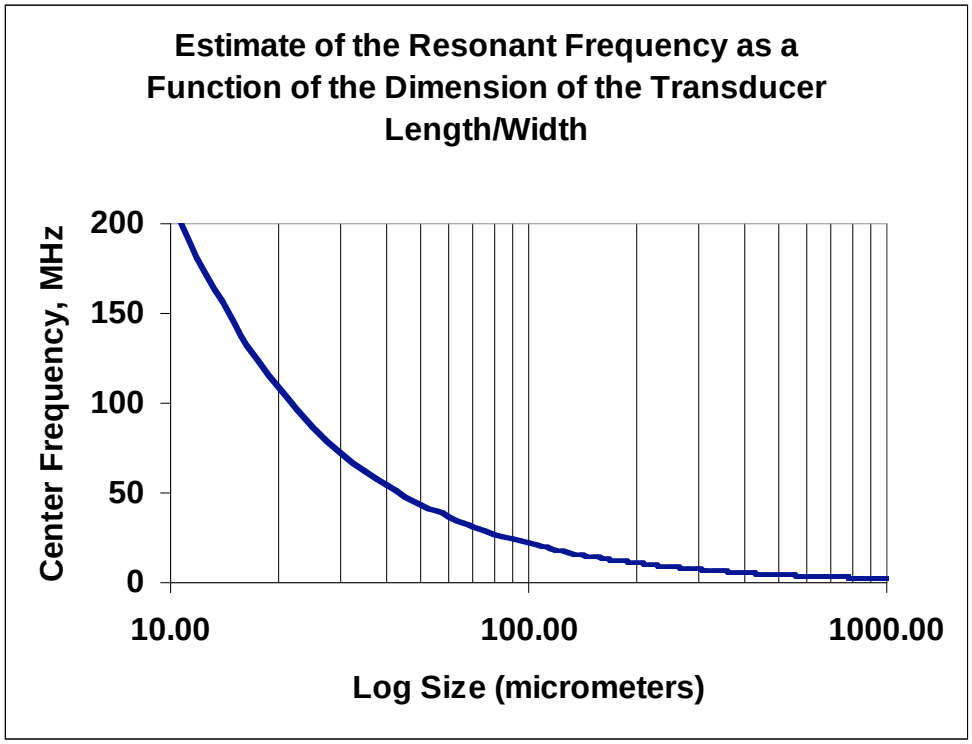

Figure 3-2: Estimated center frequency of an ultrasound system as a function of the planar dimensions of the transducer.

Table 3-1 shows the predicted resonance frequencies for some of the xylophone devices. The fingers were chosen to be 30μm in width. In order to minimize interference between the length extension and the width vibration modes, finger lengths of 150, 200, 250, and 300μm in length were chosen.

Table 3-1: Center frequency calculation using the frequency constants of PZT8 for all the dimensions of the xylophone transducer. The bar width was assigned to 30 microns, and the PZT thickness to 0.5μm

Dimensions Thickness/ Width/Length (μm)	Thickness (GHz)	Width (MHz)	Length (MHz)
0.5/30/300	3.76	72.3	7.2
0.5/30/250	3.76	72.3	8.6
0.5/30/200	3.76	72.3	10.9
0.5/30/150	3.76	72.3	14.5

This provided a length:width aspect ratio of ≥5. The thickness extension mode is at such a high frequency that no interference is expected. The device schematic is shown in Figure 3-3.

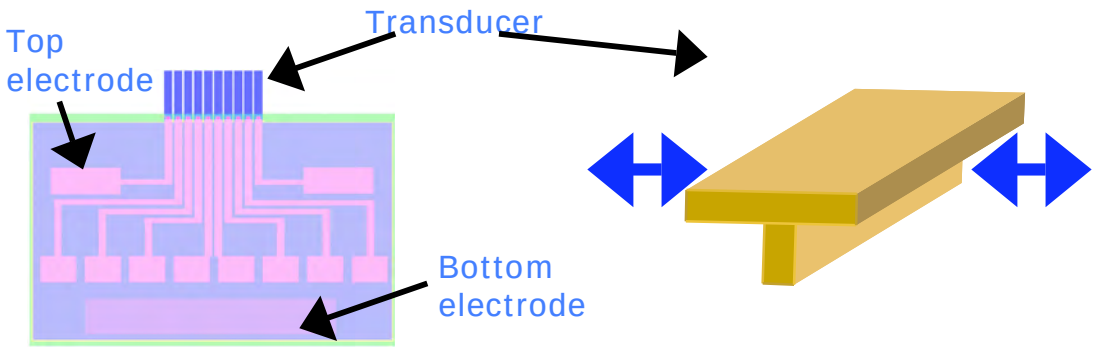

Figure 3-3: Left: Schematic showing the transducer design. Right: A side view of the transducer. The arrows show the motion that creates the 50MHz center frequency.

On the basis of this, a more accurate prediction of the dimensions was done using modeling analytical and finite element analysis software. In particular, this transducer design was modeled using the KLM, PZFlex and Field II models. All the modeling was done in collaboration with Richard Tutwiler. The modeling was done for a PZT-8 sample with Si backing layer, transmitting into water.

The KLM model was done using PiezoCAD. The dimensions were specified, and the shape of the bar was assumed to be rectangular, of 0.5x30x300 μm. Silicon was used as the backing layer and no matching layer was adopted. In the KLM model the device was completely clamped to the substrate. The signal was transmitted into water. The pulse was generated using a single cycle sine wave voltage excitation at 50 MHz. The transmit and receive impedances of the electrical terminations were set at 50 Ohms. The results from the calculation are shown in Figure 3-4 and Table 3-2. The black curve shows the time it takes for the transducer to ring down, and the blue curve shows

Table 3-2: Summary of results for xylophone bar transducer from the KLM model

Level, dB	Center Frequency, MHz	Band Width, MHz	Band Width %CF	Pulse Duration, ns
-6	47.4	48.5	102	14.9
-20	50.2	77.7	55	28.0
-40	51.5	93.1	109	52.8

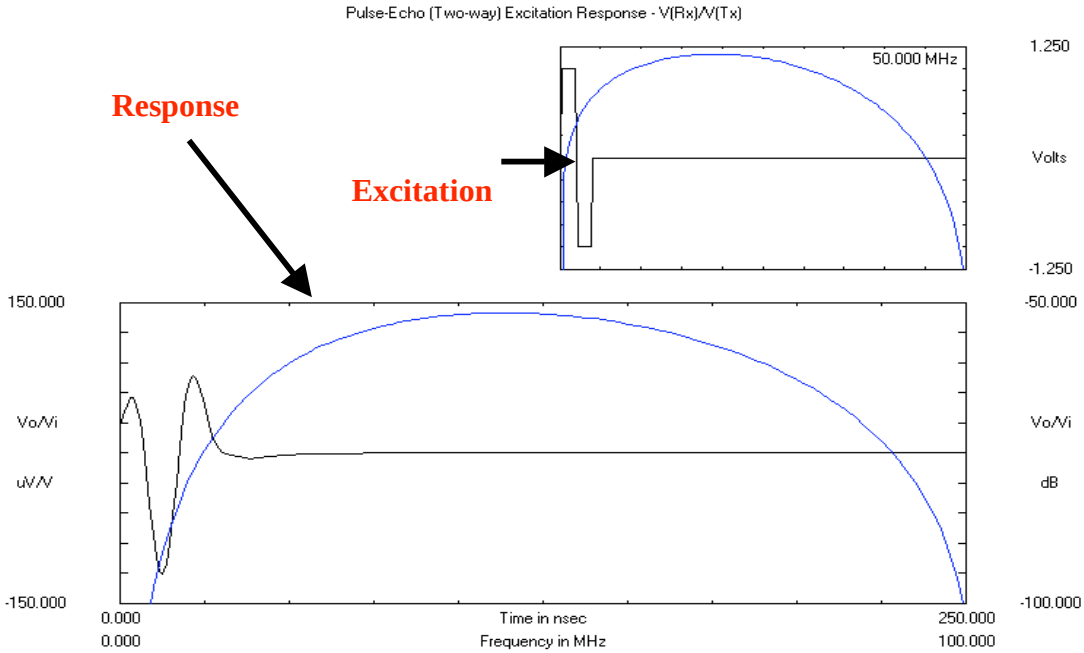

Figure 3-4: The KLM model results of the 1D transducer with SiO_2 backing transmitting into water.

the response of the transducer in the frequency domain. Both of these curves are calculated from the ratio of the receive voltage, V_0 with respect to the transmit voltage V_i.

It can be seen that the bandwidth of the transducer is 102% at -6dB, which is very large, and the center frequency falls very close to the required frequency of 50 MHz. In Figure 3-3 one can see that the excited pulse duration is short with little ringing. This suggest that imaging can be done at a broad range of frequencies with high clarity, and that the transmit and receive signals will not interfere.

One of the main disadvantages of PiezoCAD is the fact that the model is incomplete due to the restricted number of parameters taken into account. For example, the model is done for a rectangle with a Si backing, no account is taken of the fact that the rectangle is only partially clamped to the substrate by a strip of Si/SiO_2 running along the length of the transducer, which should result in less coupling to the substrate. Moreover, the KLM models describe only the thickness mode resonance in a material. As a result, it is not clear that it should accurately describe the width vibration mode employed here.

Thus, the results were compared to a more sophisticated finite element analysis model using PZFlex. The transducer shape was defined through a coordinate system of X, Y, I, and J as shown in Figure 3-5, and a mesh was applied to the system. Only half of the transducer was modeled due to the symmetry axis, and the result was then mirror imaged to create the full picture.

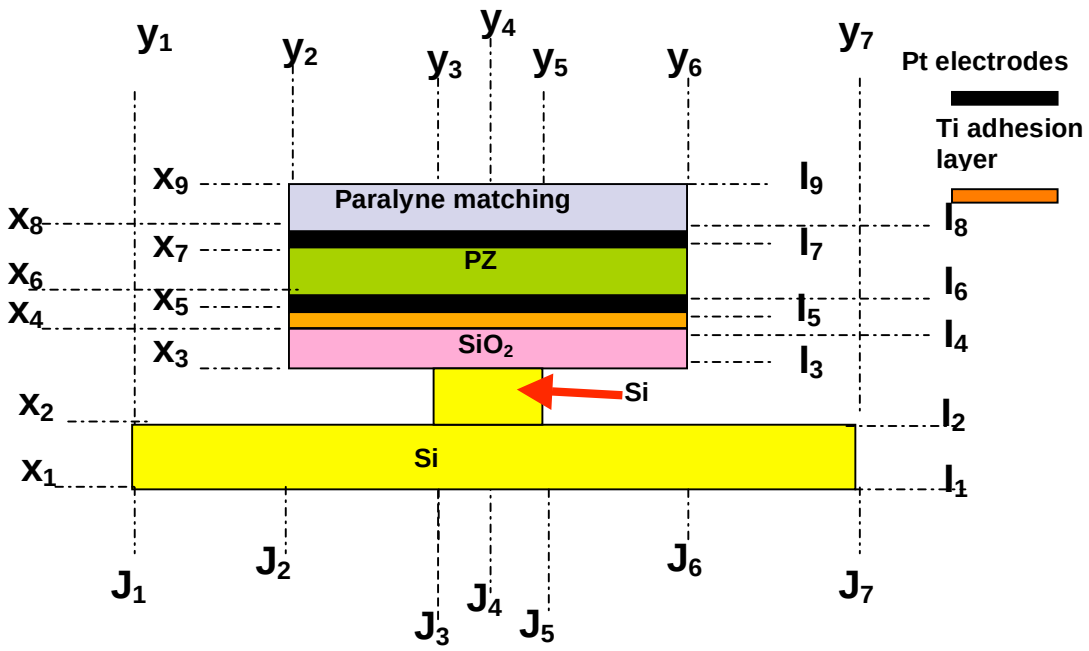

Figure 3-5: The xylophone transducer defined for the finite element analysis modeling

The materials properties were defined through a database, and the transducer was addressed by a single cycle sine wave at 3 V and 50 MHz. The materials selection and geometry that can be used to model in PZFlex is superior to that of the PiezoCAD, so the geometry and composition of all the layers were included. The thicknesses of the modeled layers are shown in Table 3-3. A soft absorbing layer was used as the boundary condition beyond water. The modeling input values are included in Appendix A.

Table 3-3: The thicknesses of each layer of the xylophone transducer as defined for the FEA model

Si Substrate	SiO_2 Backing	Ti Adhesion Layer	Pt Bottom Electrode	PZT	Pt Top Electrode
300 µm	0.3µm	0.01µm	0.05µm	0.5µm	0.05µm

Both a single element and a nine element array were modeled. The results of the modeling show a resonance at approximately 42 MHz with 101% bandwidth. This

response is very similar to the KLM model response, and improves our confidence in the modeled dataresponse.

The impedance and phase angle as a function of frequency were also modeled and compared to the measured values at resonance (see Chapter 3.4.4). It must be noted that the change in the impedance at resonance is not substantial, and the change in the phase angle is only a one degree change, according to the model. This is due to the small size of the transducer and the small Q value. This makes it increasingly hard to detect the signature of the resonance in the impedance plot using a conventional impedance analyzer.

In order to simulate imaging output, and estimate resolution by modeling the appearance of imaginary reflectors in space, the device was modeled using Field II, a software package developed by Joergen Jensen (Technical University of Denmark) that is run in MATLAB. Field II can be used to predict the center frequency, bandwidth, and the pulse duration of the transmit and received beam. It can also be used to predict the shape and size of imaged reflectors. The dimensions and the material types of the transducer were input into the code and three infinitesimally small imaginary spherical reflectors were placed in two-dimensional space. The response of the transducer was then plotted. The calculated images of the reflectors are shown in Figure 3-6.

The axial resolution of the image is extremely good; this is due to the high working frequency. The axial resolution scales with frequency, as was noted in chapter 1. The lateral resolution of nine elements is not as of high quality, and the dots appear as fading lines. This is due to the small number of elements; as the number of elements was increased in the model the images became increasingly spherical in shape.

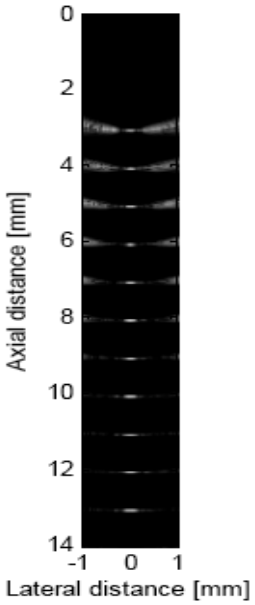

Figure 3-6: Simulated image of three reflectors using Field II for a 9 element array.

This is due to the fact that the aperture of the array is small. [2] As the aperture increases the lateral resolution scales up [3]. If the number of elements is increased to 128 the reflectors appear more spherical as shown in Figure 3-7.

Figure 3-7: Simulated image of three reflectors using Field II for 128 element array.

The improvement in lateral resolution is substantial due to the increase in the size of the aperture.

Field II can also be used to cross-check the KLM predictions for the 9 element array. The pulse echo pressure field with frequency and the pulse duration are shown in Figure 3-8.

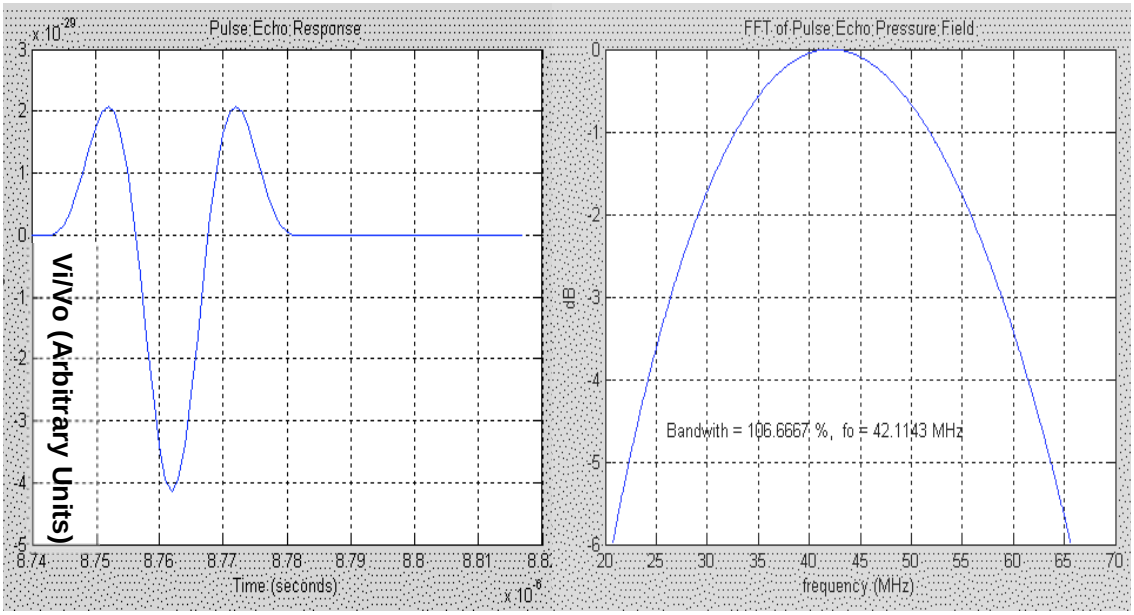

Figure 3-8: Field II model response in time (left), and frequency (right). Courtesy of Richard Tutwiler.

The results from all three models are very similar. The center frequency is approximately 50MHz, and the bandwidth is about 100%, with very little ringing on the time curve. These results are extremely promising and indicate that the device will function as proposed.

3.3 1D Transducer Fabrication Process

The transducer fabrication was done in collaboration with the Jackson group in electrical engineering at Penn State University. The film deposition and characterization as well as the electrical device characterization was performed at the Materials Research Laboratory, and the lithography and contact layout of device was done by collaborators at electrical engineering.

In order to fabricate the 1D transducer, 0.4-0.6 μm thick PZT films were deposited on $Si/SiO_2/Ti/Pt$ wafers. There were two sources of wafers used for this process, purchased 4" wafers from Nova Electronic Materials, Inc., (Richardson, TX), and 2" wafers fabricated in - house. The fabricated 2" wafers were made by thermally growing 3000 Å of SiO_2 (done by Hyunsoo Kim), and then sputtering a 300 Å Ti adhesion layer and ~700 Å of Pt electrode in a Kurt J. Lesker sputtering system. The Ti layer was deposited at 200 W and 5mTorr pressure of Ar gas sputtered for 200 seconds, and the Pt layer deposited at 200 W at 2.5 mTorr Ar gas sputtered for 600 seconds. Both layers were deposited at room temperature.

The piezoelectric film deposition was done by spin coating the ~0.75 M 2-MOE based PZT solution (see Chapter 2 for sol-gel process) at 3000 rpm. Each layer gives approximately 0.12-0.2 μm in thickness depending on the spin speed and exact solution molarity. In this way three to four layers were deposited to achieve the thickness of 0.5-0.6μm. The film was heat treated after each deposited layer with a three step heat treatment process: two pyrolysis steps at one minute each, one at 250 ^oC, and one at 350-400 ^oC; and one crystallization step for one minute in the RTA at 670 ^oC in air. The film was them sputtered with a 500Å thick Pt top electrode at 2.5mTorr pressure.

Dielectric properties and x-rays were collected on the films to determine that the properties were satisfactory.

During the second step of the process the film was masked in the shape of the transducer, and etched down to the bottom platinum, as shown in the optical image in Figure 3-9.

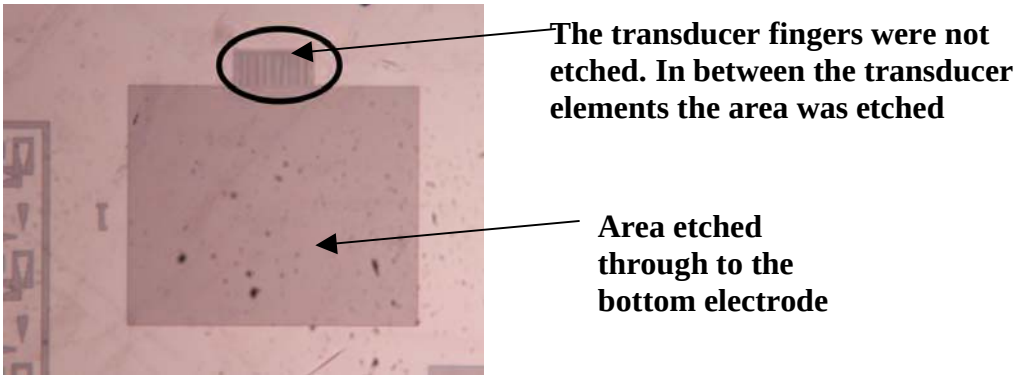

Figure 3-9: Image of the etched wafer. The top electrode and the PZT was etched in the areas around the transducer elements, leaving the elements intact. Image taken by Hyunsoo Kim

Because the dielectric constant values diminished, and the shape of the hysteresis loop suffered a deformation and, as discussed in Chapter 3.4.2, the wafers were annealed at 600 ^{o}C for one minute after this step in order to recover the ferroelectric and dielectric properties.

The wafer was then coated with SiN_x. Vias were patterned on the tips of the transducers to allow for top electrode contact, and the SiNx was removed from the rest of the transducer. An SEM image of the vias is shown in Figure 3-10. A large bottom electrode pad is also left uncovered to serve as the contact to the bottom electrode.

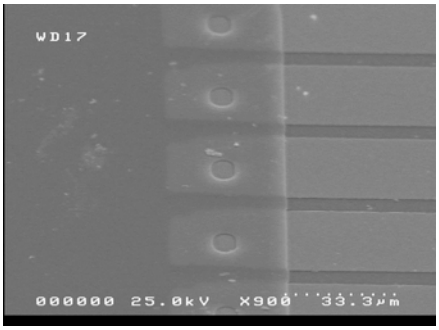

Figure 3-10: SEM image of the SiN_x insulating layer covering the tips of the transducers with vias. SEM taken by Hyunsoo Kim

The SiN_x is deposited in order to isolate the bottom and top electrode traces with a lower permittivity dielectric than PZT. In order to deposit the top electrode traces to contact the transducer fingers, the wafer was then sputtered with Cr/Au, patterned, and etched. This is shown in Figure 3-11, Figure 3-12 and Figure 3-13.

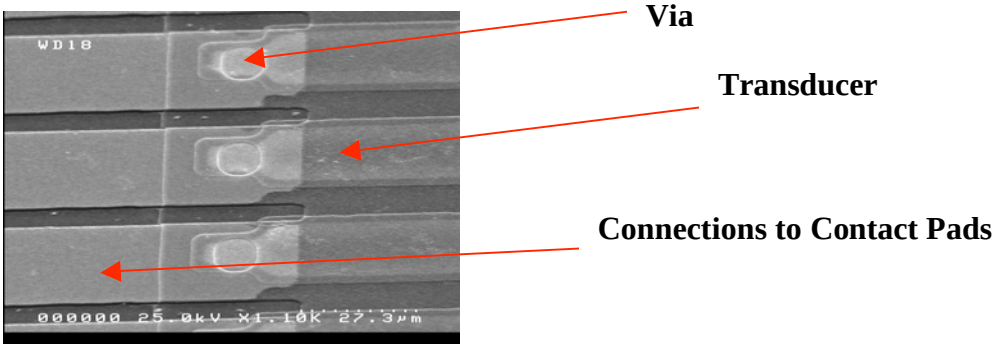

Figure 3-11: Image of the top electrode contacts that run through the vias onto the top Pt on the transducer fingers. SEM taken by Hyunsoo Kim

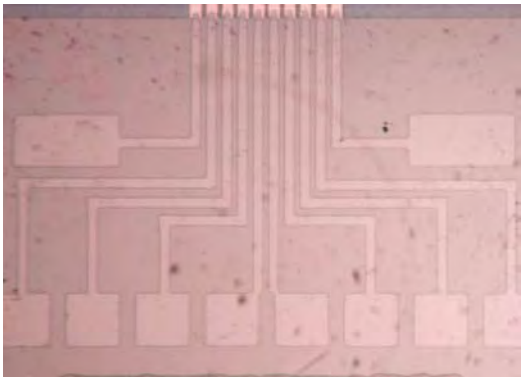

Figure 3-12: Image of the transducer contact pads. SEM taken by Hyunsoo Kim

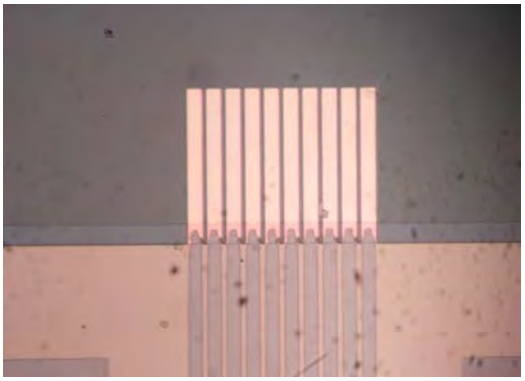

Figure 3-13: Image of the transducer elements. SEM taken by Hyunsoo Kim

Then the transducers were partially released from the substrate to make them into a T-bar shaped structure. This was done by partially removing the SiO_2 and Si via RIE and XeF_2. SEM images of the released structures are shown in Figure 3-14. The flow chart of the overall transducer fabrication process is shown in Figure 3-15.

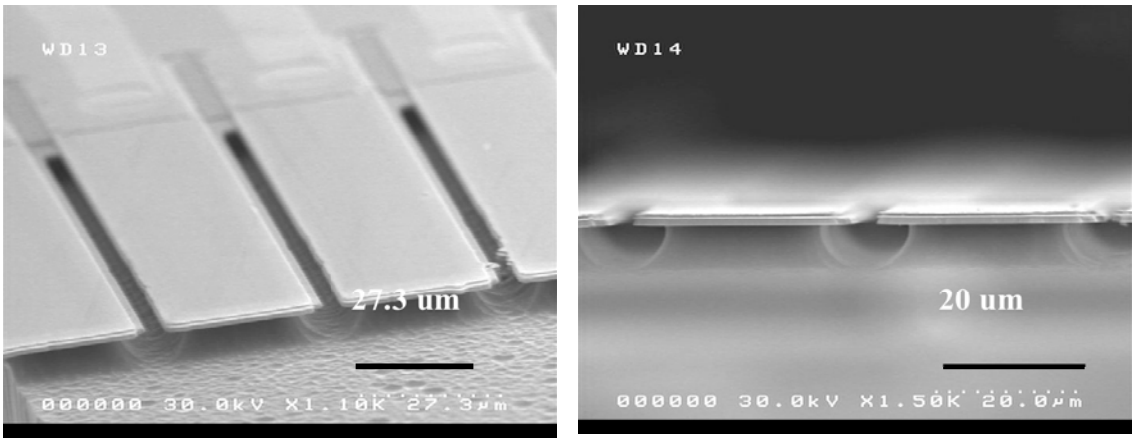

Figure 3-14: SEMs of the released xylophone transducers. SEMs taken by Hyunsoo Kim

When the transducer fabrication was completed, the wafer was cut into the individual devices and was mounted and wire bonded to a 16-pin connector. Some of the device and the traces were then coated in paraxylene ($C_6H_4(CH_3)_2$). This served as

protection from the water for the pulse-echo measurement. Ultimately, paraxylene could also be used as a kerf filler.

In order to test the functionality of the device after packaging first the capacitance and loss as a function of frequency were measured between 0.1-100KHz on the HP 4192A. The ferroelectric properties were also measured on individual elements using the RT-66. Impedance measurements to determine resonances were collected on the Agilent 4194A and 4294A, at first using clamp connectors and later using a special fixture for the 16-pin socket.

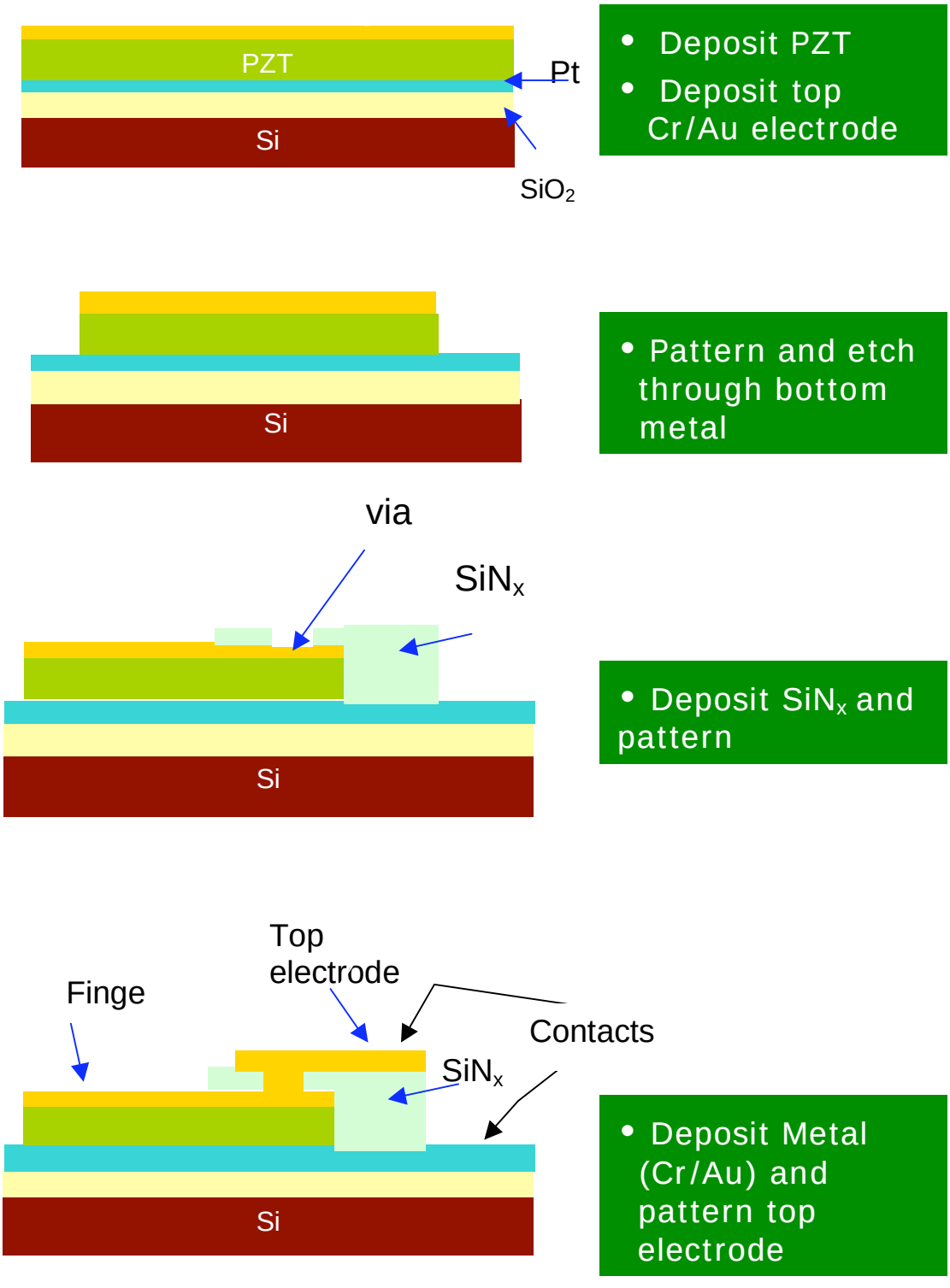

Figure 3-15: Flow chart of the 1D transducer fabrication process. Figure by Hyunsoo Kim

3.4 Results: 1D Transducer Properties

An image of the completed and packaged and parylene coated device is shown in Figure 3-16.

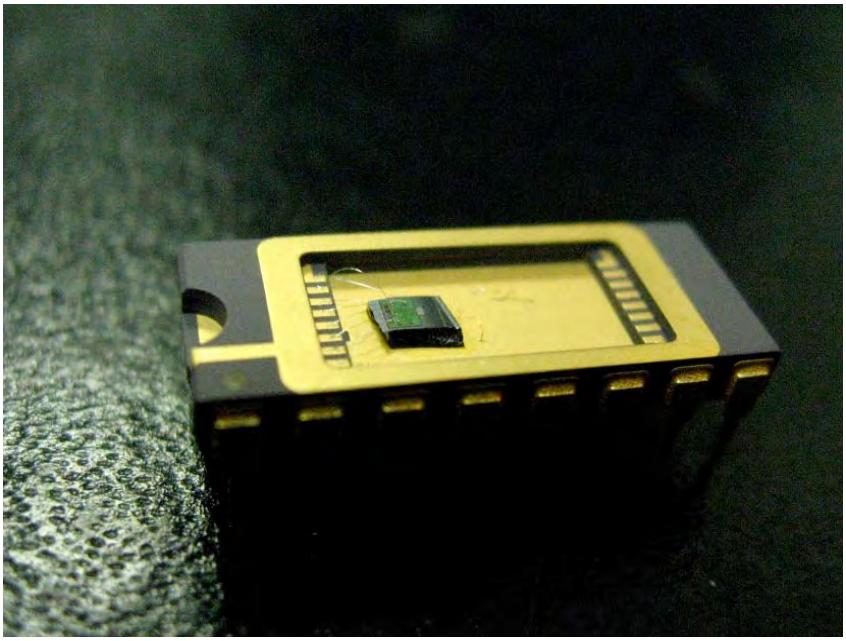

Figure 3-16: Xylophone transducer packaged in a 16-pin connector prepared for testing

3.4.1 X-ray diffraction

In order to determine the phase purity of the PZT films, x-ray characterization was performed using the Scintag x-ray diffractometer (Scintag, Inc., Sunnyvale, CA). Ni-filtered Cu Kα radiation was used and x-ray diffraction data were collected between 20° and 65° 2θ at a rate of 2° 2θ/min. The x-ray pattern is shown Figure 3-17. This is a pattern of a phase pure perovskite PZT 52/48.

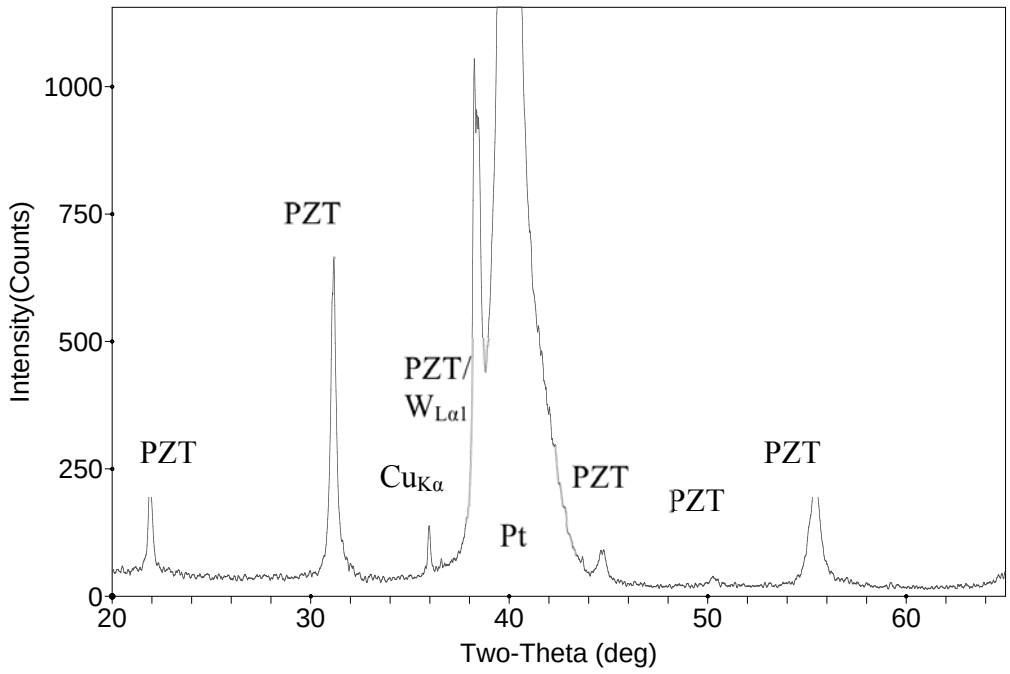

Figure 3-17: X-ray pattern of a PZT film on a Si/SiO_2/Ti/Pt wafer made to pattern into the xylophone shaped transducers.

3.4.2 Dielectric Constant and Loss 1-100KHz and Hysteresis Loop

The devices were tested for dielectric properties and the hysteresis was plotted to determine that the properties were satisfactory. The electrical characterization was performed after the Si/SiO_2 release step, and the results are shown in Figure 3-18 and Figure 3-19. The dielectric constant and loss of this particular sample at 1 kHz are about 1600 and 2.5%, respectively. The hysteresis loop values gave P_r^+~23.5 μC/cm^2, P_r^-~36 μC/cm^2, and the coercive field E_c^+~60 kV/cm, E_c^-~37 kV/cm.

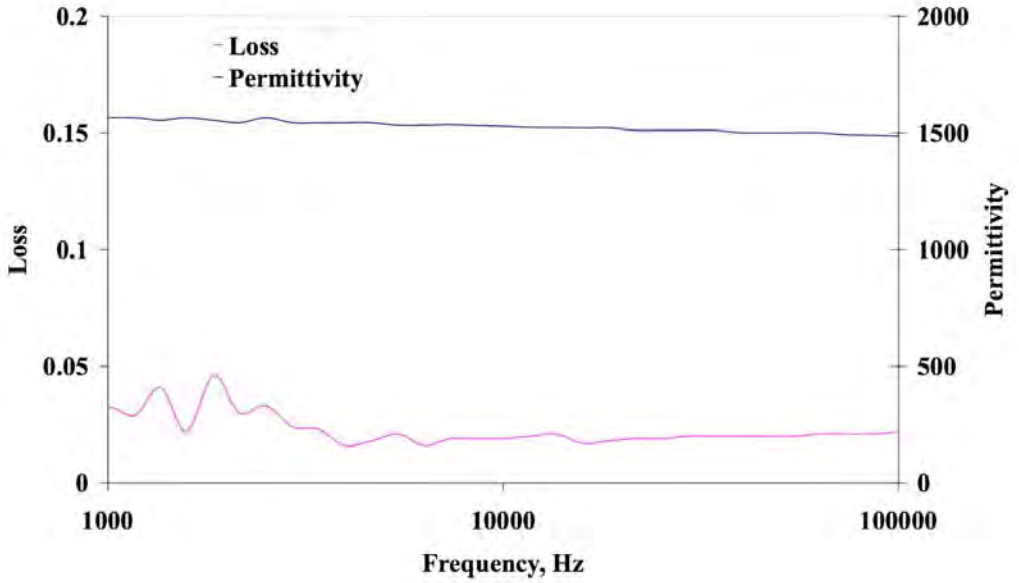

Figure 3-18: Permittivity and loss as a function of frequency on an individual transducer.

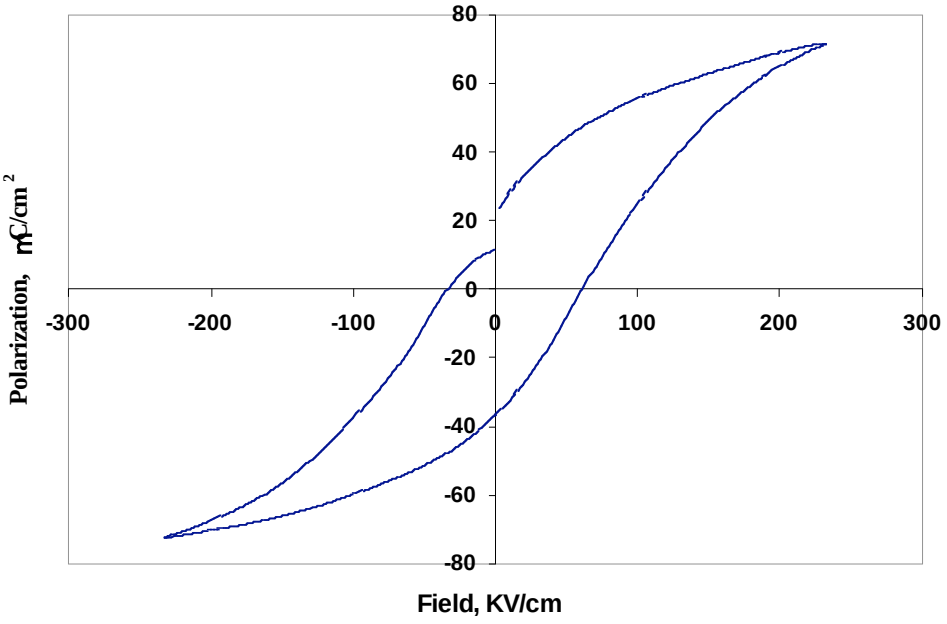

Figure 3-19: Hysteresis loop of a xylophone finger

The first sets of devices had much lower P_r and E_c values, and the hysteresis loops were often strongly pinched. An example of such a loop is shown in Figure 3-120. This may be caused by bombardment damage [4]. This problem was overcome by annealing the films at 600-700 ^oC for 1 minute after the etching step. A similar pattern was noticed in the dielectric constant of the devices. If the device was not annealed the dielectric constant would average about 600-700. Annealed samples would usually give a minimum dielectric constant of approximately 900-950.

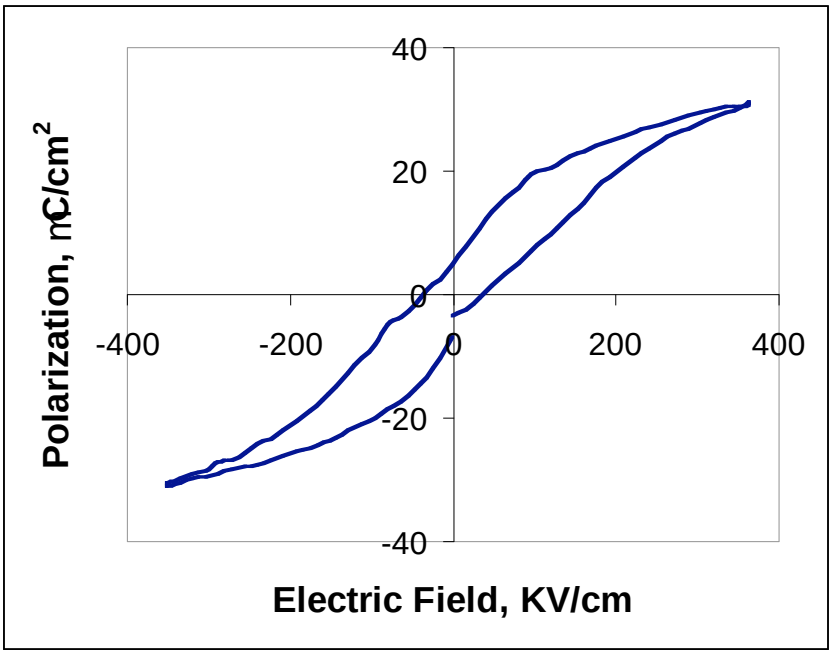

Figure 3-20: A pinched hysteresis loop of a device.

In summary, the PZT on the device wafers appears to be of reasonably high quality, and would be expected to have $e_{31,f}$ coefficients of –5 to –7 C/m^2.[2,5] As a result, the films with square hysteresis loops with large remanent polarization values are expected to function as intended in the transducers. It should be noted that the samples with pinched hysteresis loops should have small remanent piezoelectric coefficients.

3.4.3 Pulse-Echo Measurements

The pulse echo measurements were done in collaboration with Richard Tutwiler from the Applied Research Laboratory at Penn State. These were performed in a water tank using a steel plate as a reflector. The schematic of the layout of the measurement is shown in Figure 3-21.

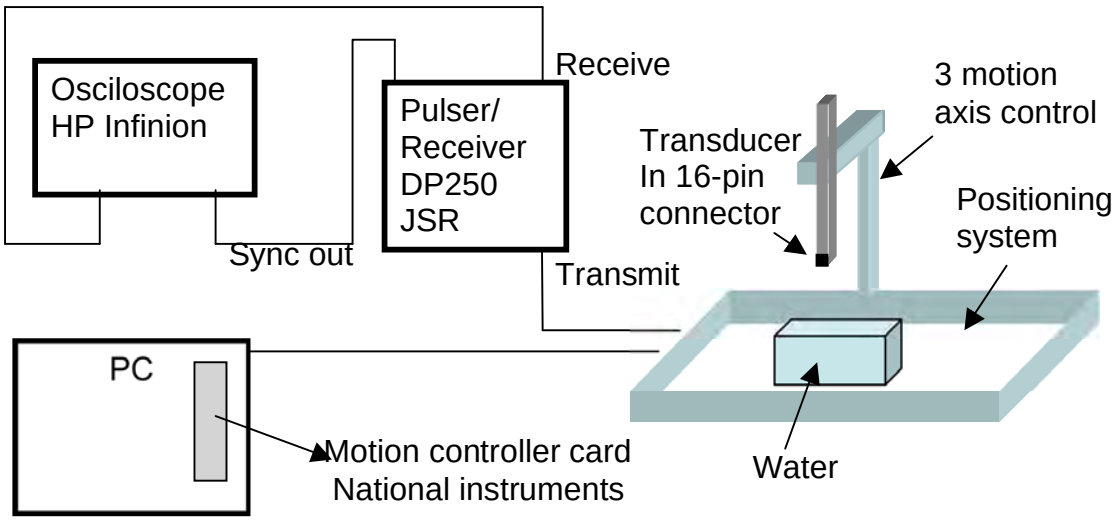

Figure 3-21: Pulse echo measurement system schematic

For these measurements, the transducer was coated in parylene, and attached through a 16-pin connector onto the rod that goes into the positioning system (see Figure 3-22). A steel plate was placed into the deionized water tank and the transducer was lowered until it was only a few millimeters away from the steel plate inside the water. A single -3 V pulse of 20 ns duration at 50 MHz was then used to excite the transducer, a transmit/receive switch attached to the pulser/receive switched between the two modes automatically, and the received signal superimposed on the transmit signal was imaged on the oscilloscope. Because the voltage from the transmitter was developed for bulk

ceramic measurements, it had to be attenuated from 100V to 3V. This was done by putting voltage attenuators in series to step the voltage down.

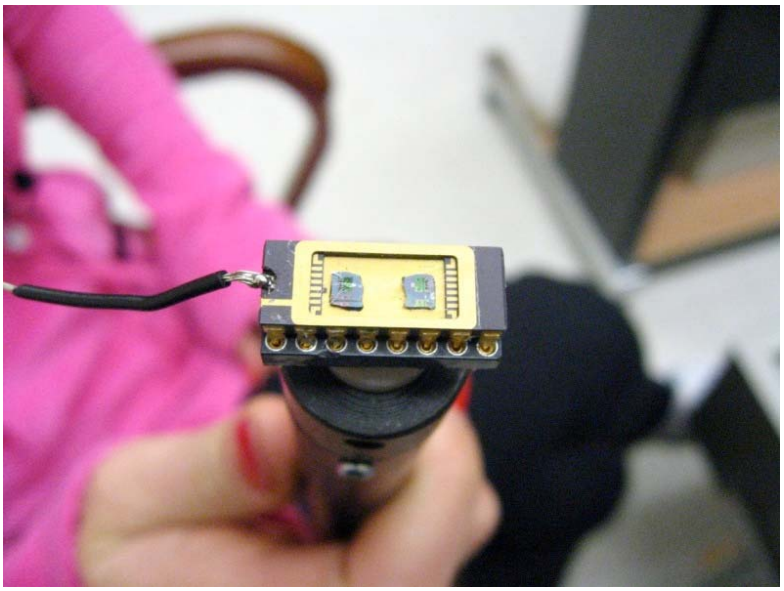

Figure 3-22: A packaged transducer device mounted into a 16-pin connector attached to the 3-axis motion control system

Prior to the measurement, the fingers were poled by applying 6V DC for 15 minutes at room temperature. Several attempts were made to make this measurement. In particular, the distance between the steel plate and the transducer was changed. The coupling media was also varied from water to a special ultrasonic gel, the connectors and the transducer were isolated from the coupling medium by coating the whole active and passive area with parylene to avoid shorting through the water. Despite all the alterations there was no response signal detected by the transducer. It is not clear why this is the case. Clearly additional work should be pursued here, possibly with a larger number of elements being driven.

3.4.4 Resonance Measurements 10-100MHz

High frequency measurements were also made by characterizing either the capacitance and loss or the impedance and phase angle as a function of frequency up to 100MHz. It was found that measurements performed using clip connectors and approximately one meter long cables on the Agilent 4294A provided erroneous results (See Figure 3-23 and Figure 3-24). The apparent resonances in reality do not correspond to the device, but rather to the leads and the impedance analyzer, despite the compensation for the short and open prior to the measurement.

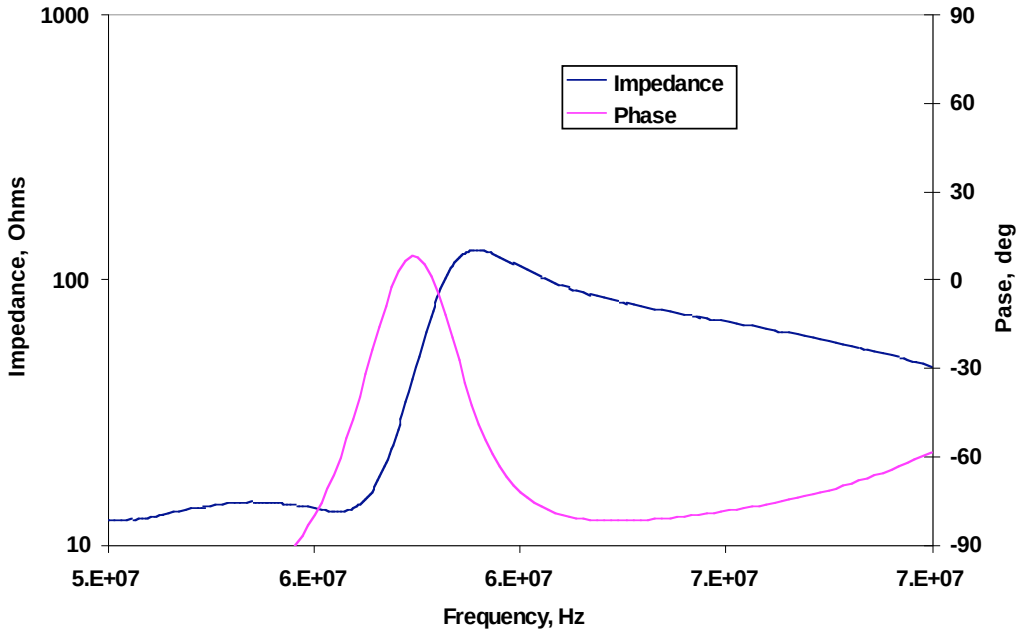

Figure 3-23: Impedance and phase angle as a function of frequency in the 50-70MHz range

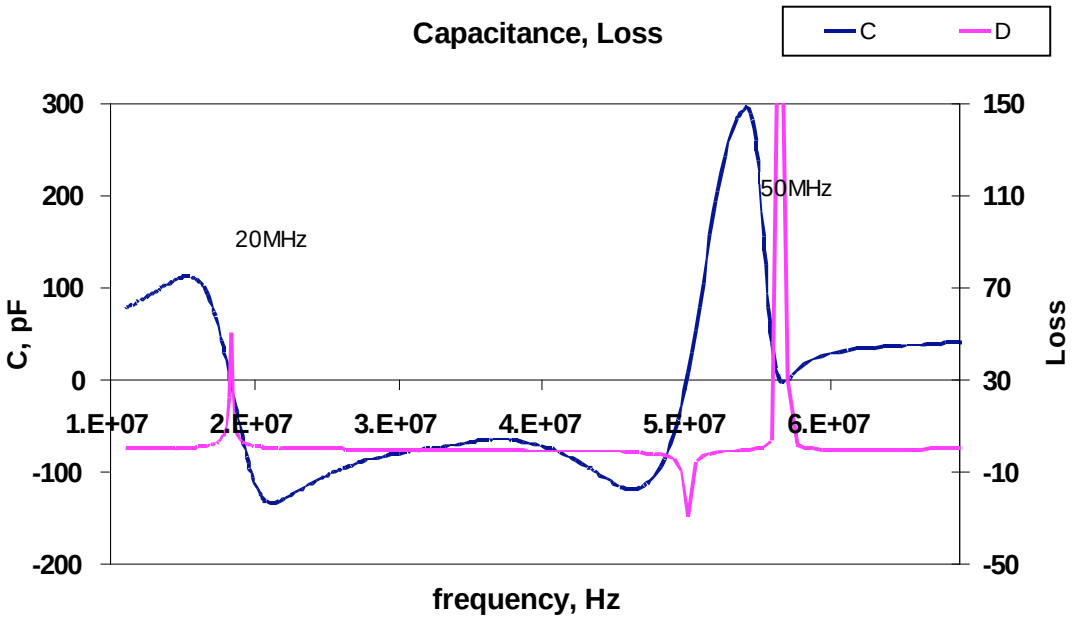

Figure 3-24: Capacitance and loss as a function of frequency in the 10 – 70 MHz range

To minimize errors in the high frequency measurements, it was found that the cables need to be eliminated. For this purpose, a special fixture was fabricated with the help of Paul Moses. The 16-pin connector plugged directly into the fixture. The fixture was designed in such a way that the contact wire lengths did not change or changed very little from the calibration to the actual device testing. Also the back of the fixture was insulated from mechanical shocks by gluing a half inch thick Styrofoam pad at the bottom. In this way, human error and artifacts associated with resistance-capacitance resonances are reduced as much as possible. Probing of the sample was done using the device shown in Figure 3-25. The image of the new fixture is shown in Figure 3-26.

Even with the improved fixturing, it is not obvious that it will be straightforward to detect the resonance via impedance analysis. In particular, the resonating element is quite small. In addition, because the transducer was modeled to have a >100% bandwidth, it is possible that the resonance impedance is low and

washed out enough that it would be hard to detect. In order for the bandwidth to be wide the quality factor needs to be small, Q is defined by,

$$Q = \frac{F_r}{F_2 - F_1}$$ **Equation 3-1**

where F_r is the frequency at resonance and F_2 and F_1 are the frequencies at a certain bandwidth level usually -3, -6, -20, and -40 dB level. If the resonance peak is broad the denominator will dominate, making Q small.

To estimate the importance of Q, the impedance change associated with the resonance for model piezoelectric resonators was calculated using an effective medium model. It was found that the signature in the impedance becomes very (undetectably) small for Q values approaching one. However, it has been demonstrated by other groups that pulse-echo responses can still be generated from probes without easily measured impedance changes; thus, they can be used for imaging [6].

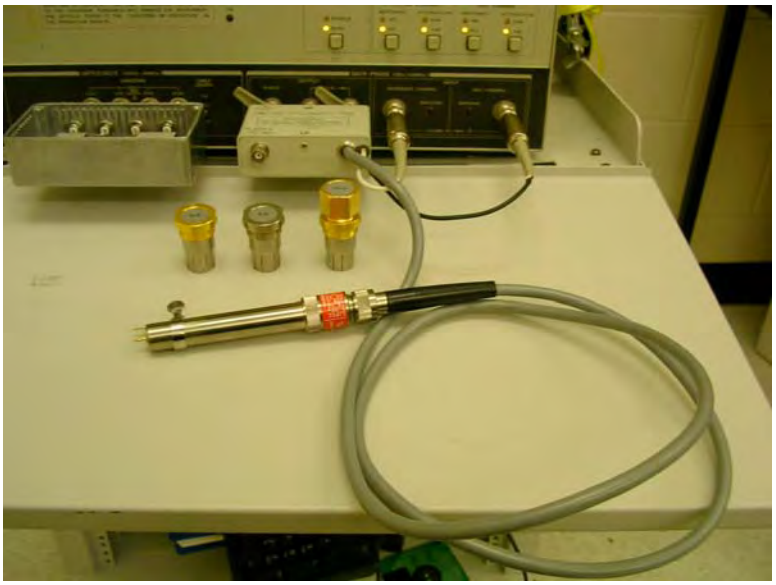

Figure 3-25: Probe used for the impedance measurements on the 4194A

The capacitance and loss as a function of frequency were measured on an Agilent 4194A. The results obtained from this measurement were compared to a standard 120pF capacitor soldered to the fixture. This is approximately the same capacitance as a single finger, and serves as a means of testing for RC or LC resonances associated with the fixturing, rather than piezoelectric activity. The capacitance and loss values and curve shapes of the device were measured and compared to the reference capacitor.

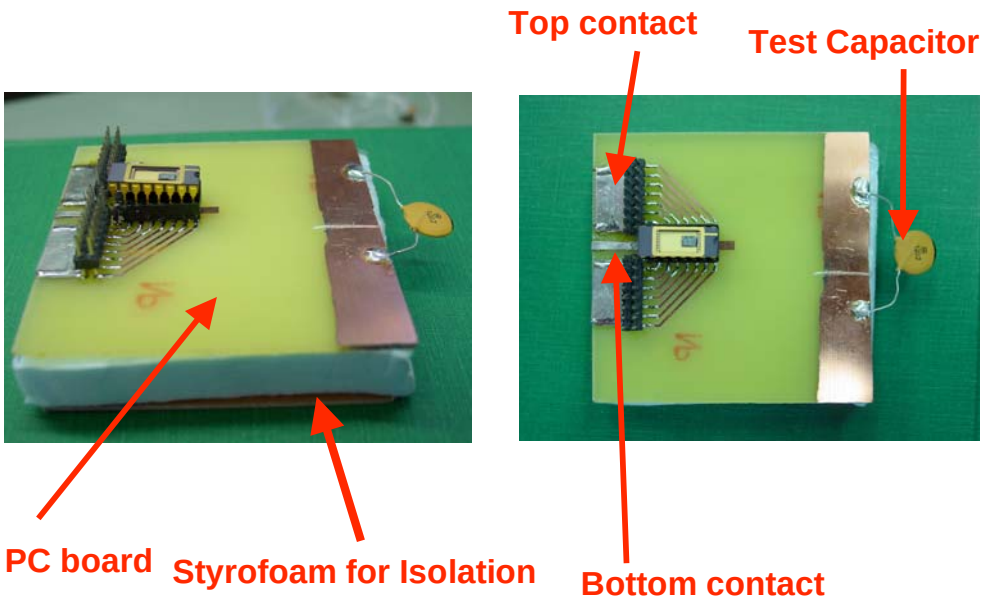

Figure 3-26: Fixture for high frequency measurements on transducer

The measured data from the transducer were fitted to 2^{nd} , 3^{rd} and 4^{th} order polynomials. The polynomial curves were then subtracted from the data in order to reduce the background as much as possible. The polynomial curves and the data are shown in Figure 3-27. The 3^{rd} order polynomial was used for the subtraction, as the 2^{nd} does not give a good enough fit. Unfortunately, this background subtraction did not highlight the

presence of any pronounced resonances in either the capacitance or loss tangent. However it must be noted that the FEA impedance (shown in Figure 3-28) also shows only a very small change in the impedance. The phase angle shows a change of one degree at resonance of ~25MHz.

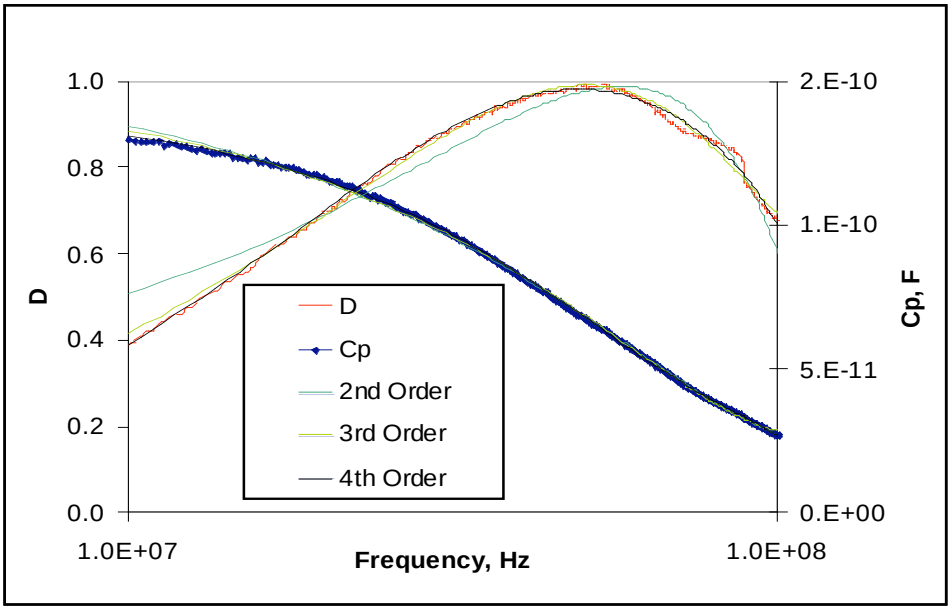

Figure 3-27: Resonance data with 2nd, 3rd, and 4th order polynomials overlaid.

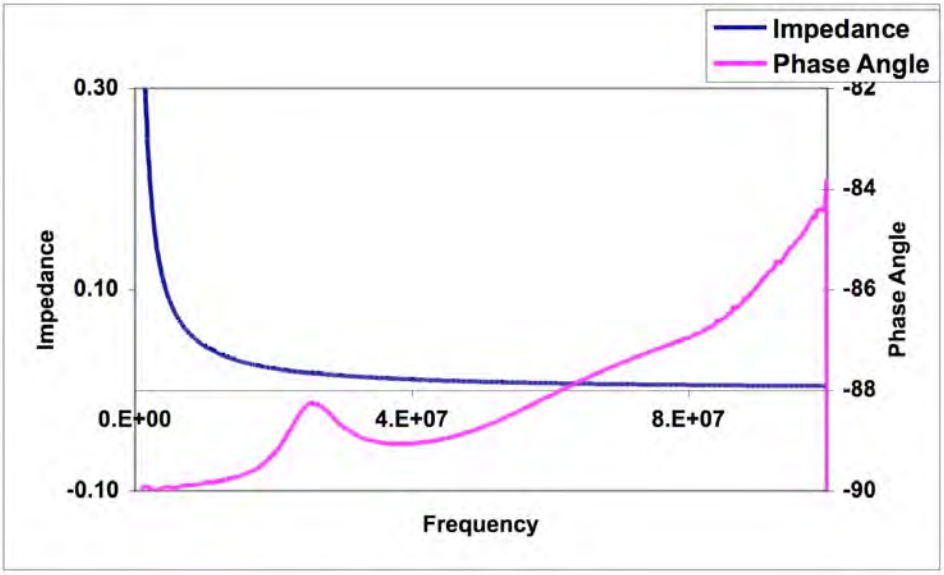

Figure 3-28: The calculated using FEA, and the measured impedance and phase angle xylophone transducer.

If the impedance curve generated from the finite element analysis is fitted to a power law and the background is subtracted from the data, a small resonance becomes visible; the change in the impedance value is on the order of 10^{-5} Ohms. Such a small resonance would be very hard to detect using even the sensitive fixture that was developed for the measurement. Moreover, any inhomogeneity in the dimensions of the sample would be likely to further broaden the impedance and phase angle response associated with the resonance, which would further complicate detection. It is likely that some combination of the small resonator size, imperfections in the patterning, extra resistance associated with the electrodes, and/or degraded PZT quality is responsible for failure to detect impedance and phase angle changes in these initial measurements.

3.4.5 Electrode Failure

Another complicating factor observed during the measurements was failure of the electrode traces. When they did so, they failed as an "open," and this usually happened at the base where the gold lead attached to the transducer element, as shown in Figure 3-29. This probability of failure increased when a high triangular voltage was applied during the hysteresis measurements. It was found that the breakdown strength depended on the size of the elements and batch. Usually it was on the order of tens of volts, fields that the PZT element usually survives (indeed comparable to the values used to pole the piezoelectric under normal circumstances). In addition, failure was also observed on application of much lower voltages during high frequency measurements. At first, 0.5V was used for the high field measurements, the electrodes

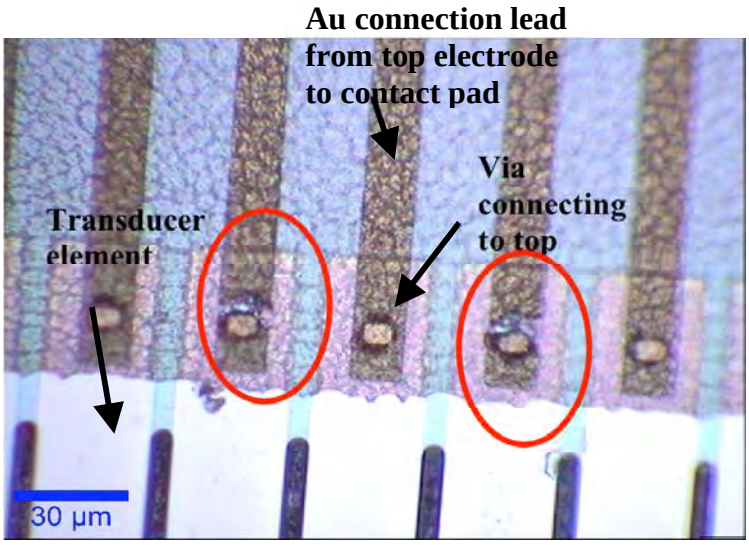

Figure 3-29: Optical image of a transducer array after a series of characterization attempts on different electrodes. Failure points are circled in red.

started to break down after a single measurement. The voltage was then changed to 5mV for further measurements. This greatly reduced the amplitude of the piezoelectric response and complicated electrical measurements considerably.

The origin of this failure is unclear, and could potentially be batch dependant. This needs to be investigated further in order to produce devices that would function at high frequencies.

3.4.6 Pulse-Echo Measurement Using the HP 4194

A more sensitive measurement was suggested and executed with the help of Paul Moses given the reduced excitation voltages that could be employed. In order to do this two elements were used, one as the transmitter and the other one as the receiver. No coupling media was used in this measurement, and the majority of the signal was expected to couple through the Si substrate, as it is better coupling media than air. The fixture for the experiment is shown in Figure 3-30. The two coaxial connectors were connected to the input “Test” and “Response” the third connector was connected

through a short coaxial cable to the “single” output. The transmit element was excited by a sine wave voltage of 0.005V, the projector element was then connected to the response and a measured signal would be detected from that transducer. The “test” measures the output voltage and compares it to the response.

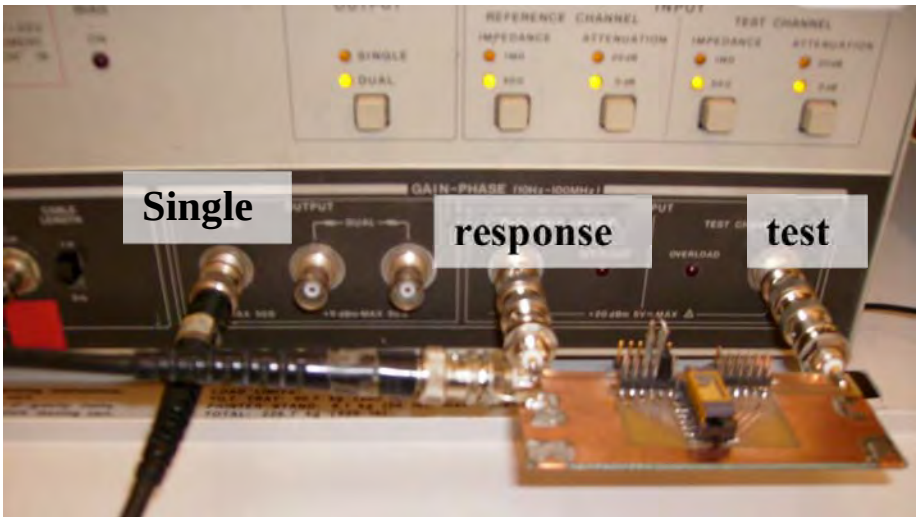

Figure 3-30: The gain phase experiment set up to examine coupling of two transducer fingers through the substrate.

The Test/Response (T/R) and the gain phase are plotted against frequency. Assuming there is true coupling between the detector and projector elements, the phase gain signal of two transducers poled in one direction and two transducers poled in opposite directions will vary in the angle. In theory the signals should be received 180^0 out of phase.

The transducer elements were tested for capacitance and loss at 1 kHz, the hysteresis loops were plotted, to ensure that they were not faulty in any way. The elements were then poled at three times the coercive field for fifteen minutes. The measurement was performed with an input oscillating voltage of 5mV. The result of plot of the gain phase and as a function of frequency from 10 to 100MHz is shown in

Figure 3-31. The signal for both transducers poled up, both poled down, and one up and one down were measured. The signals of the gain phase were then subtracted from each other to examine small changes in the phase angle.

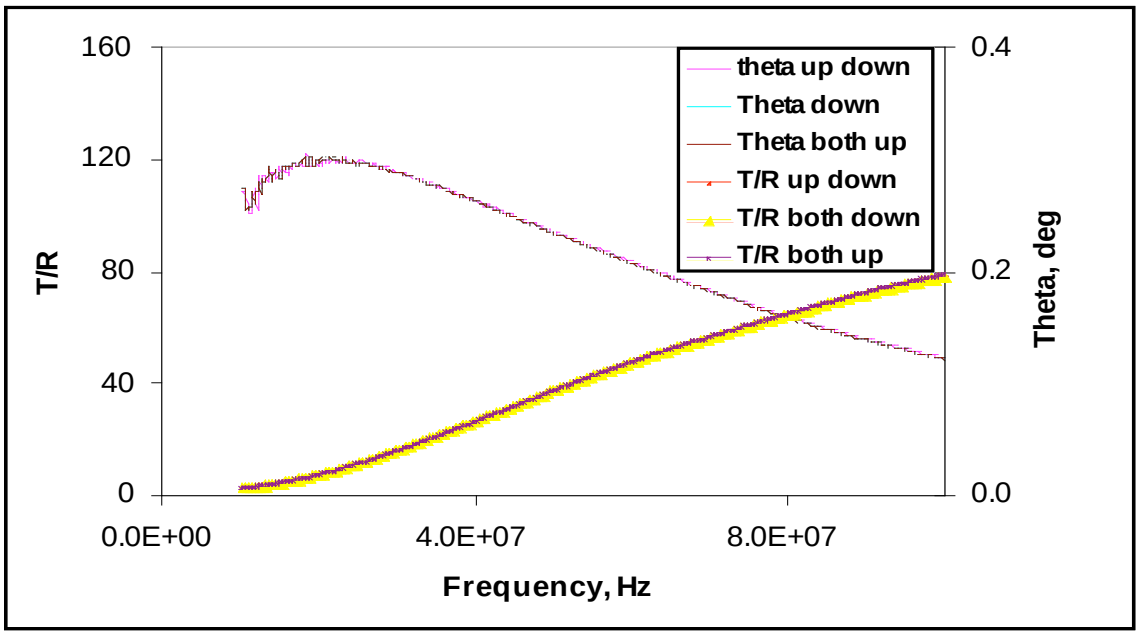

Figure 3-31: The gain phase and T/R signal as a function of frequency for the xylophone transducer

The subtracted signals from both transducer poled up and one up one down gave a phase increase of two degrees between 30 and 70 MHz, the subtracted data from the signals from the transducers both being poled down and one up and one down gave no net difference in gain phase angle. It must also be noted that as described in section 3.4.5 it was impossible to drive the transducer at a high alternating voltage at high frequencies because the traces running to the transducer would fail open. It is possible that the measurement would have given a response had we been able to drive the transducer with a higher voltage. Thus, it will be important in the future to repeat these measurements with higher drive voltages on transducers with improved electrode

structures. In addition, it would be ideal in those measurements for the transducer fingers not to be undercut by a XeF_2 release step. This will insure that there is maximal mechanical coupling from one element to another.

3.5 Conclusions

A method of fabricating a one-dimensional array is discussed. This design has a center frequency of 50MHz and has beamforming and beam steering capabilities in two dimensions. The elements of this transducer array are made up of rectangular shapes partially released from the Si substrate. The width mode was chosen as the resonating mode, and in order for it to resonate at 50MHz, the width dimension was set to 30 microns based on the modeling. The other dimensions of the device were made to be far away in resonant frequency from the desired 50MHz in order to achieve isolation of resonances.

The beam steering and forming capability imposes a requirement on the design that the pitch of the elements is less than half a wavelength of operation. This can be accomplished using lithography, and micromachining of a piezoelectric film rather than the conventional dicing of a ceramic. Lithography was also used to lay out the interconnects and contact pads. It is recommended in the future that a design change to allow the device to operate in its length extensional mode be considered, as this would allow the correct $\lambda/2$ element spacing required for focusing.

The dielectric constant and loss properties of the device were measured to be 800 - 1500 and ~3% respectively, depending on details of the processing. The measured hysteresis loop shows values of polarization to be P_r^+~23.5 $\mu C/cm^2$, P_r^-~36

μC/cm^2, and the coercive field E_c^+~60 kV/cm, E_c^-~37 kV/cm. No resonances could be detected in the impedance data as a function of frequency, even after removal of the cables. Additional work on pulse-echo measurements should be undertaken in the future on devices with more robust electrode structures.

References

1 H. L. W. Chan and J. Unsworth, IEEE International Symposium on Applications of Ferroelectrics proceedings. **,** 277-280 (1986).

2 S. Trolier-McKinstry and P. Muralt, Journal of Electroceramics **12,** 7-17 (2004).

3 J. A. Zagzebski, *Essentials of Ultrasound Physics* (Mosby, 1996).

4 C. Soyer, E. Cattan, D. Remiens, and M. Guilloux-Viry, Journal of Applied Physics **92,** 1048-1055 (2002).

5 R. A. Wolf and S. Trolier-McKinstry, Journal of Applied Physics **95,** 1397-1406 (2004).

6 K. Snook, (Personal Communication, 2007).

4. Tube Structures: 2D Transducers

4.1. *Introduction*

One of the approaches used to fabricate high aspect ratio transducers for high frequency devices with small interelement pitch, a requirement for beam steering, was infiltration of the electrode and piezoelectric material into a Si mold. The structures were then heat treated to crystallize the oxide electrodes and piezoelectric and the substrate was partially released.

The structures are envisioned to have the geometry shown in Figure 4- 1, where each element is made up of three layers. The inner and outer electrode layers coat the piezoelectric. The solutions used in this process were $LaNiO_3$, a conductive oxide that can be used as electrode material[1], and $PbZr_{0.52}Ti_{0.48}O_3$ (PZT), a ferroelectric material with a high dielectric constant. By sandwiching the PZT between two layers of $LaNiO_3$ the structure could potentially be used as a piezoelectric upon the application of a bias to the inner and outer surfaces [2]. This chapter describes the process of preparing the piezoelectric structures for this purpose.

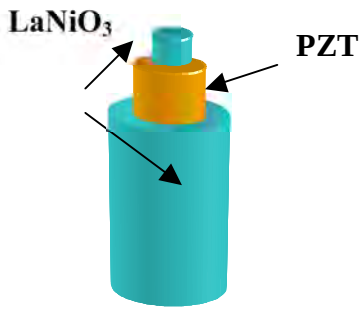

Figure 4- 1: Schematic showing the concentric tubes of $LaNiO_3$/PZT/$LaNiO_3$ sandwich structure

4.2. *Tube Structures: Experimental Procedure*

High aspect ratio piezoelectric structures were fabricated using an infiltration technique. This technique involved the use of prefabricated macroporous Si templates (Philips Research Laboratories, Eindhoven, the Netherlands, or Norcoda Inc., Edmonton, Canada). These were fabricated using the Deep Reactive Ion Etch (DRIE) process (Bosch process) [3].

A substrate is shown in Figure 4- 2. The intent was to infiltrate the mold with solution and then heat treat to form a crystallized material. The mold was then partially removed in order to achieve an array of a very high aspect ratio periodic structures attached to a substrate. The pores had 1.8-2.0 micron diameters with a pitch of 1.5 microns [2].

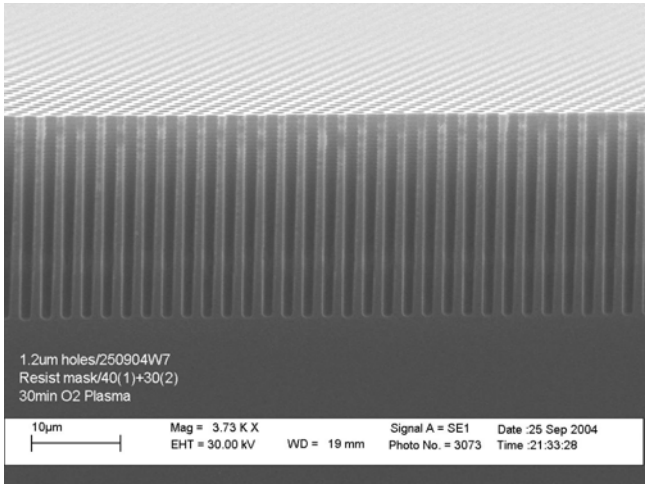

Figure 4- 2: Si mold substrates from Norcoda. Picture courtesy of S. S. N. Bharadwaja

4.2.1. Substrate Cleaning

During the tube fabrication process, several discrepancies were noticed that pointed to the fact that there was native contamination layer on the mold surfaces. First,

when the Si was removed to create the free standing tubes there was some surface film left behind that connected the tubes to each other at their tops. Secondly, while the PZT wall thickness increased linearly as a function of the number of infiltrations, the estimate of wall thickness did not extrapolate to zero for no infiltrations. To confirm whether there was a contaminant layer, a Si substrate was etched in XeF_2 *prior* to infiltration. As shown in the SEM images in Figure 4- 3 there is a skin of material remaining that suggests the existence of a contaminant layer on the Si.

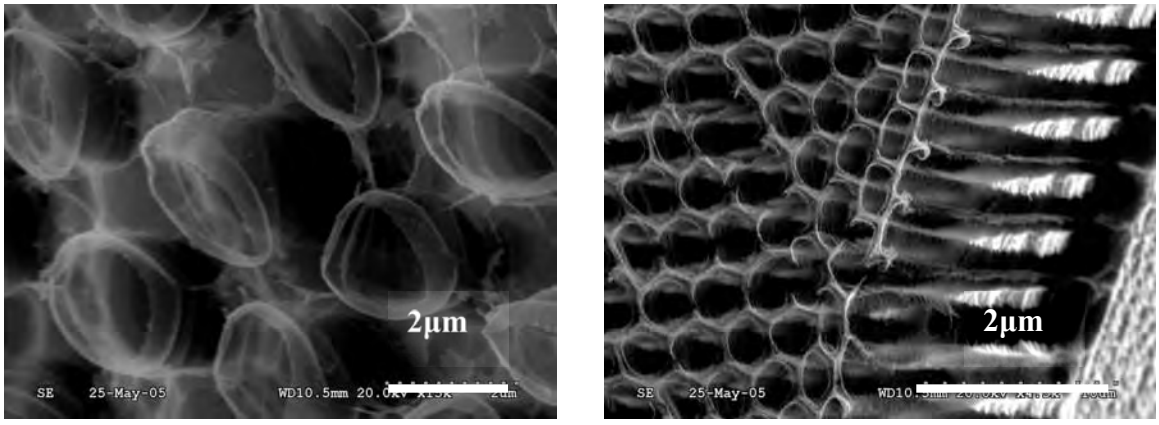

Figure 4- 3: SEM images of an etched Si mold *prior* to any infiltration. After the Si is removed, the sidewall of native oxide appears in the form of thin tubes.

In order to determine the best way to remove this layer prior to $LaNiO_3$ and PZT deposition, attempts were made to remove it either by use of a 10:1 buffered oxide etch (BOE) (J.T. Baker) which should remove SiO_2 or a reactive ion etch (RIE) oxygen plasma ashing to remove any organics that might remain on the sidewalls following the Bosch etch process. The gases used in the ashing process were 332 sccm of CF_4 and 77 sccm of O_2 at 100W power. The following conditions were used:

1. RIE 2 min CF_4/O_2
2. RIE 4 min CF_4/O_2

3. Vacuum assisted infiltration of BOE
4. Vacuum assisted infiltration of BOE and RIE for 2 minutes

All the samples were then etched in XeF_2, for thirty cycles, at one minute per cycle at 2Torr pressure. SEM images were taken to compare the results. The native oxide layer was removed after BOE infiltration and RIE for 2-3 min under these conditions. In Figure 4- 4 one can see the Si samples after etching. The remaining morphology is due to the isotropic removal of Si from the patterned substrate, and suggest that the sidewalls of the mold are substantially cleaner. Thus, in all subsequent experiments, the following protocol was used to clean the templates prior to PZT or $LaNiO_3$ deposition.

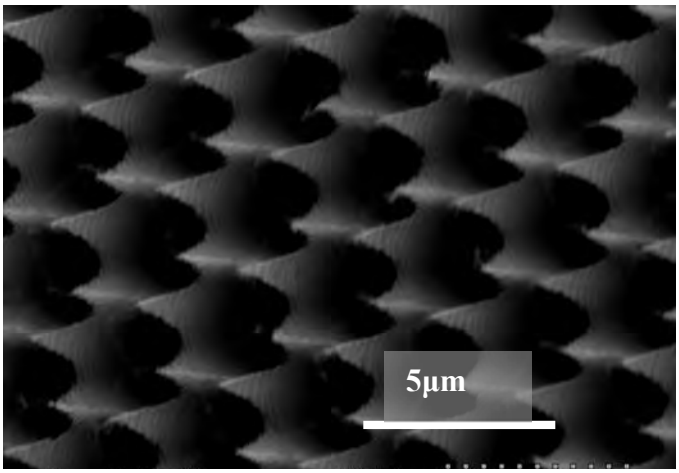

Figure 4- 4: Si substrate after removal of the native oxide and releasing with XeF_2. There are no signs of sidewall contamination.

4.2.2. PZT and Electrode Deposition

It was previously shown by Bharadwaja et al. [2] that simply immersing the templates in a 0.75 molar 2 methoxyethanol-based PZT solution led to incomplete infiltration (See Figure 4- 5). That is, after immersion, an oxide layer remains on the

substrate surface. Once a capping layer developed, further infiltration was impossible. Thus, in all depositions reported here, the sample surfaces after each infiltration were wiped with a cotton swab or a clean room cloth to remove the excess solution.

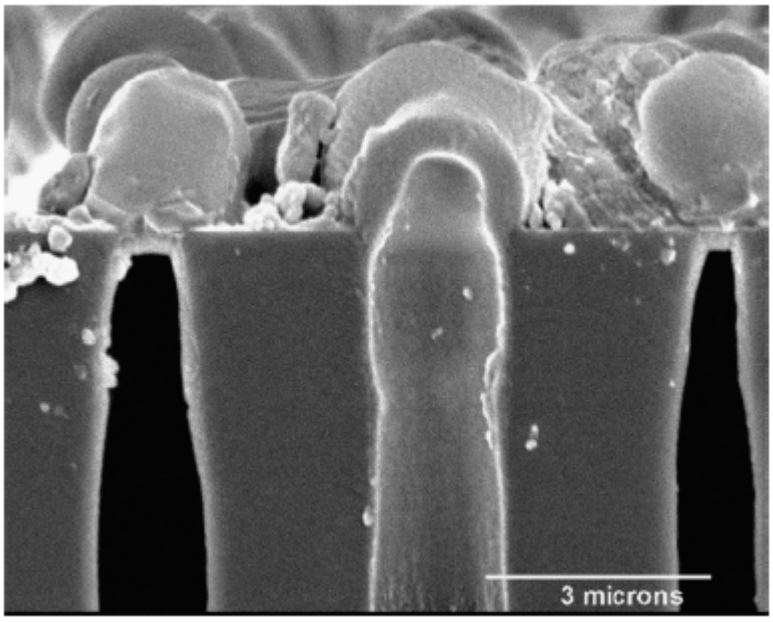

Figure 4- 5: SEM image of solution capped pores in a Si mold [2].

It is presumed that the capping layers formed because air trapped inside the pores needs to be displaced in order for the liquid to enter the tube. The surface tension of the liquid is sufficient to keep the liquid molecules together over the opening of the tube. In order to overcome this, a vacuum needs to be applied to decrease the partial pressure of air and force the air out of the tubes and allow the liquid to penetrate.

A schematic of the set up is shown in Figure 4- 6. To make this work, a closed container connected to a vacuum pump was used. The solution that is to be deposited was poured into the container and the Si mold was submerged in the solution. The container was sealed, and the vacuum pressure difference of ~80 kPa pressure was drawn over the

top. Bubbles of gas could be seen to rise from the sample surface, at first quite vigorously, and after a few minutes they would slow down, until the evolution of gas would stop. This method increased the deposition rate and overall wall thickness substantially, as observed in SEM. Despite this, complete filling of the tubes was never achieved. This is probably due to the fact that the shrinkage of the solution from the gel state to the crystallized ceramic is approximately 50-70% on a flat film [4], and is probably substantial in the tubes also.

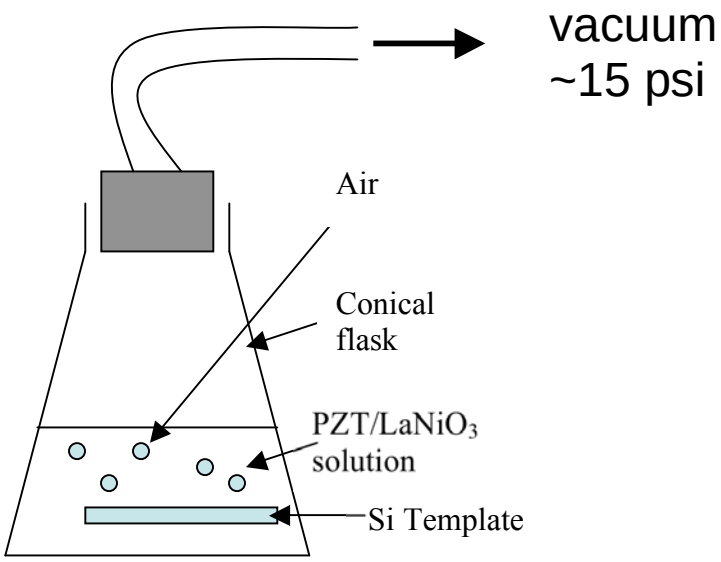

Figure 4- 6: Schematic showing the vacuum infiltration process

4.3. *Mold removal*

The mold was removed using XeF_2 gas. The removal was done in a Xactix e1 series etch tool (Pittsburgh, PA), using the following conditions: pressure 2 Torr, each cycle was 60 seconds, 15-20 cycles were performed in order to release the entire structure (~15-20μm). During each of these cycles the sample was exposed to XeF_2 for 60 seconds.

After that, the gas was removed and the chamber was then purged with N_2. The overall fabrication process flow chart is show in Figure 4- 7, and SEM images of the tubes are shown in Figure 4- 8.

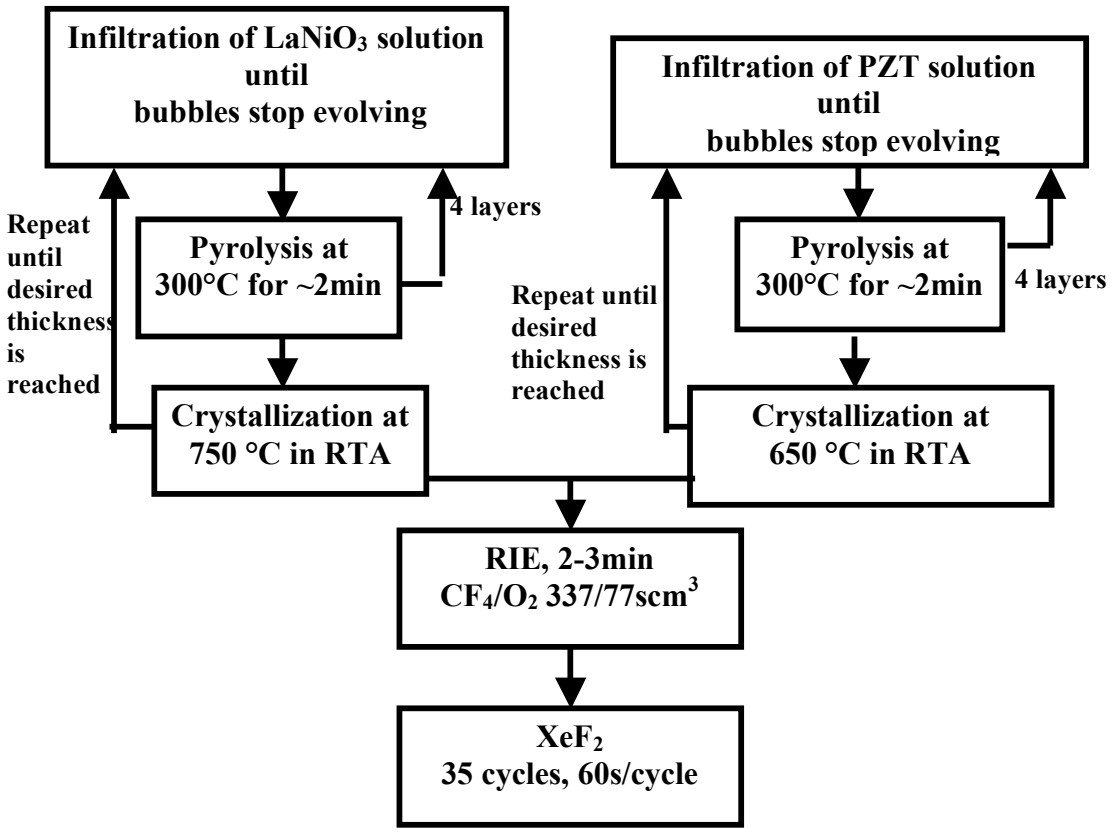

Figure 4- 7: Fabrication process flow chart of tube structures

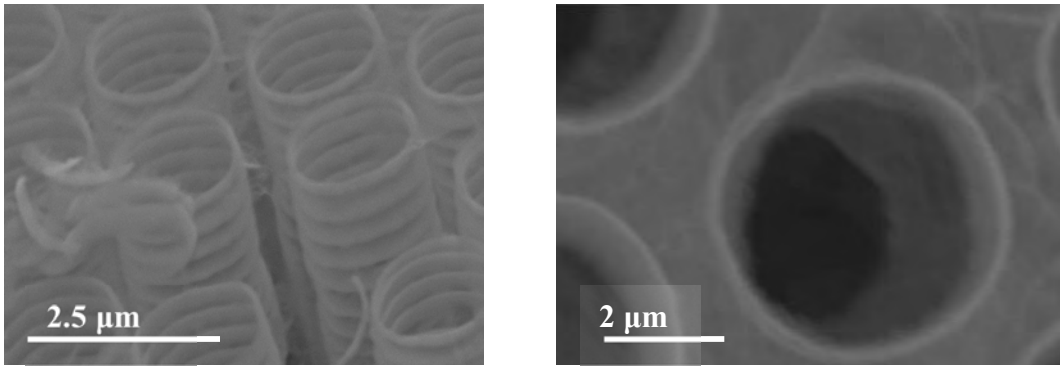

Figure 4- 8: SEM image of the $LaNiO_3$/PZT/$LaNiO_3$ tubes

The reason for the wall of the tube being ribbed is because of the deep-reactive ion etch process process for the Si, (Bosch process). The typical DRIE system entails having an inductively coupled power (ICP) source to provide a high-density plasma, and an independent substrate power bias to provide directional ion bombardment during the etch step [5]. This process is made up of two steps which are cycled. A protective layer of polymer is first deposited conformally by PECVD (Plasma Enhanced Chemical Vapor Deposition) [5] of trifluoromethane, CHF_3 polymer, and argon gas [3]. This is followed by the etch step, a simultaneous engagement of the substrate bias and flow of SF_6 or some other fluorine source (e.g. NF_3 or CF_4) and Ar [3]. During this step the sidewalls of the silicon trench are relatively protected by the polymer layer. The bottom of the trench being formed, although originally coated with polymer, is exposed to the reactant gases by the directional ion bombardment. The silicon is then "etched" chemically [5]. The iteration of these passivation/etch cycles allows the desired anisotropic features to be achieved. While in principle smooth sidewalls can be achieved using this process, in many cases, the resulting sidewalls of the Si have a ribbed structure.

4.4. *Characterization*

In order to determine the best conditions for crystallization of the $LaNiO_3$/PZT/ $LaNiO_3$ tube structures, the tubes were exposed to different crystallization conditions as summarized in Table 4-1. For these samples, 4 layers of $LaNiO_3$ were deposited by vacuum infiltration, followed by four layers of PZT, and another four layers of $LaNiO_3$. It was hoped that the $LaNiO_3$ electrode would serve both as an electrode and as a buffer

against reaction between PZT and the Si template during heat treatment. The initial pyrolysis steps were the same for all the samples, that is, 160 °C for 2 minutes, and 360 °C for 2 minutes on a hotplate in air. X-ray diffraction scans between 20°and 60° degrees 2Θ were performed on sample crystallized under different conditions.

Table 4-1: Conditions for crystallization of the $LaNiO_3$/PZT/ $LaNiO_3$ tubes

	Crystallization I	**Crystallization II**	**Substrate Pretreatment**
A	--	750°C 1min	No
B	--	750°C, 2min	No
C	650°C, 2min	750°C, 2min	Oxygen plasma 2-3 min

X-ray diffraction patterns of samples prepared using the original method of fabrication (as shown in the flow chart in Figure 4- 7) revealed a poorly crystallized perovskite phase, as well as some residual carbon fluorides (the XRD peak above 36° was a good match to the fluorocarbides with $6 \leq x \leq 10$, as well as the polymer Ploytetrafluroethylene, $(CF_2)_n$.). This corresponds to the sample A in Figure 4- 9. This peak is clearly visible in x-ray A and B. Only the template in sample C was pretreated in oxygen plasma to determine if the CF_x peak would disappear. In this work, it was found that the residue disappears after pre-treatment of the substrates in an oxygen plasma for 2-3 minutes. Subsequently, it was shown by Bharadwaja et al. that a fluorine-containing compound can also develop due to the XeF_2 release step.

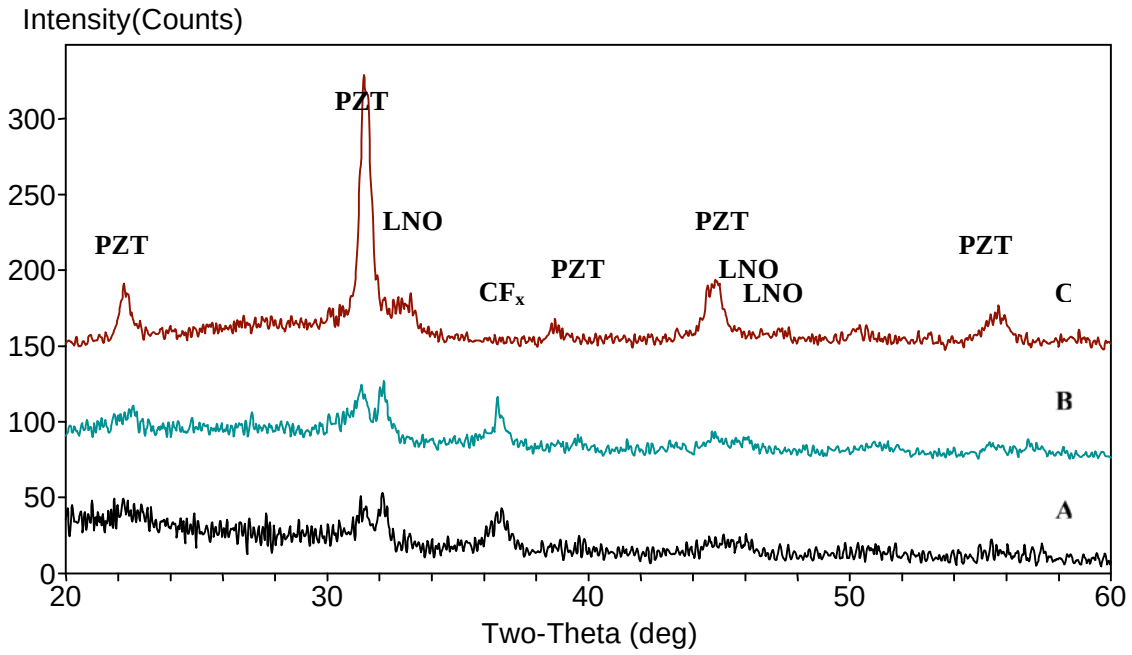

Figure 4- 9: X-ray diffraction patterns of $LaNiO_3$-PZT-$LaNiO_3$ tubes heat prepared under different conditions.

It is clear from the x-ray patterns that tubes which were heat-treated in the RTA at 750 ^{o}C for 1 minute were poorly crystallized. Significantly improved crystallinity was obtained using a two step crystallization, one at 650 ^{o}C and another at 750 ^{o}C. On the basis of this work, an improved process was developed as shown in Figure 4- 10.

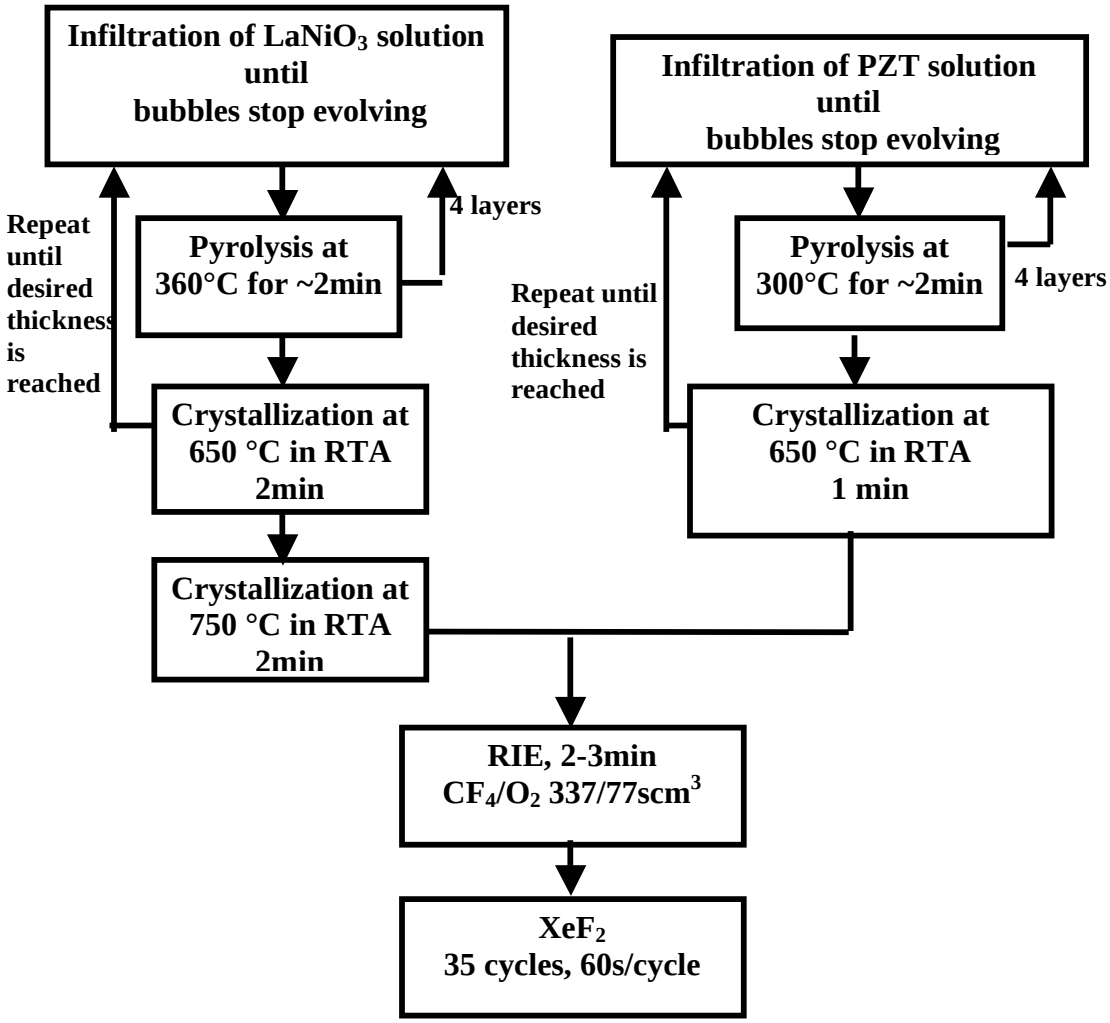

Figure 4- 10: Flow chart of the modified crystallization process for LNO-PZT-LNO tube fabrication.

4.5. *Conclusions*

In summary, it was found that vacuum infiltration of porous Si molds was an effective means of creating high aspect ratio PZT structures with reasonable phase purity. The results obtained here were subsequently confirmed by Bharadwaja et al [2].

After pre-cleaning Si molds with RIE and BOE to remove the organic deposit and native oxide layer formed during the Bosch process, these templates were used for

deposition of electrode and piezoelectric solution. In order to achieve infiltration, the deposition needed to be under vacuum to remove the air trapped in the tube. The deposition and pyrolysis were alternated for four layers prior to a crystallization step. An optimized condition for crystallization of the piezoelectric and the electrode layers was determined. When the tube deposited reached the desired thickness, the Si substrate was removed using XeF_2 etching. This resulted in high aspect ratio structures arranged in an ordered manner on the substrate.

Despite the progress with processing piezoelectric tube structures by this method, it would be extremely hard to contact an array of such tubes with electrical interconnects after fabrication. For this reason an alternative geometry was attempted where an array of metal posts was used. Here, the posts were prepared on a substrate which could be pre-patterned with the electrical interconnects. In this case, the metal core acts as a rigid support, the inner electrode, and the structure which should control the resonant frequency of the device.

References

[1] Q. Zhou, J. M. Cannata, R. J. Meyer, Jr., D. J. Van Tol, S. Tadigadapa, W. J. Hughes, K. K. Shung, and S. Trolier-McKinstry, IEEE Transactions on Ultrasonics, Ferroelectrics and Frequency Control **52,** 350-357 (2005).

[2] S. S. N. Bharadwaja, M. Olszta, S. Trolier-McKinstry, X. Li, T. S. Mayer, and F. Roozeboom, Journal of the American Ceramic Society **89,** 2695-2701 (2006).

[3] F. Laermer and A. Schilp, (Robert Bosch GmbH Patent No. 5501893, 1996).

[4] R. W. Schwartz, Chem. Mater. **9,** 2325-2340 (1997).

[5] M. Wasilik and N. Chen, (Berkeley Sensor & Actuator Center).

5 Post Geometry Transducers

5.1 Introduction

The second type of two dimensional transducer was introduced to address some of the issues that arose while developing the tube transducers. The tube transducers discussed in chapter 3 proved to be geometrically difficult to electrode and contact, and the tubes were structurally not very sturdy. Thus, as an alternative, tall metal posts were used as robust inner electrode structures on which PZT could be deposited. The dimensions were again chosen to maintain a 50MHz center frequency with a wide bandwidth and a pitch that can be used for beam steering.

5.2 Post Transducer Modeling

This second version of a 2D array transducer consists of a series of Ni posts with PZT covering the surface. An outer electrode can then be deposited on the PZT, as shown in Figure 5-1 to enable electrical contact. The piezoelectric will be addressed through the thickness of the PZT layer. Schematics of the post and the interconnects are shown in Figure 5-1.

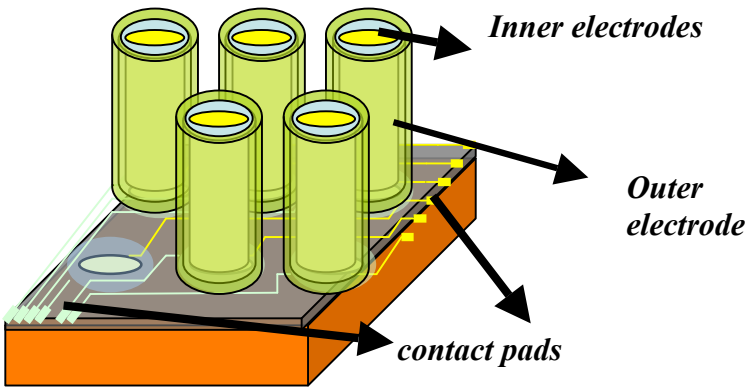

Figure 5-1: Schematic showing the geometry and interconnects of the 2D transducers. (Figure drawn by Hyunsoo Kim).

For this structure, the dimension used to establish the resonance frequency is the height of the posts. Each element is driven through the thickness of the piezoelectric by applying electrodes to the inside and outside of the tubes. Because the piezoelectric layer between the electrodes is thin, the voltage required to drive the transducer is low. As long as the driving voltage is below ~9V, the transducer is potentially integratable with a CMOS chip, where both the receive and transmit electronics can be included. That is, if the distance between the electrodes is too large (as in bulk ceramic transducer arrays), the large voltage required to generate the ultrasound pulse would damage the sensitive receive electronics, unless they are decoupled. Thin films, however, offer the prospect of low drive voltages, and so enable additional electronics integration.

Two approaches were employed to model the behavior of an array element. First, using the KLM model in PiezoCAD (Sonic Concepts, Woodinville, WA), one transducer element was modeled in two dimensions. Secondly, PZFlex (Weidlinger Associates, inc. Mountain View, CA) was used for finite element simulations. The modelling was done by Richard Tutwiler from the Applied Research Laboratory at Penn State.

As a proof of concept for this transducer geometry, a transducer with a center frequency of 50MHz was designed. The element dimensions in Figure 5-2 for the KLM model were chosen for this frequency. Modeling has shown that in order to have a resonance at 50MHz the height of the posts needs to be 41μm. The diameter of the metal was set to 8μm. The thickness of the PZT was set at 1μm due to the ease of deposition of this thickness using sol-gel and in order to match the capacitance of the piezoelectric as close as possible to that of the 50 Ohm electronics at the resonant frequency. As discussed in Chapter 1, in order to enable electronic beam steering and focusing the pitch

needs to be less then half the wavelength. To incorporate this into our design the pitch of the individual elements was set at 15μm. Silicon was used as the backing material and the transducer was transmitting into water. The PZT values were taken from the PiezoCAD database for PZT-8. These PZT data were chosen because thin films typically behave as hard piezoelectrics [1]. In KLM the posts were modeled as hollow tubes, because PiezoCAD does not allow for the input of the metal core. The response curves for the modeled data are shown in Figure 5-3.

Element array specifications:

Thickness/Height = 41 μm
Outer Diameter = 10 μm
Inner Diameter = 8 μm
PZT Wall thickness = 1 μm
Center Frequency = 50 MHz
Pitch = 15 μm
Kerf = 13 μm

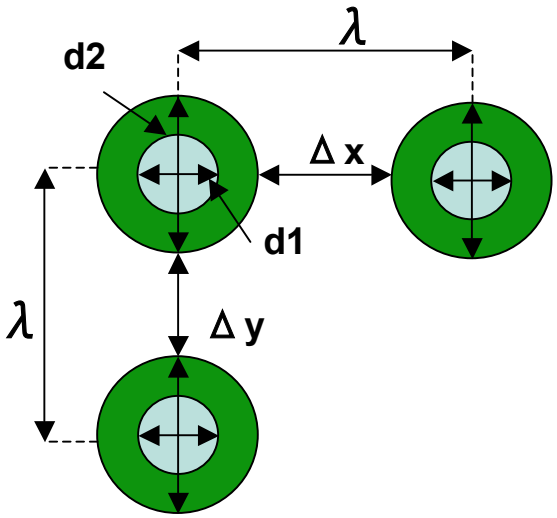

Figure 5-2: Design and layout specifications for the 2D transducers.

The centre frequency, bandwidth, and pulse duration for the model are given in Table 1. As it can be seen, the response has a center frequency very close to the desired frequency with a large bandwidth, and a short pulse duration.

Table 5-1: The center frequency, bandwidth, and pulse width of the post ultrasound transducer as modeled by the KLM model

Level	Center Freq.	Bandwidth	Bandwidth	Pulse Width
dB	MHz	MHz	%	nsec
-6	50.77	23.39	46	41
-20	51.01	41.37	81	63
-40	52.43	72.39	138	128

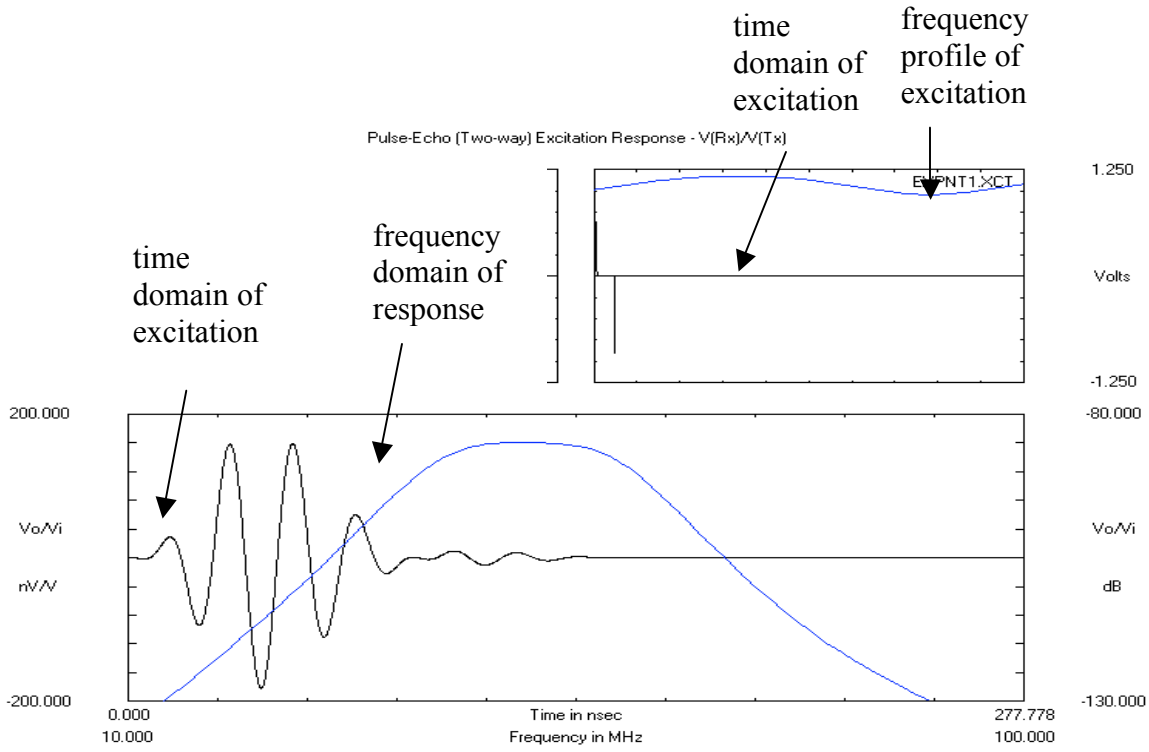

Figure 5-3: KLM model of the excitation and response of the signal of the post transducer

Overall the results of the KLM modeling are positive. At -6dB level the resonant frequency at 50.77 MHz is very close to the desired 50MHz frequency, the bandwidth is 46%, which means that the transducer can be used for imaging in the approximate frequency range of 40-60MHz. Finally the pulse width is very short, and close to the

desired single cycle sine wave, which will be useful in minimizing interference between the transmitted and received signals.

These encouraging initial results merited additional, more complete modeling than was possible using PiezoCAD. For example, the only materials defined in the KLM model are the PZT and the backing layer. The electrodes are omitted, as are details on the transducer geometry. The impedance is calculated from the defined area of the transducer, and electroding is done by default top to bottom. Further, only a single element can modeled. A more complete model can be done using finite element analysis.

The post transducers were also modeled using finite element analysis (FEA) using PZFlex. In order to do so, the device was broken down into a mesh using the coordinate system shown in Figure 5-4. The material are then defined using the coordinates, and the mesh is plotted. Because the post elements are cylindrically symmetric, the elements $\mathbf{Y_4}$ and $\mathbf{J_4}$ are used such that only half of the element along that axis is modeled. By doing this, the simulation becomes simpler and takes a shorter time to run. Symmetry is then employed to get the overall results.

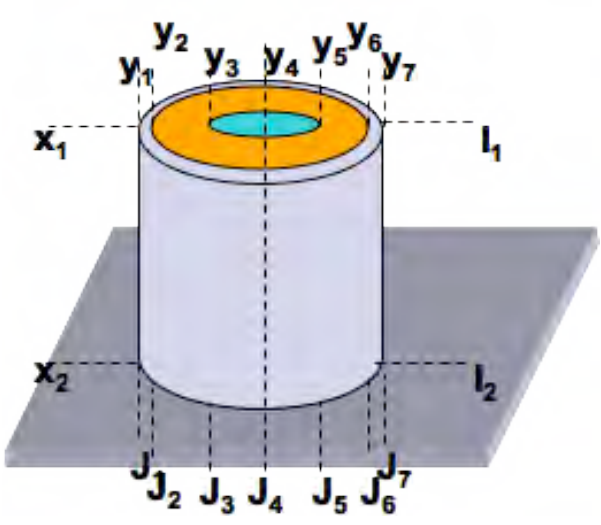

Figure 5-4: Coordinate definition for the FEA modeling of the post transducer

The inputs for the materials properties, the Ni core, PZT, and Pt top electrodes, used were taken from a database in the program. The input materials included the density, bulk and sheer moduli, the dielectric constant, the elastic compliance and stiffness coefficients, and the piezoelectric coefficients of PZT. The PZT properties used were taken from the database of PZT-8, as this is the closest material in properties to the sol-gel films. The surrounding material was set to water, and the boundary condition around the water was set as an absorbing layer, as otherwise reflections would interfere with the signal. The number of elements was set to 30. The ultrasound was then triggered with 3V at 50MHz.

In Figure 5-5 a time lapse of the generated sound wave is captured. The t1-t4 represent the time sequence at which these snapshots were taken from the time the sound wave was launched until the beam was focused. The outer elements are triggered first and the centre elements later. In this way the beam can be focused and steered using constructive and destructive interference. The model gave satisfactory results. Thus, this geometry was adopted for the fabrication of the 2D transducer. The proposed method of fabrication is discussed further in section 5.3.

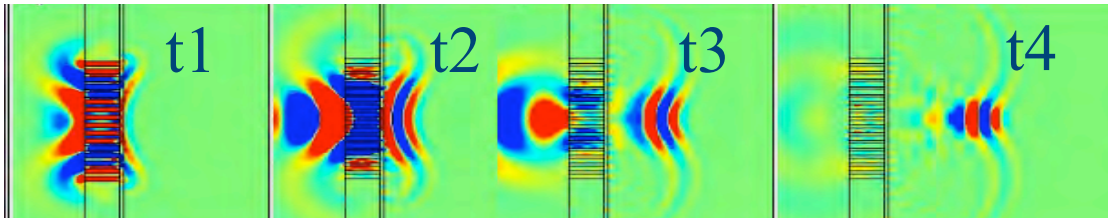

Figure 5-5: FEA of the 2D array showing the propagation of the beam with time. Focusing is clearly achieved by appropriate timing of the transducer excitation

5.3 *Post Transducer Fabrication Process*

There are several stages involved in the fabrication of 2D post transducer arrays: 1) The substrate fabrication, 2) post preparation, 3) PZT deposition, and finally the 4) top electrode deposition. The overall fabrication process, developed by Hyunsoo Kim, Sungkyu Park, and Prof. Thomas N. Jackson of the Electrical Engineering department at Penn State is shown in Figure 5-8. Details on these steps are given below.

Patterning of the contacts on the substrate is done using standard microfabrication procedures. The masks used in the lithography, and the final substrate are shown in Figure 5-6 and Figure 5-7. By fabricating the substrate in this way, the pillars that sit on top of the contact pads can be individually addressed, which makes beam forming possible.

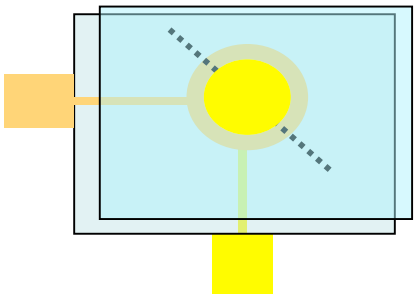

Figure 5-6: Schematic of the contact pads attached to the pillars. (As would be viewed from the top.) Figure drawn by Hyunsoo Kim.

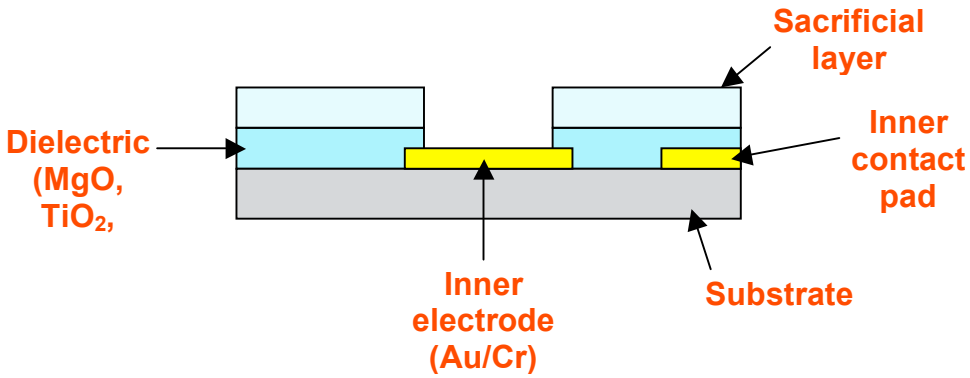

Figure 5-7: Side view of the substrate used for the post shaped transducers. Figure drawn by Hyunsoo Kim.

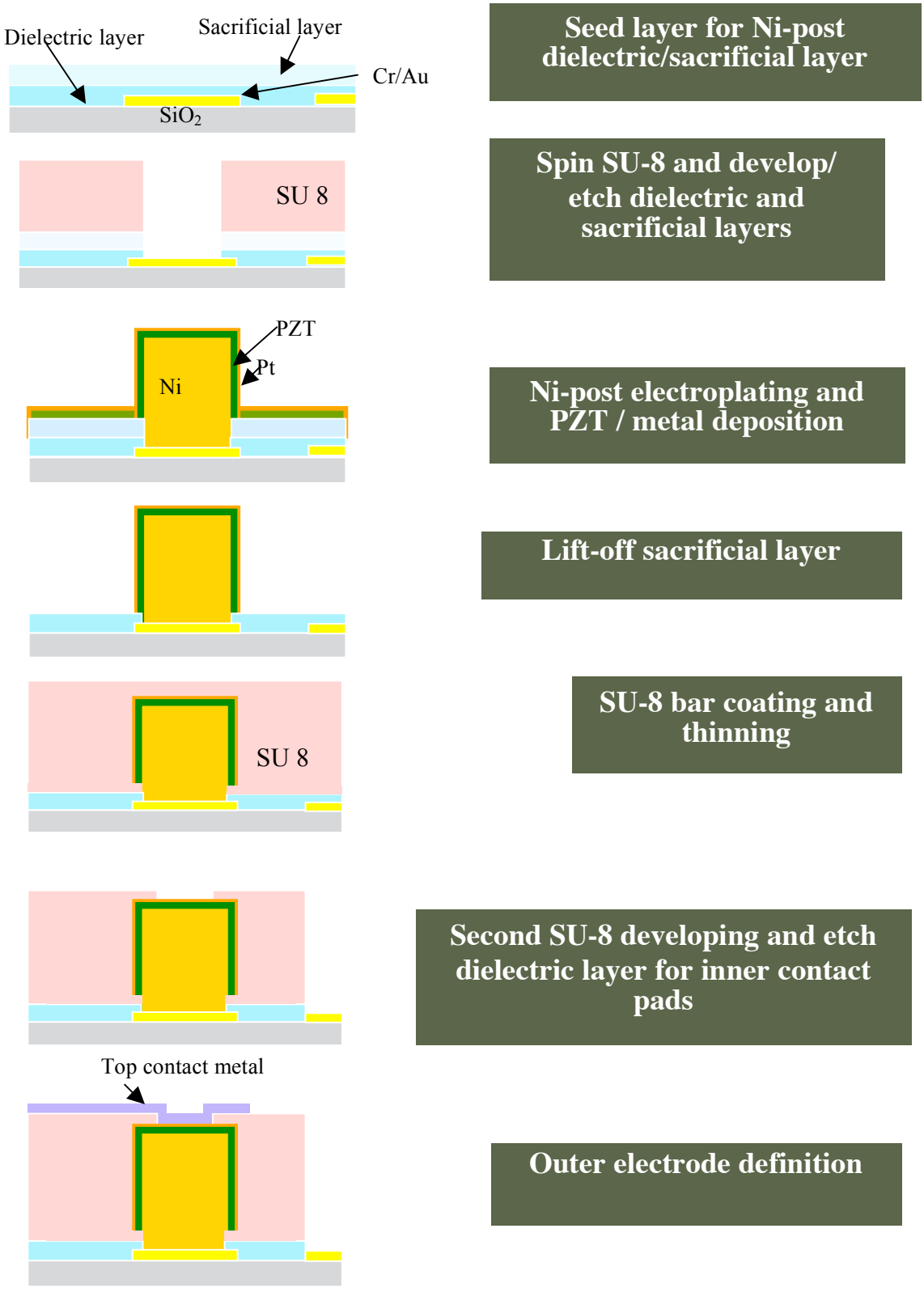

Figure 5-8: Planned pillar geometry transducer fabrication process. Figure drawn by Hyunsoo Kim

The posts are fabricated by first making the contact pads for the inner electrodes, and deposition of the dielectric and sacrificial layers on a Si wafer. SU 8 is then deposited on the wafer and patterned together with the dielectric and sacrificial layers using lithography as shown in Figure 5-7. The metal core is then electroplated into the SU-8 mold creating the high aspect ratio structures. Several different metals were explored for this purpose. While a noble metal such as Pt would be an ideal inner electrode, it was found that the electrodeposition rate of Pt from solution was too slow to enable pillars tens of microns in height to be prepared. In contrast, Ni could readily be prepared at the desired aspect ratio. Thus, initial work concentrated on Ni posts. The Ni was electroplated from an electrolyte formed by mixing deionized water, Ni-precursor and brightener at ratios of 20 : 2 : 1 (Caswell, inc., Lyons, NY) . The initial pH of the plating solution was 3.5 ~ 4.5. The Ni electrode and the substrate were then immersed in solution with an approximate distance from each other of 5cm. The deposition was performed with a constant current of 10 mA/cm^2.

When the plating is completed, the top surface was then polished to create a smooth, flat surface on the top of the posts, and the photoresist was removed, leaving metal pillars of 1:5 aspect ratio structures. SEM images of these structures are shown in Figure 5-9.

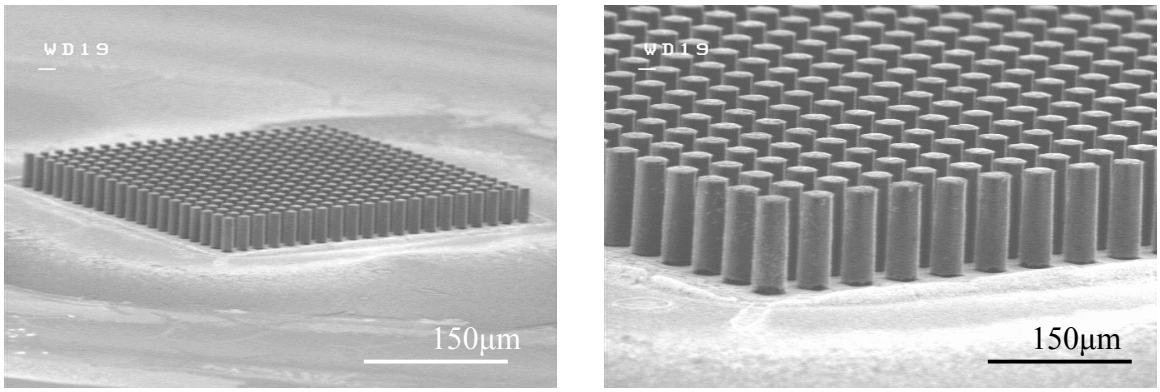

Figure 5-9: SEM images of Ni pillars on a substrate. SEM by Hyunsoo Kim

After the posts were fabricated, PZT was deposited on top. Several methods were tested for this purpose. Both dip and spin coating were unsuccessful due to the non-uniformity of the coating produced (See Figure 5-10). As can be seen, the solution collects at the bottom of the structures giving rise to a thick bottom layer that cracks during the heat treatment. The layer of PZT at the top was substantially thinner. No attempt was made to quantify the conformality of the coating due to the cracking.

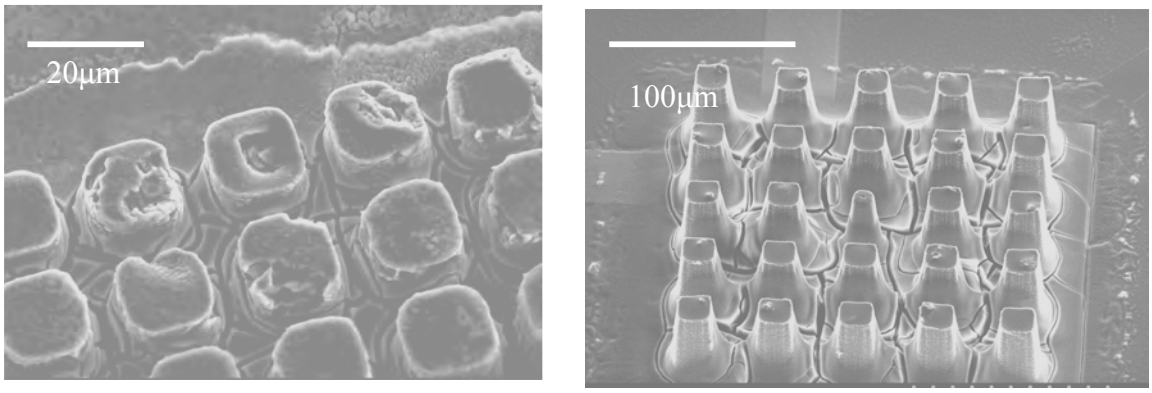

Figure 5-10: SEM images of dip coated (left), and spin coated (right) pillars.

The most effective conformal coating of the pillars was achieved using LSMCD. The coating of the pillars in the SEM appears to be uniform and after heat treatment there were no visual cracks like in the pillars that were spin and dip coated. SEM images of mist coated pillars are shown in Figure 5-11. The posts were deposited for 960 sec which on a flat film corresponds to approximately 0.25-0.3 microns thickness. The heat treatment that was performed to crystallize the PZT was as described in Chapter 2, pyrolysis on a hotplate at 350 and 450 ^{o}C for 1 minute each, and crystallization in air at 700 ^{o}C for 1 minute.

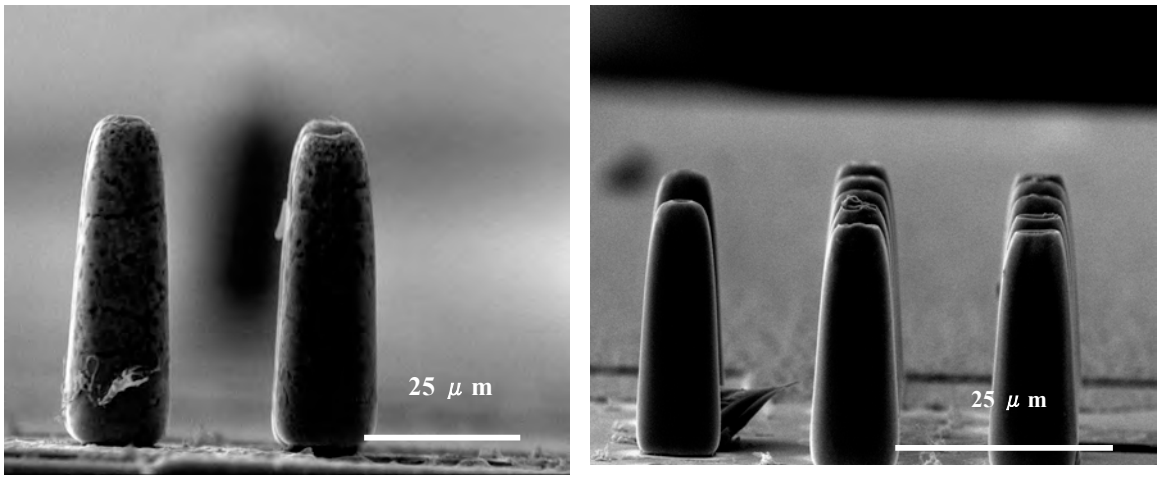

Figure 5-11: SEM images of electroplated Ni posts with PZT

In order to determine the quality of PZT and electrode, x-ray diffraction was performed on post structures. The x-ray scan between 20 and 60 degrees 2Θ is shown in Figure 5-12. In addition to the crystalline perovskite phase, there are also unwanted NiO peaks, and some pyrochlore. These probably result from the oxidation of Ni during the heat treatments, and either the migration of Pb into the Ni or volatility of lead as PbO to form a lead deficient PZT. It has been widely reported that the pyrochlore phase develops from lead deficient PZT films [2,3].

Chapter 6 describes a study to determine the optimum conditions for PZT deposition onto Ni substrates. As will be shown there, it is possible to deposit PZT that is phase pure (by X-ray diffraction) onto Ni substrates. Thus, this general approach to preparing 2D array transducers by depositing a piezoelectric film over pre-patterned high aspect ratio structures is a promising one. No further work was carried out on 2D arrays in this thesis in order to concentrate on linear arrays. However, additional work should be performed on this in the future.

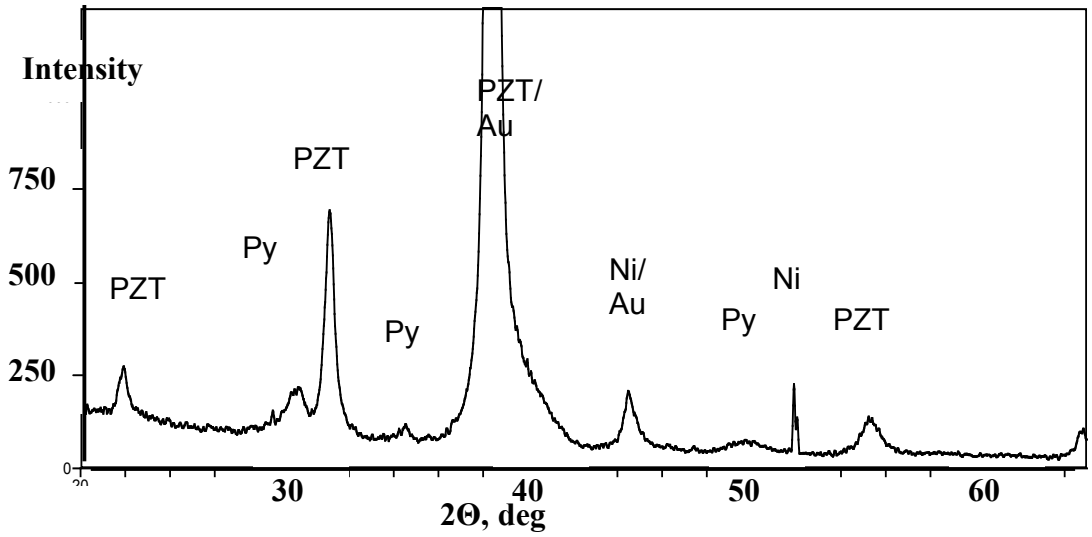

Figure 5-12: X-ray data of electroplated Ni posts with PZT crystallized at 700 ^{0}C in air. Peaks marked Py are from a pyrochlore phase

References

[1] **F. Xu, S. Trolier-McKinstry, W. Ren, X. Baomin, Z. L. Xie, and K. J. Hemker, Journal of Applied Physics 89, 1336-1348 (2001).**

[2] **E. M. Griswold, L. Weaver, M. Sayer, and I. D. Calder, Journal of Materials Research 10, 3149-3159 (1995).**

[3] **S.-Y. Chen and I. W. Chen, Journal of the American Ceramic Society 81, 97-105 (1998).**

6 PZT on Base Metal Electrodes

6.1 Overview

Base metal electrodes (BME) are frequently used to cut costs in the capacitor industry due to their lower market cost in comparison to metals such as Pt, Pd, Au and Ag [1]. However, BME parts are more susceptible to oxidation during high temperature processing. In $BaTiO_3$-based capacitors, use of Ni electrodes requires that the part be fired in a reducing atmosphere [1]. Some common BME metals, their firing conditions and price comparisons are shown in Table 6- 1.

Table 6- 1: Metal electrodes for capacitors[1]

Metal	Processing atmosphere	Price ratio
Ag	Air	3
Cu	Reducing	1
Ni	Reducing	1
Pd	Air	80

As was discussed in Chapter 3, integration of PZT with Ni needs to be investigated because Ni can readily be electroplated into high aspect ratio structures that can be used to control the frequency of an ultrasound transducer array[2]. In contrast, noble metals, such as platinum, are very hard to plate to thicknesses of tens of microns[2].

BME electroceramic technology has focused predominantly on $BaTiO_3$ dielectrics; only recently has focus been extended to the PZT system. The reason that PZT has not been investigated is probably three-fold. First, the region of

thermodynamic equilibrium for the PZT / Cu or Ni system is constrained by the Pb constituent and is significantly narrower than that allowed for $BaTiO_3$. Thus, controlling the processing conditions for a PZT/Cu stack would be considerably more difficult whereas a PZT/Ni stack is thermodynamically impossible [3]. The system is further complicated by the volatility of PbO. To achieve a true equilibrium state, it would be necessary to also control the partial pressure of PbO. Thirdly, the faster sintering kinetics expected for a Pb-based system may also create a kinetic limitation to reaching thermodynamic equilibrium. If the dielectric rapidly densifies, then any premature oxidation of the base metal may be difficult to reverse due to the slower diffusion rate expected through a dense ceramic layer [3].

The effect of a NiO interface layer on the apparent dielectric constant of a PZT film on a Ni foil can be calculated using a model for capacitors in series, where C_T is the total capacitance of all the layers and C_i is the capacitance of the individual layer.

$$\frac{1}{C_T} = \sum_i \frac{1}{C_i}$$

Figure 6-1 shows the result. For this calculation it was assumed that the PZT film has a dielectric constant of about 1000 [4], and NiO has a dielectric constant of approximately 8 to11, depending on the thickness of the sample, in thin films, and about 15 in bulk [5]. The hypothetical PZT film is 1μm thick and the electrode area is $1mm^2$.

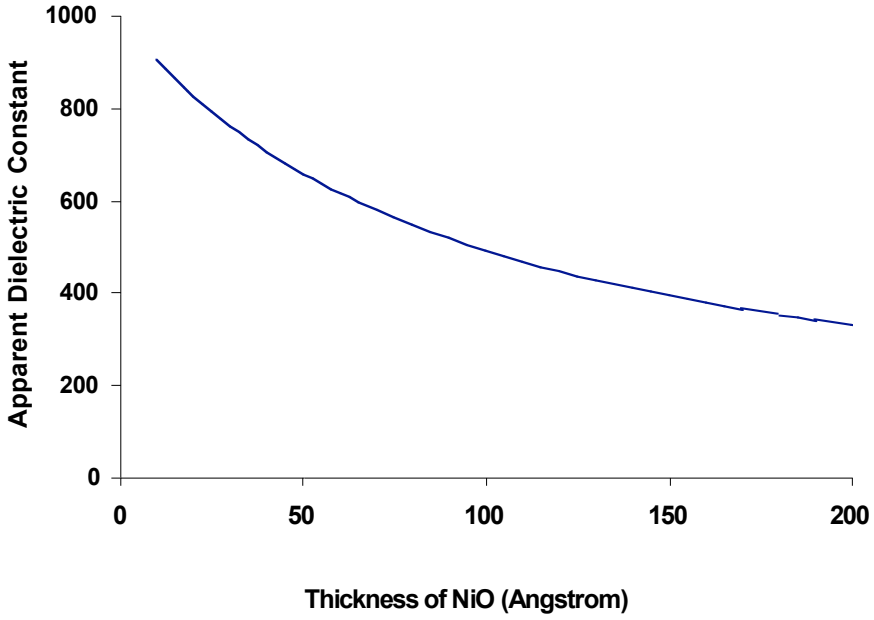

Figure 6-1: Calculation showing how the growth of a NiO interface layer affects the apparent dielectric properties of a PZT film on Ni

If the Ni is allowed to form 50Å of NiO, the apparent PZT permittivity decreases from 1000 to about 700; at 100Å of NiO the capacitance halves to a value of about 500. As shown in Chapter 1, in order to fabricate a transducer functional at >50MHz the element size must be extremely small. Yet at the same time we need to impedance match the elements to 50 Ohm electronics at the operating frequency. This requires a comparatively large capacitance of ~60pF for a 50 MHz transducer if we assume a 1/ωC relationship with impedance. The only way to achieve that is if the piezoelectric material had a high dielectric constant, since the capacitance is proportional to the permittivity of a material.

$$C = \frac{\varepsilon \varepsilon_0 A}{d} \qquad \textbf{Equation 1}$$

The ε_r here is the dielectric constant, d is the thickness of the capacitor, A is the area of electrodes, and ε_0 is the permittivity of free space, 8.85×10^{-12} F m^{-1}. Thus, minimizing formation of a low permittivity barrier layer between the electrode and the piezoelectric is important.

6.1.1 Thermodynamic Stability of the Ni/PZT interface

Figure 6-2 shows the thermodynamic stability of the Ni/NiO and Pb/PbO systems as a function of temperature and oxygen partial pressure [3]. It can be seen that there are no conditions under which the lead in the PZT can remain oxidized, while the Ni at the PZT/electrode interface remains reduced. For example, at a typical pyrolysis temperature of 350 °C, PbO reduces to Pb at a P_{O2} of 10^{-24} atm, and yet a pO_2 of 10^{-32} atm would be required to keep the Ni metallic. Similarly, at the crystallization temperature of 670 °C, Ni oxidizes and PbO reduces between 10^{-16} and 10^{-14} atm. Thus, according to this diagram it would be thermodynamically impossible to keep Ni reduced without the precipitation of metallic lead when PZT is in direct contact with the Ni. Consequently, attempts to prepare PZT on Ni rely either on kinetics to prevent the Ni oxidation, or a barrier layer to reduce the reactivity of the Ni surface. That is, in order for metallic lead to form, oxygen needs to move out of the perovskite phase, which is kinetically a slow process due to the need to overcome the energy of bond breaking in a perovskite. Moreover, if Ni is protected with a uniform coating of a noble metal, the oxidation process may be pushed to higher temperatures and longer annealing times [6,7].

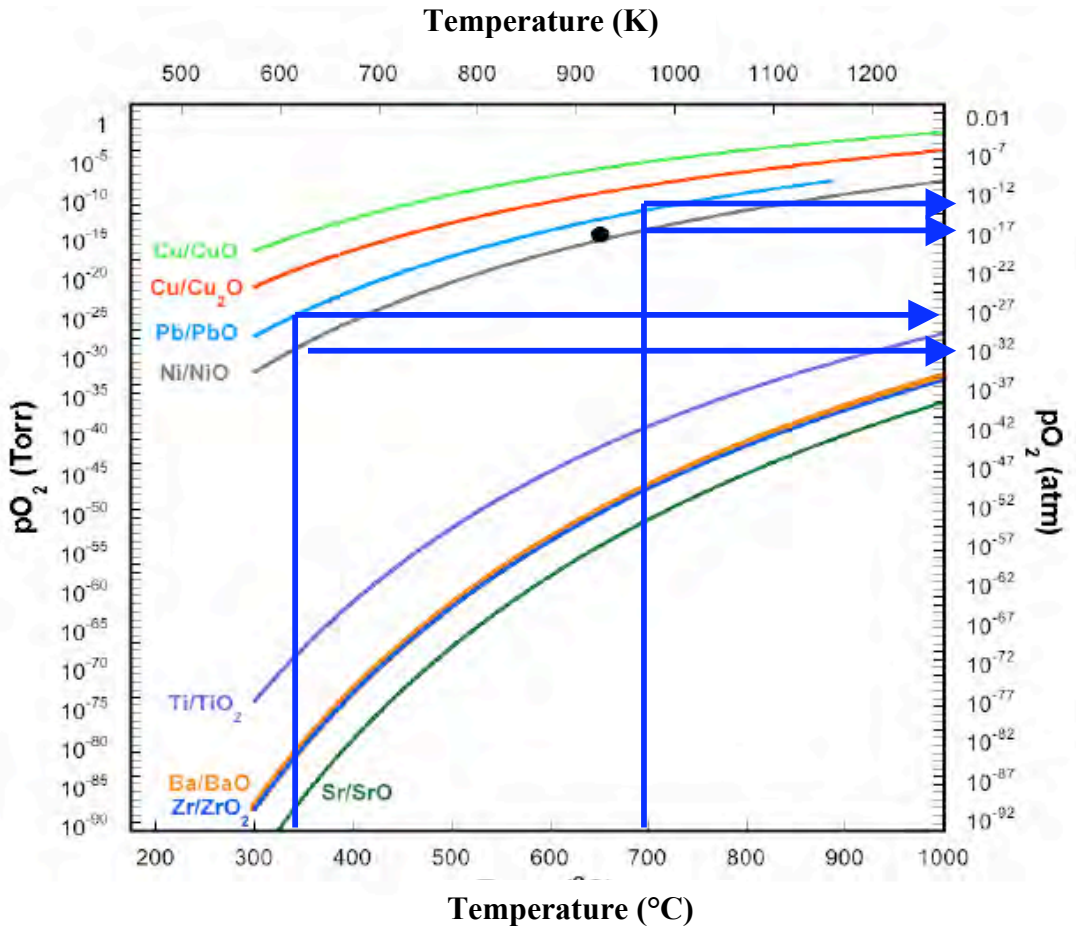

Figure 6-2: Phase diagram showing the P_{O2} at the pyrolysis and crystallization temperatures that will transform the PbO into metallic Pb[3].

6.1.2 BME/PZT interface

Figure 6-3 and Figure 6- 4 [8], there is solid solubility between Ni and Pb and Cu and Pb. This means that there will be diffusion of Pb into the Ni and Cu, degrading the interface between the electrode and dielectric, by forming capacitors in series, Pb, and poor quality PZT. This also needs to be considered in preparing PZT on Ni or Cu structures.

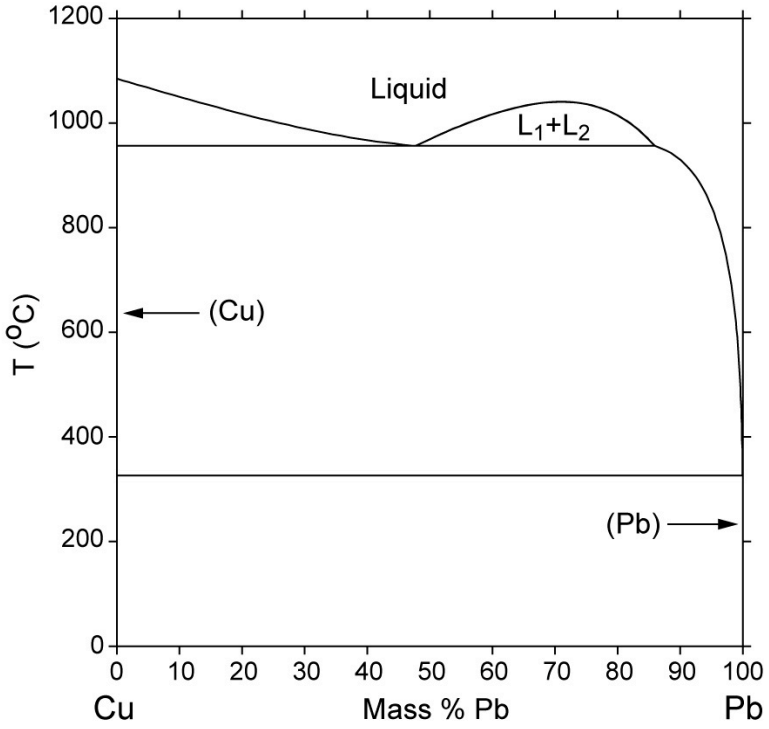

Figure 6- 3: Cu-Pb phase diagram [9]

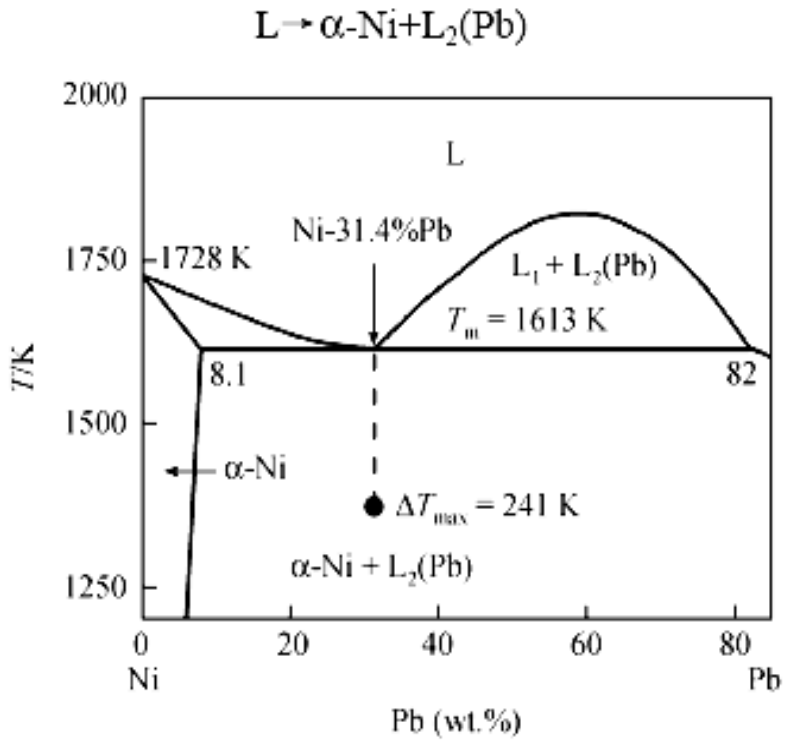

Figure 6- 4: Ni-Pb phase diagram [8]

Nickel electrodes have replaced the noble metals in $BaTiO_3$ capacitors, and recently methods for depositing PZT films on copper electrodes have been developed by Kingon [10] and Losego [3]. A dielectric constant of 1000 was obtained on the reported films. In contrast, less has been done on deposition of PZT on alternative electrodes. Zou [11] studied the properties of PZT (the composition was not described) films on titanium, stainless steel, brass, and nickel alloy electrodes. The highest dielectric constant (400) with a loss of 4% was shown for films on titanium, and the lowest (111 with a 11% loss) for films on the Ni alloy. The material in this case was deposited directly onto the substrate without any interfacial layers. Another report of deposition of PZT on Ni plated Cu electrodes is described by Kim [12]. This group used 50-100nm of ZrO_2 as a buffer layer, and the reported dielectric properties were $400nF/cm^2$ for films of thickness in the 700-800nm. A TEM investigation showed a 50nm thick interfacial layer of undetermined composition that resulted possibly from oxidation of substrate and reaction of neighboring species.

Suzuki et al. [13] report on RF-magnetron sputtering of PZT 53/47 directly onto stainless steel substrates. The x-ray of the films show a phase pure perovskite, however, the dielectric constant of the films was 110, which is substantially less then the quoted values for PZT on Si substrates [13]. The low dielectric constant is attributed to residual thermal stress.

Cheng et al. [14] used $LaNiO_3$ as an interfacial layer for the deposition of PZT on Si, Ti, NiCr, and stainless steel substrates using spin coating. The x-ray data for all the substrates show phase pure perovskite PZT, however, no dielectric data was reported.

Cheng [15] et al. used $PbTiO_3$ perovskite as a buffer layer on stainless steel. This created a seed layer for the crystallization of PZT 52/48 at lower temperatures. The films were crystallized at 550 ^oC. The reported dielectric constant and loss were 280 and 7% respectively. Despite the low dielectric constant, the hysteresis loop parameters were high, with Pr of 35$\mu C/cm^2$ and Ec of 99kV/cm. However, the large coercive field and low dielectric constant suggest that there could be an interfacial layer present between the electrode and the dielectric.

Finally, excellent dielectric properties are reported by Baba [16] for 52/48 PZT films on stainless steel substrates. The films were deposited by CO_2 laser assisted aerosol deposition. Films with a dielectric constant of >1000 at 1kHz and a loss below 2% were demonstrated.

One of the possible solutions to the problem of oxidation is coating of the BME with a noble metal. This will minimize exposure to the various oxidizing ambients used during the heat treatments. Bencan [7] et al. used a Au interfacial layer on Ni substrates to decrease oxidation and reaction between PZT and Ni. Electron microscopy still showed 8% solid solubility of NiO in the PZT. A dielectric constant of 450 for PZT 53/47 with a loss tangent of 5% was reported, which was an improvement.

Another method is described by Tsur et al. [6] where the Ni metal powder is dipped into a solution of hexachloroplatinic solution and a passivation metal is deposited onto the surface of the powder via exchange as shown in Figure 6-5. A potential reaction scheme for the process is:

$2Ni\ (s) \Leftrightarrow 2Ni^{2+}\ (aq) + 4e^-$, $E^\circ_{ox}=0.514$ V

$[PtCl_6]^{2-}(aq) + 4e^- \Leftrightarrow Pt\ (s) + 6Cl^-(aq)$, $E°_{red}=1.435$ V

$2Ni(s) + [PtCl_6]^{2-}(aq) + Pt(s) + 6Cl^-(aq)$, $E°_{cell}=1.949$ V

The positive overall potential of the cell constitutes a feasible reaction. This method creates a monolayer of deposited metal. The passivation layer was shown to reduce the rate of oxidation of Ni.

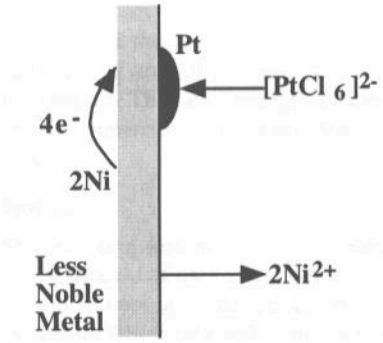

Figure 6-5:Reaction scheme for platinization of Ni [6]

6.2 Oxidation of Ni on Model Substrates: Experimental Procedure and Results

6.2.1 Model Substrates

Studies of model PZT/Ni interfaces were made using commercially available nickel foils and nickel-coated Si, where the purities and surface morphologies were well-defined. Several types of substrates were used for this purpose: rolled Ni foils of 0.05mm thickness (99+% Ni), 0.025mm thickness (99.99% Ni), and 0.1mm (99.994%

Ni), as well as Si/SiO_2/Ni/Pt substrates, and electroplated Ni. The 99+% purity foils were the roughest, while the 99.99% and 99.994% purity foils were smoother. The sputtered wafers and plated Ni foils were extremely smooth. This could be detected visually, as smoother foils were more reflective than the rougher ones. To quantify the differences, AFM was used to compare the surface roughness of the 99.99% and 99+% foils. It can be seen in Figure 6-6 that there is considerable large scale topology on the 99+% purity substrates. Because the surface roughness is on the order of the film thickness, PZT films prepared on these substrates were susceptible to electrical shorts, especially if the films were thin. This complicated electrical characterization of the interface quality. Moreover, the low reflectivity of the surface made ellipsometry alignment difficult. The lower purity could also lead to unwanted chemical reactions between the impurities and the PZT, resulting in degradation of film properties.

An AFM image of the 99.99% pure thinner Ni foils is shown in Figure 6-7 for

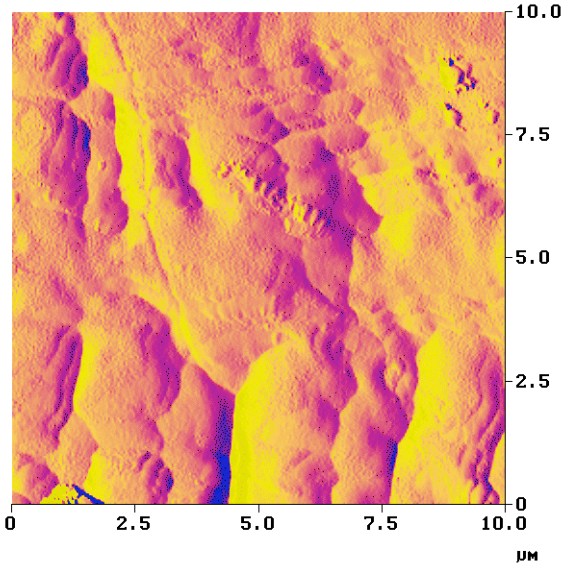

Figure 6-6: AFM and statistics on the "rough", 99+% pure Ni foils. The rms roughness was 43.9 while the average roughness was 34.2 nm. The peak to valley roughness was in excess of 330 nm. Courtesy of Tanawadee Dechakupt

comparison and an SEM in Figure 6-8 These foils had a smoother surface overall; however they also contained some large striations that came from the rolling process.

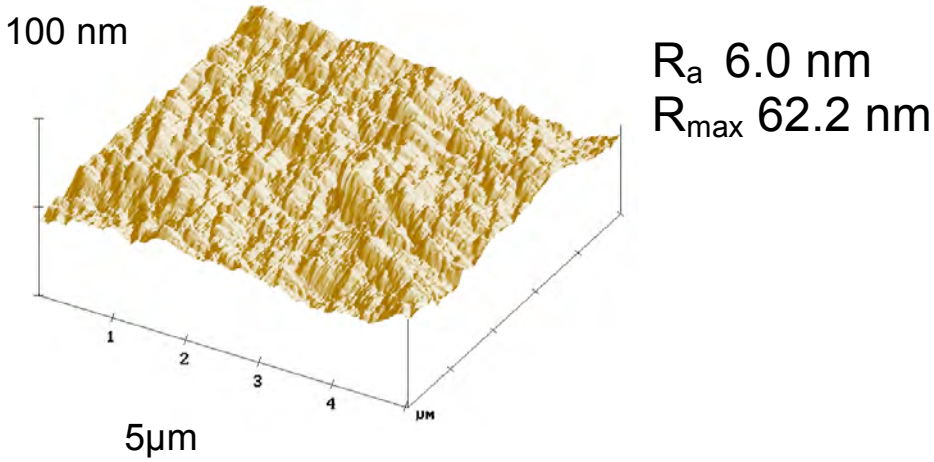

Figure 6-7: AFM image of the 99.99% purity nickel foil. Courtesy of Tanawadee Dechakupt

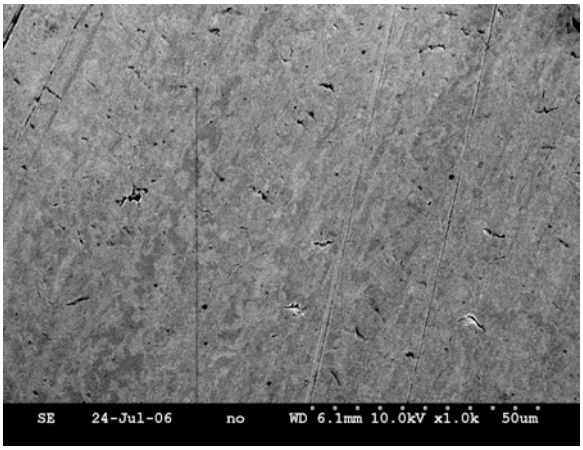

Figure 6-8: SEM image of the 99.99% purity Ni foil

Generally, the rolled films gave varying results as to how well Pt coated the surface of the foils. Often the Pt deposited as a rough black layer on the surface, presumably due to high levels of surface roughness. This made further work with the foils impossible, as the Pt came off the surface very easily, and unevenly. The quality

of the Pt layer deposited on the Ni foil surface depended strongly on the batch of the foil purchased, making comparison and reproducibility of the experiments extremely hard. The most successful results, as far as coating were obtained from the 99.994% purity foils with the lot number J27P29. The foils that were purchased with a different lot number later were not as smooth.

6.2.2 Temperature of Ni Foil Oxidation

6.2.2.1 Unplated Ni Foils

Initial experiments had shown that Ni foils cannot be used for PZT film deposition because, as predicted by the phase diagram in Figure 6- 2, they oxidize during the heat treatment step. In order to determine the temperature at which NiO begins to form on Ni, a series of experiments was performed where Ni foils were heated in air at various temperatures for two minutes. Two minutes was chosen since this is the typical time required for pyrolysis. After heat treatment, characterization was done to determine the presence and amount of NiO on each foil. Rough, low purity (99% pure) Ni foils were used in this experiment. Separate samples were heated at 200, 250, 300, 350, 400, and 450 °C for 2 min. At 450 °C there was a color change following heat-treatment; the foils turned from silvery to yellow. Due to this visual sign of oxidation, higher temperature treatments were not performed for this experiment.

X-rays patterns were taken on all the samples, and they are shown in Figure 6-9. The reader should note that there are no NiO peaks detected by the X-ray equipments even for foils treated at 450 °C, despite the visual color change.

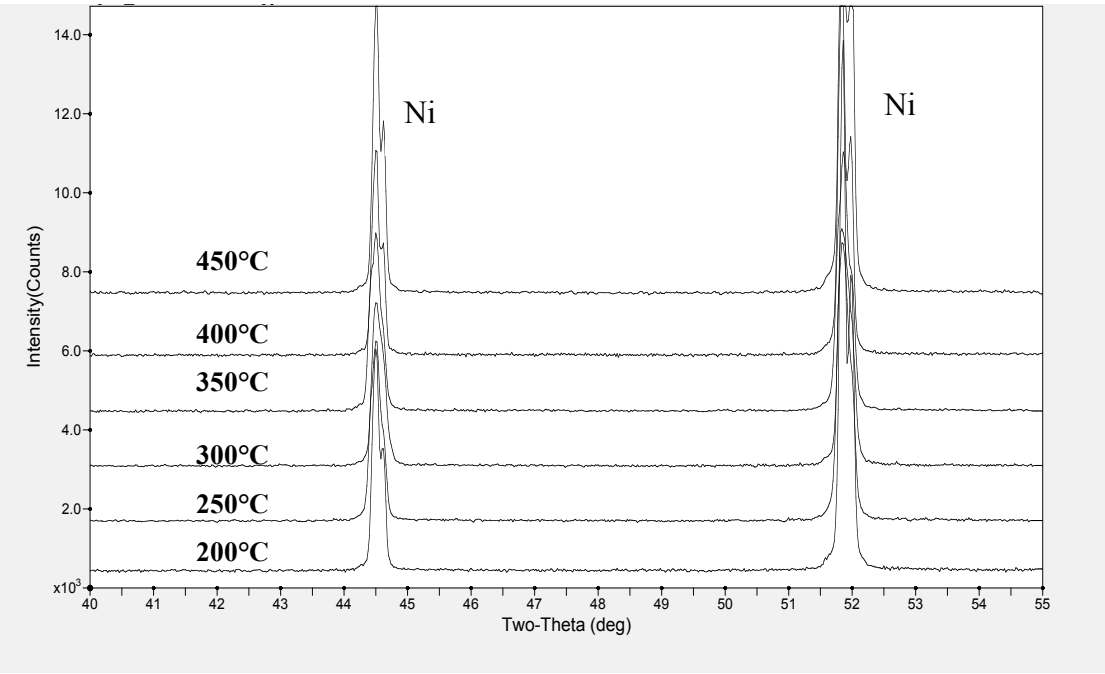

Figure 6- 9: X-rays of Ni foils heated between 200 °C and 450 °C at 50 °C intervals

Because the x-ray tool was not sensitive enough to determine presence of NiO, spectroscopic ellipsometry analysis was also done. The ellipsometry data were collected by Tanawadee Dechakupt. This experiment is done by directing plane polarized light at a known angle of incidence onto the sample surface. The change in the polarization state of the light on reflection is controlled by the depth profile of the optical dielecric function of the sample. The resulting data are then modeled to extract information on the depth profile [17]. The composition of the surface layers and their thicknesses can be identified. Plots of the raw psi and delta are shown in Figure 6-10. These relate to the phase and amplitude changes of the two components of the polarized light. One of the advantages of SE is the ability to detect very thin layers that would be very hard to detect using x-ray diffraction.

From the raw collected data in Figure 6-10 small, random changes in the parameters at annealing temperatures below 300 °C are visible. Above 300 °C, there is a systematic progression in the ellipsometric data, where the psi and delta curves begin to shift downwards on the y-axis. The sample heated at 450 °C has the most extreme shift, and shows significant deviation from the unoxidized samples. The larger amplitude oscillation is consistent with the development of an interference fringe from a transparent layer on an opaque substrate.

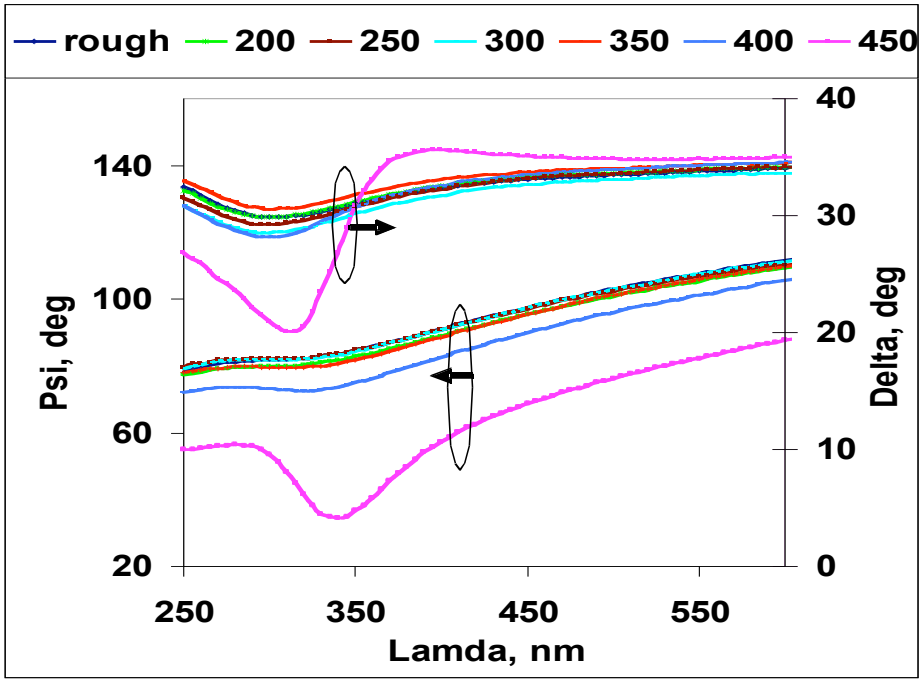

Figure 6-10: Spectroscopic ellipsometry data as a function of annealing temperature. Psi and delta as a function of wavelength of Ni foils heated between 200°C and 450°C for 2 minutes.

The ellipsometry data were modeled to determine the thickness of the oxide on the foils as a function of temperature. For low temperatures, the data were best fit as a thin layer of rough Ni on the substrate. At higher temperatures, however, there was a clear transition, and the best fit model consisted of a layer of NiO on the Ni. A graph

of the amount of oxide as a function of annealing temperature is shown in Figure 6-11. It is clear that at 300 °C the Ni begins to oxidize. The NiO layer thickness is 37 nm at 350 °C the thickness of the NiO on the surface is approximately 50 nm. Table 6- 2 summarizes the geometry of the measured layer, the composition and the unbiased estimator for the error in the fits.

Table 6- 2: Ni foils oxidation analysis using spectroscopic ellipsometry

Temp, °C	Composition of Layer	Layer Thickness, Å	sigma
200	Ni/Air 0.37/0.63	43 ± 2	0.0129
250	Ni/Air 0.29/0.71	39 ± 14	0.0216
300	Ni/NiO/Air 0.47/0.496/0.032	37 ± 5	0.0138
350	NiO/Air 0.437/0.563	51 ± 13	0.0140
400	NiO/Air 0.50/0.50	81 ± 7	
450	NiO/Air 0.67/0.36	205±2	0.0131

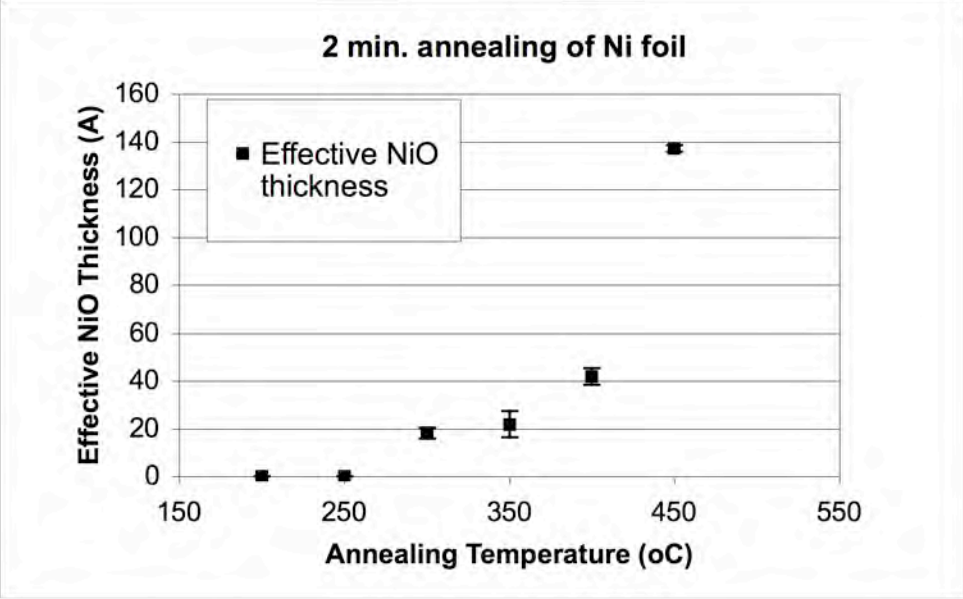

Figure 6-11: Modeling of the NiO thickness on heated Ni foils. Modeling of the data was performed by Tanawadee Dechakupt and Susan Trolier-McKinstry. The NiO effective thickness was calculated as the volume fraction of NiO times the layer thickness.

6.2.3 Ni plating

In order to determine the best conditions for Pt deposition onto the Ni foils, the foils were immersed in a beaker with hydrazine hydrate 85% solution in water (EMD Chemicals, inc. Gibbstown, NJ) to strip off NiO, and after washing with deionized water in $H_2[PtH_6]$. For the latter step, 1,000 μg/mL Pt in 5% HCl (Sigma Aldrich) solutions were tested on the 99.99% purity thin foils. SEM images of plated Ni foils are shown in Figure 6-12.

The effect of increased temperature during deposition was also studied on the 99.99% foils. For a bath temperature of 60 °C, the deposition rate was often faster. For elevated bath temperatures, the foil was placed in a beaker with approximately 5ml of the Pt solution. The beaker was placed on a hot plate with a stirrer. The solution was self-stirred by the magnetic nickel foils. The results of heating however, varied depending on the foils. On the thin 99.99% purity foils the deposition was rapid, but the black rough Pt deposit also appeared very quickly [18]. On the thicker 99.994% purity foils, the opposite effect took place; heating improved the smoothness of the surface, and the deposition time required was only about 15 min. A black deposit in this case began to appear only about 20-30 minutes into the deposition. Thus, heating was only appropriate for use with the thicker 99.994% purity foils.

It is worth noting that the success of deposition of Pt onto Ni foils varied dramatically depending on the substrates used. The thick 99.+% purity samples and especially the 99.994% foils were quickly and nearly uniformly covered without any black Pt residue the majority of the times. Deposits on the 99.99% purity foils depended strongly on the batch of the foils. The majority of the 99.99% foils would

rapidly show Pt on the surface in the form of the black residue, so the repeatability of this process was quite low. For this reason, when available, the 99.994% foils were used. Generally, the coverage of the Pt was pretty good, with a few visible blemishes. Images of the various platinized foils are shown in Figure 6-12 . Leaving the foils overnight in the Pt solution resulted in the appearance of the black precipitate. Thus, the deposition had to be closely monitored to determine the maximum amount of smooth Pt deposition that could be achieved.

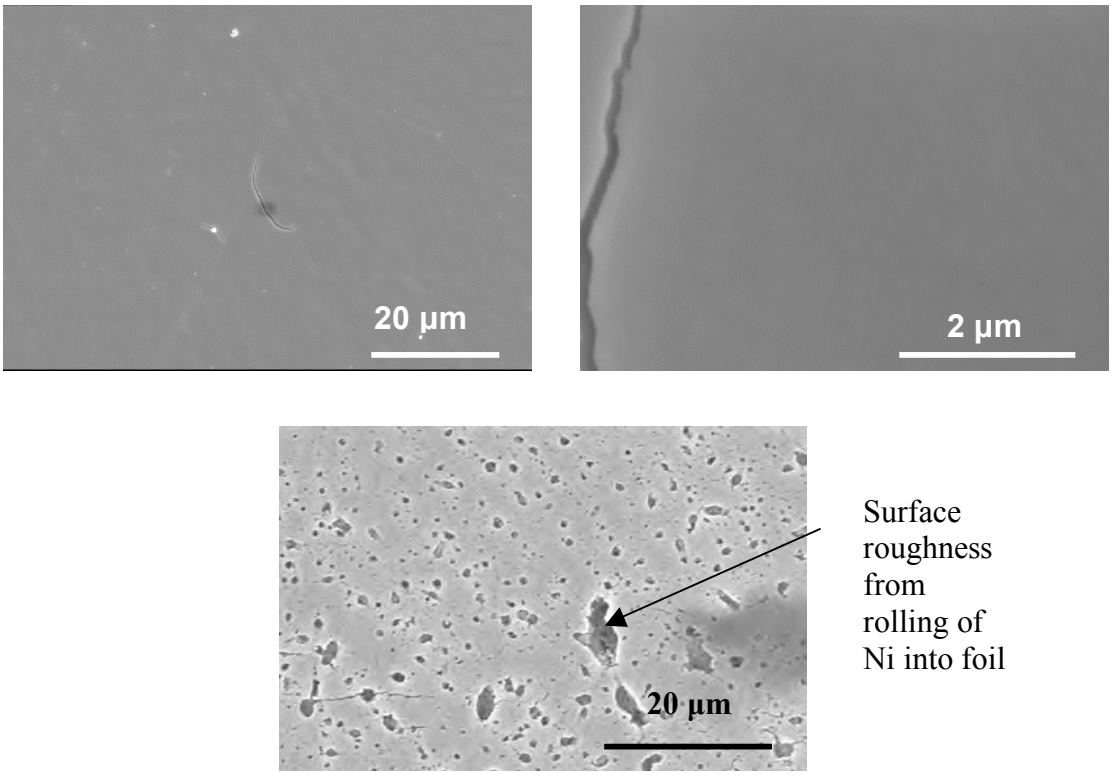

Figure 6-12: Pt-coated Ni foils Top: left 99.994% low magnification with sputtered 20nm Pt, top right: 99.994% Ni foil at high magnification. Bottom: 99+% purity plated Ni foil

All the thinner 99.99% purity plated foils used in subsequent experiments were deposited at room temperature for approximately 1 hour. The thicker 99.994% purity

foils were deposited at 60°C for approximately 15 minutes, since it was possible to use the faster rates without forming black, roughened Pt.

6.2.4 Heating Results of the Plated Ni Foils

To determine whether a Pt coating reduced the oxidation four samples of 99.99% purity Ni foil were plated with Pt. They were then heated to either 350 °C (air), 400 °C (air), 600°C (5slpm N_2). A fourth sample was left for control. The x-ray data for samples heated at 400°C and 600°C are shown in Figure 6-13. The diffraction pattern of the foil at 400 °C shows no NiO peaks, the foil heated at 600 °C could potentially

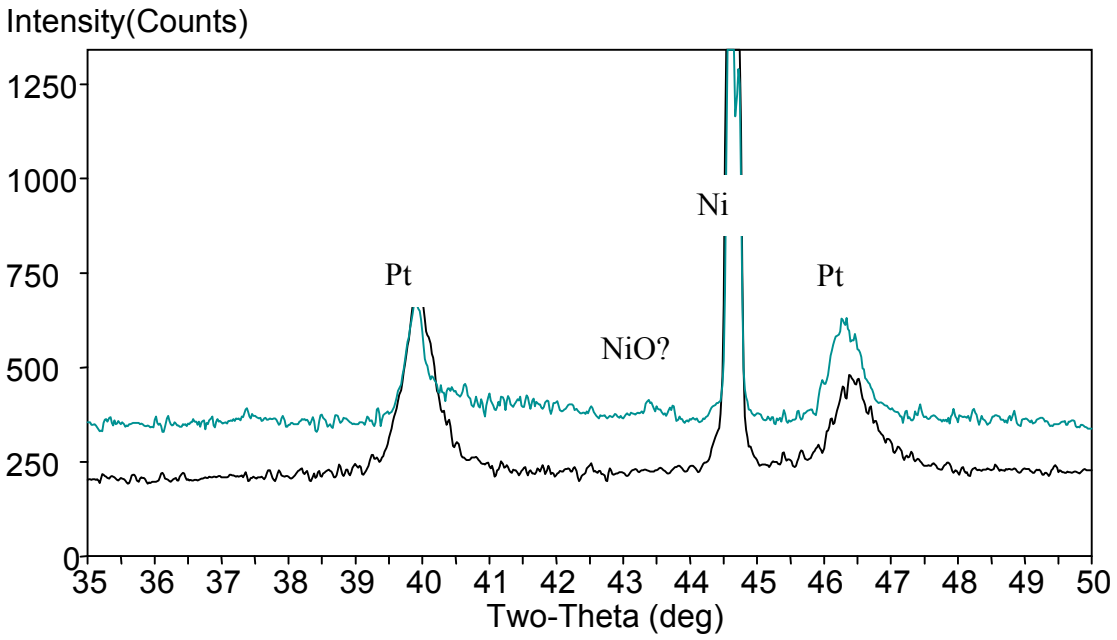

Figure 6-13: x-ray data of platinized Ni foils heated to 400 and 600^{0}C

have some NiO present. There was no visual color change on any foils. In order to determine with more accuracy the presence of NiO, spectroscopic ellipsometry was also performed on the two samples in order to compare with the results obtained from

the unplatinized samples. The raw data are presented in Figure 6-14 . From the raw data, there is no obvious oxidation occurring at 350 °C or 400 °C. In contrast, for 400 °C on the unplatinized foils (Figure 6-10) there is obvious oxidation taking place. The raw data of foils heated at 600 °C show clear evidence for oxidation on the platinized foils. Thus, it is clear that the Pt coating successfully delays oxidation of the Ni, and so may be useful as a barrier layer for PZT deposition on Ni.

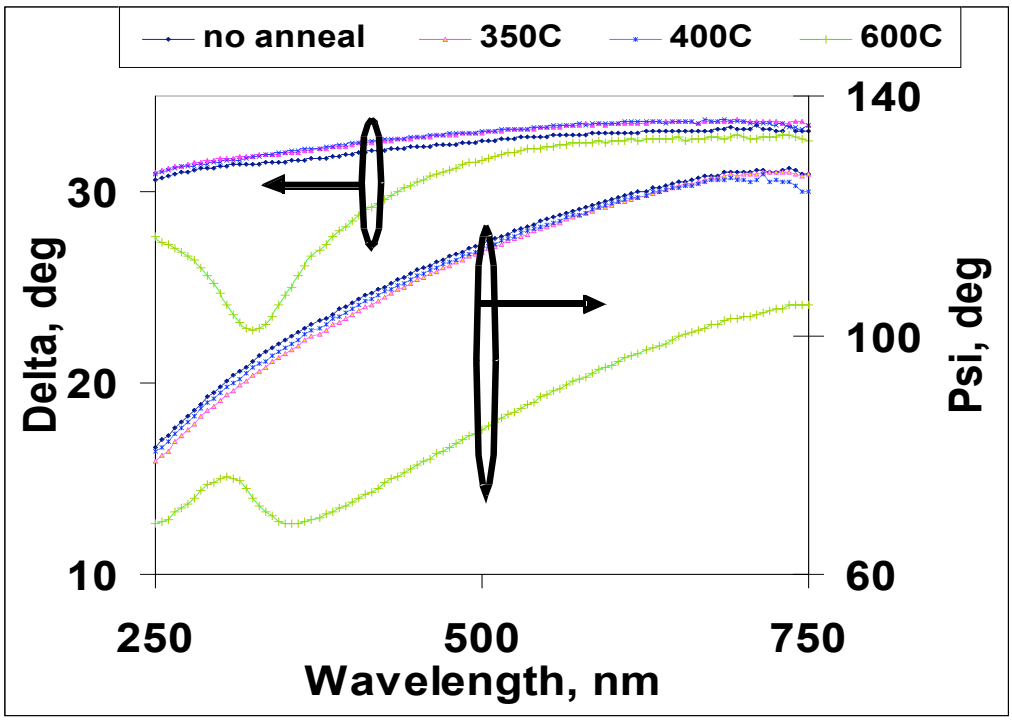

Figure 6- 14: Raw data from ellipsometry measurements on platinized foils which were: unheated, heated at 350 °C - 600 °C. Data were taken by Tanawadee Dechakupt.

6.2.5 PZT Films on Ni Foils

6.2.5.1 Films on Unplatinized Ni Foils

In order to establish a starting point for the Ni oxidation of a *coated* substrate, PZT films were deposited on Ni foils using the same conditions as the films made on

platinum coated silicon wafers. A 10% Pb excess PZT solution was used to prepare a 0.2 micron thick PZT film. The first pyrolysis was done at 250 °C on a hot plate, the second pyrolysis was done at 350 °C, and crystallization at 700°C in an RTA. The conditions for the heat treatment of each sample are shown in Table 6- 3.

Table 6- 3: Conditions for heat treatment of PZT on 99% purity Ni foils

	2nd Pyrolysis		**Crystallization**	
	Temp, °C	**N_2, slpm**	**Temp, °C**	**N_2, slpm**
A	350, 1min	Air	700	Air
B	350, 1min	Air	700	5
C	350, 1min	2	700	2
D	350, 1min	5	700	5
E	350, 1min	20	700	20

An X-ray scan was taken from 20° to 60° 2Θ at a rate of 2Θ/min to determine the bracket of conditions at which the best PZT is formed, with the least interaction of the substrate with the environment. It was noticed that films heated in low Po_2 turned black. From the x-ray diffraction patterns in Figure 6-15 it can be determined that Pb formed when the films were heated in N_2. These results agree with the phase diagram (See Figure 6-2) in that low P_{O2} should favor Pb reduction.

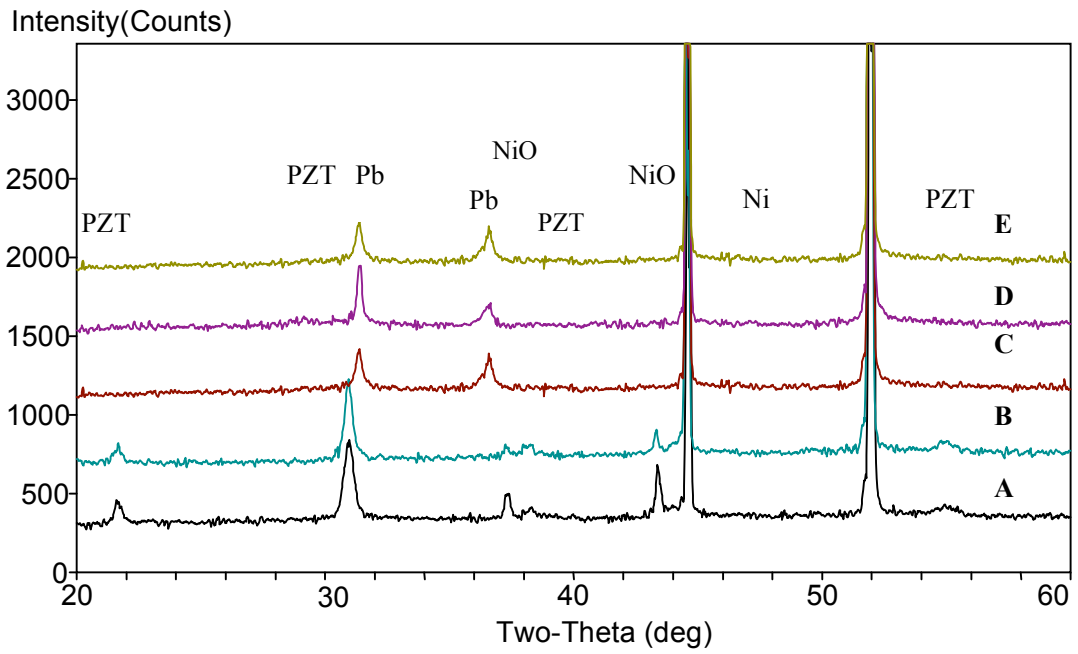

Figure 6-15: X-ray diffraction patterns for 0.2 µm PZT films on 99% purity Ni foils annealed at 700°C

6.2.5.1.1 Presence of Metallic Lead

Because the x-ray data of films that were crystallized at low Po_2 showed the presence of metallic lead, the origin of the reduction was investigated. A 0.2 µm thick film of PZT was deposited on a 99% Ni foils using the same conditions. The foil was then taken through the first pyrolysis at 250 °C in air and second pyrolysis at 350 °C at 2 slpm of nitrogen. No crystallization was done on the sample. An x-ray diffraction pattern was then taken to search for the presence of the lead peak. The results of the control experiment to determine at which step the lead is formed are shown in Figure 6-16. From this data it can be deduced that the formation of lead is initiated during the second pyrolysis step.

Because the N_2 atmosphere during the heat treatment cannot be the cause of such a low partial pressure of O_2 that it would reduce Pb, it is believed that the local pO_2 is reduced by volatilization of organics from the film.

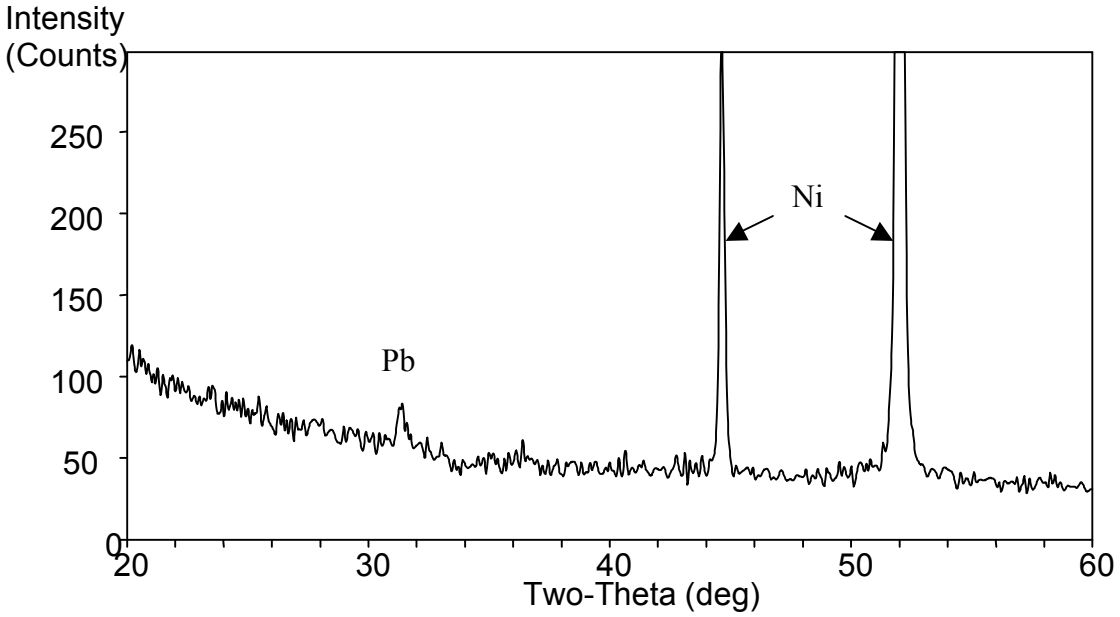

Figure 6-16: X-ray pattern of PZT film on Ni. After the second pyrolysis step at 350 ^{o} C metallic Pb is formed.

During the pyrolysis steps, the film contains many unburned and partially burned organics that could absorb oxygen, reducing locally the partial pressure of oxygen. In an attempt to decrease the formation of Pb during the crystallization process of PZT, a longer pyrolysis step to more completely remove residual organics was incorporated into the subsequent experiments.

6.2.5.1.2 PZT Films on Ni Foils with Longer Pyrolysis Time

After the confirmation of lead formation during the pyrolysis, more films were deposited on 99% Ni foils and again they were treated at different conditions to determine if that improved the crystallinity of PZT without increasing the amount of NiO. This time tighter bounds of nitrogen conditions were used, as the previous experiment showed that a lower flow of nitrogen was preferable. The nitrogen flow rate was limited to less than or equal to 3 slpm. The crystallization temperature was also

lowered, since PZT can be crystallized at the lower temperature of 600 °C. This can also minimize NiO formation. PZT films with an approximate thickness of 0.2 μm were used in this experiment. The first pyrolysis was done in air at 250°C, the second pyrolysis and crystallization conditions are shown in Table 6- 4.

Table 6- 4: Heat treatment conditions of Ni foils with PZT films with increased pyrolysis time

	2nd Pyrolysis		**Crystallization**	
	Temp, °C	**N_2, slpm**	**Temp, °C**	**N_2, slpm**
A	350, 2min	1	600	1
B	350, 2min	2	600	2
C	350, 2min	3	600	3

It was found that the best conditions appear to be when the Po_2 during the pyrolysis is higher, and lower during the crystallization. Longer anneal times on the second pyrolysis decreased the lead formation below the detectible limits of the x-ray diffraction equipment. The data from the x-ray are shown in Figure 6-17 . Although the size of the NiO peaks decreased as the amount of N_2 flown through the system increased, the crystallinity of the PZT generally degraded at the same time. It is encouraging that no Pb seems to develop under these heat treatment conditions.

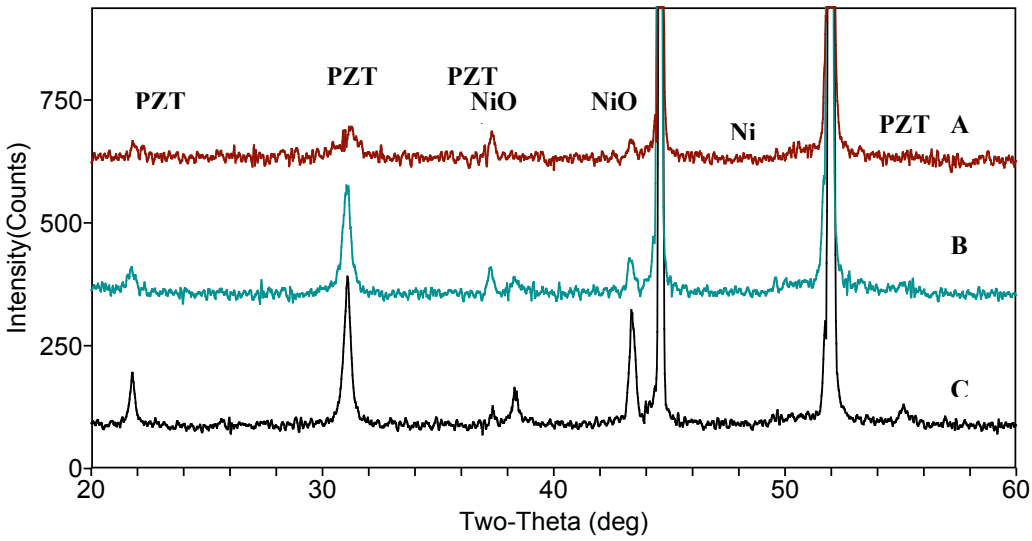

Figure 6- 17: X-ray of PZT films on Ni foils with second pyrolysis time of two minutes.

6.2.5.2 PZT Films on Plated Ni Foils

In order to test the hypothesis that a Pt layer will reduce oxidation of Ni during the co-processing with PZT, PZT films were deposited on Ni foils that had been plated with Pt. Figure 6-18 shows an x-ray pattern of such a film. The film was crystallized in air at 670 °C, and it seems that the Ni on the foil was partially oxidized during this experiment. However, the ratio of the NiO/PZT peaks seems to have improved in comparison to the films crystallized in air in Figure 6-15 without the Pt passivation layer. It is possible that some of the oxidation can be attributed to the small thickness of the Pt layer.

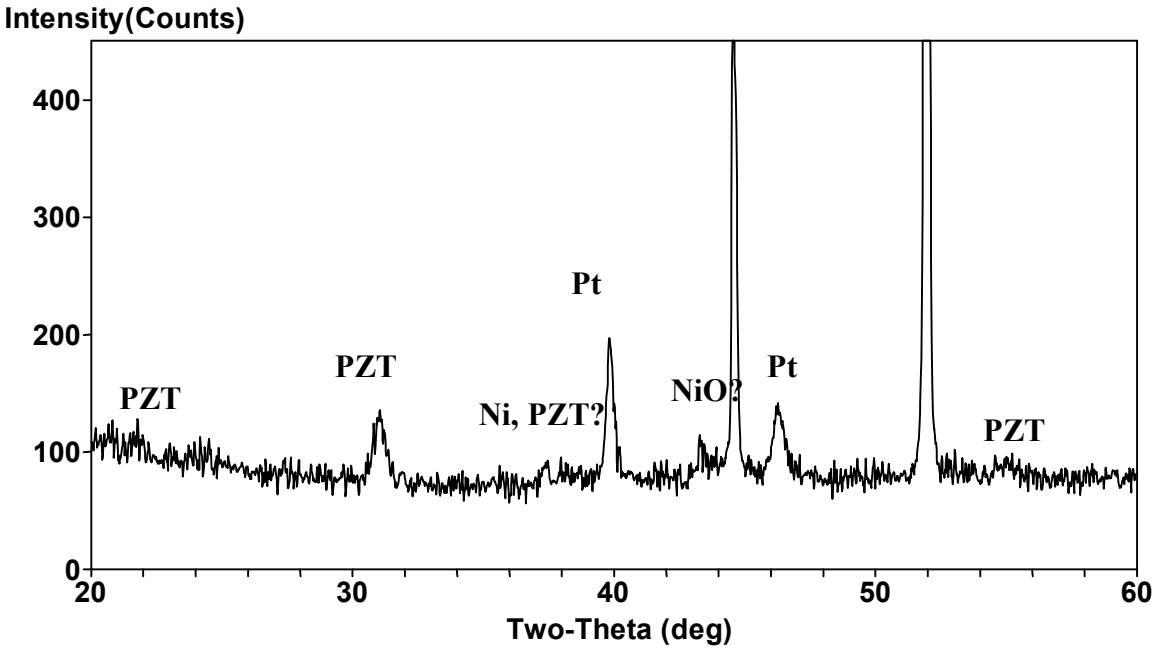

Figure 6-18: Ni/Pt/PZT film crystallized at 670 °C in air.

6.2.5.3 PZT Film on Ni Foils with Plated and Sputtered Pt

In order to further improve protection of the Ni from oxidation, a sputtering step was added into the process. For this experiment the 99.994% purity Ni foils were used. The Ni was cleaned and treated with N_2H_4 to remove the native oxide. The Ni was then plated with Pt at 60°C for 15-20 min. When all of the foil's surface appeared to be covered with Pt, the foils were washed with deionized water and were placed on a hot plate at 250 °C for 1 min. The foils were then sputtered with ~200 Å of Pt in order to increase the Pt thickness. The sputtering was performed in a Kurt J. Lesker sputtering system at 2.5 mTorr Ar gas and 200W power. Two layers of 0.75M PZT solution were then spin-coated onto the surface of the foil with an intermediate 200°C pyrolysis step in air between each layer. The foils were then pyrolyzed and crystallized at different conditions in the RTA. The schedule of the heat treatments is shown in Table 6- 5. Two

minute pyrolysis conditions were used in order to avoid lead formation. A 600 °C crystallization step was used to minimize Ni oxidation. The bounds of the N_2 flow rate explored, as determined from the previous experiments, were narrow: between 0-2 slpm for pyrolysis and 5-8 slpm for crystallization. X-ray data were taken from the three foils and the phases present were determined using Jade 8.

Table 6- 5: Heat treatment conditions of PZT films on Ni/Pt/Pt foils.

	2nd Pyrolysis		**Crystallization**	
	Temp, °C	**N_2, slpm**	**Temp, °C**	**N_2, slpm**
A	350, 2min	Air	600	5
B	350, 2min	1	600	7
C	350, 2min	2	600	8

All the films that were pyrolyzed in N_2 turned black after the second pyrolysis step. Foil B regained its color after the crystallization step; foil C remained black. As can be seen in Figure 6-19, foil A shows crystallized PZT without any second phases. Foil B shows crystalline PZT and Pt, (however, they are not as well crystallized as in Foil A) and it also shows peaks 1, 2, 4, and 5. The possible compounds for those peaks are shown in Table 6- 6. Foil C does not seem to contain any substantial amounts of PZT perovskite or Pt, and contains a variety of other compositions. The possible compounds are listed in Table 6- 6. From this data it can be concluded that foil A has the best phase purity of any PZT film on Ni foil investigated here.

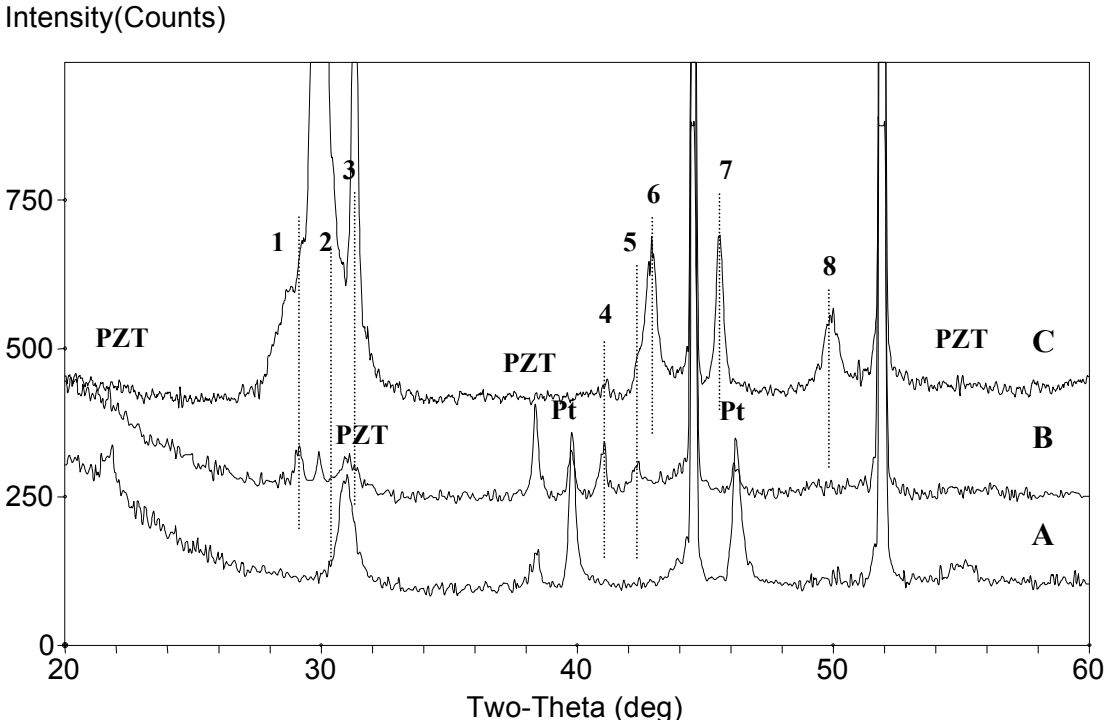

Figure 6-19: X-ray diffraction pattern of Ni/Pt/PZT foils heat treated under various conditions

Table 6- 6: Possible compounds present in Ni/Pt/PZT samples from Figure 6-19

Peak	Possible compounds
1	PtPb
2	?
3	Pb
4	Ni_2Ti, PbPt
5	PbPt, PbO
6	$Ni_{0.75}Pt_{0.25}$, NiTi
7	PbO
8	$Ni_{0.75}Pt_{0.25}$

6.2.6 Transmission Electron Microscopy (TEM)

In order to analyze the Ni/Pt/PZT film for presence of NiO and to look at the microstructure and interfaces of the layers, TEM analysis was performed on sample A, the sample that had been pyrolyzed in air and crystallized under low amounts of nitrogen. The sample was first thinned down to 100nm using a Fischione focused ion beam using Ga at 30kV. The analysis was then performed in a JEOL 2010F TEM at 200 kV. EDX and diffraction spectra were taken from various regions in the sample to determine the phases of the layers and the interfaces.

An image of the sample is shown in Figure 6-20. The top layer is the conductive layer that was deposited on the sample prior to the thinning, it consists of 100Å of Au and 100Å of C. The layer below that is PZT. This layer was partially amorphized during the milling of the sample, especially near the surface; the rest of the PZT looks polycrystalline. The fact that the PZT amorphized at the top surface means that the milling voltage was too high. Below the PZT layer is the Pt that was plated and sputtered. The bottom most layer is the Ni foil substrate.

The grain size of the PZT appears to be on the order of ~80nm in size and is blocky, rather than columnar in microstructure. The upper ~80nm of the PZT layer has been amorphized by the milling, the remaining of the layer, however seems to be still crystalline. There is no obvious reaction layer at the Pt-PZT interface.

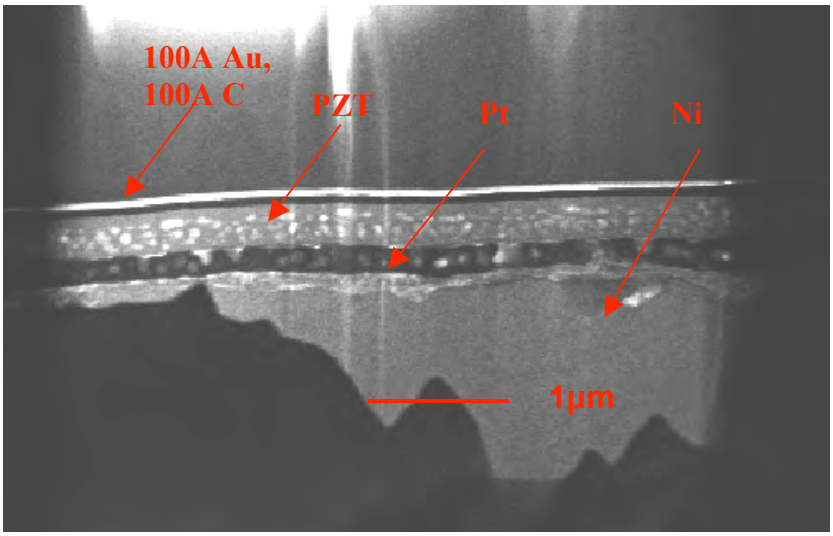

Figure 6-20: TEM image of the a PZT film on a Pt-coated Ni foil

The quality of the interfaces was also investigated by collecting diffraction patterns from the PZT/Pt and the Pt/Ni interfaces. The diffraction data were taken with a camera length of 250mm at 200KV accelerating voltage of the beam. The diffraction data from the Ni foil show only evidence of FCC Ni. All of the diffraction spots from the data collected at the Pt/PZT interface correspond to either perovskite PZT or Pt. If the NiO rings were overlaid onto the diffraction pattern the 111 and the 220 peaks were absent, which suggests that no NiO is present at the interface. This is in agreement with the X-ray diffraction experiments, which showed no NiO on these samples.

Close examination of Figure 6-20 and Figure 6- 21 reveals that there is another layer present between the Pt and the Ni layer that is of lighter color than Ni. However, the electron diffraction patterns from that region were consistent with Ni.

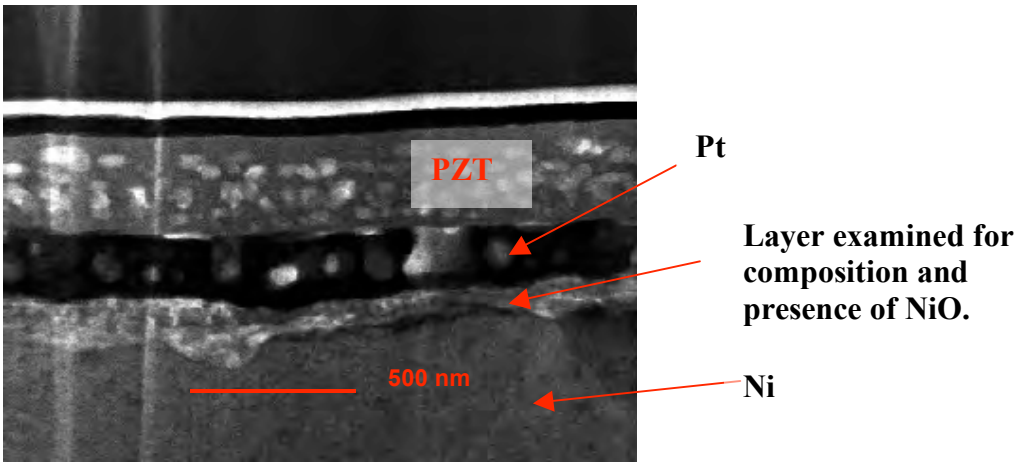

Figure 6-21: Higher magnification TEM image of the layers. The PZT, the Ni, the Pt and the layer under study are shown

In conclusion, it appears that the interfaces of the PZT/PT and PT/Ni do not contain secondary phases, and electroless deposition of Pt can help avoid Ni oxidation, by acting as a barrier layer for the between Ni and the oxidizing air, and it can be used as the bottom electrode of the PZT films. The structures that appear inside the Ni and Pt phases in different color may be due to the lower density material that formed as a result of plating.

6.3 Conclusions

It would be valuable to be able to produce PZT films on Ni electrodes, since Ni electroplating enables very high aspect ratio structures of interest for high frequency ultrasound transducers. However, the propensity for Ni to oxidize at high temperatures at moderate Po_2 requires use of low P_{O2} crystallization conditions that reduce Pb from the PZT. On the phase diagram in Figure 6- 2, the boundaries marking the Ni/NiO and Pb/PbO equilibria clearly show no overlap between the two systems. Thus, it would be thermodynamically impossible for PbO and Ni to coexist.

It was found that Pt-coating of Ni foils enabled deposition of phase pure PZT films on Ni without extensive NiO formation. The best PZT processing conditions occurred when the partial pressure of oxygen is high during the second pyrolysis in order to facilitate removal of the organics. Lower P_{O2} was employed during the crystallization. Under these conditions, a PZT film was successfully deposited onto a platinized nickel foil without the appearance of NiO within the detection limits of the x-ray diffraction equipment.

The results were confirmed through TEM analysis of the film. The analysis has shown that the interfaces of the PZT/PT and PT/Ni do not contain secondary phases, and electroless deposition of Pt can help avoid the Ni oxidation problem, by acting as a barrier layer for the between Ni and the oxidizing air, and it can be used as the bottom electrode of the PZT films.

References

1 H. Kishi, Y. Mizuno, and H. Chazono, Japanese Journal of Applied Physics **42,** 1-15 (2003).

2 T. Jackson, (2006).

3 M. D. Losego, MS Thesis, North Carolina State University, 2005.

4 I. G. Mina, Thesis (B.S.) Thesis, Pennsylvania State University, 2004.

5 Y.-H. You, B.-S. So, J.-H. Hwang, W. Cho, S. S. Lee, T.-M. Chung, C. G. Kim, and K.-S. An, Applied Physics Letters **89,** 222105 (2006).

6 Y. Tsur, J. Adair, and C. Randall, Japanese Journal of Applied Physics **39,** 6004-7 (2000).

7 A. Bencan, G. Dravic, M. Hrovat, J. Holc, and M. Kosec, Journal of Materials Science **38,** 3769-74 (2003).

8 H. Wang, C. Cao, and W. B., Chinese Scienec Bulletin **49,** 220-224 (2004).

9 http://www.metallurgy.nist.gov/phase/solder/cupb.html, (Metallurgy Dividion, NIST, 2003).

10 A. I. Kingon and S. Srinivasan, Nature Materials **4,** 233-8 (2005).

11 Q. Zou, H. E. Ruda, B. G. Yacobi, K. Saegusa, and M. Farrell, Applied Physics Letters **77,** 1038-41 (2000).

[12] T. Kim, A. I. Kingon, J.-p. Maria, and R. T. Croswell, Journal of the American Ceramic Society **89,** 3426-3430 (2006).
[13] T. Suzuki, I. Kanno, J. J. Loverich, H. Kotera, and K. Wasa, Sensors and Actuators A: Physical **125,** 382-386 (2006).
[14] J. Cheng, L. He, S. Yu, and Z. Meng, Applied Physics Letters **88** (2006).
[15] J.-R. Cheng, W. Zhu, N. Li, and E. L. Cross, Applied Physics Letters **81,** 4805-4807 (2002).
[16] S. Baba, J. Akedo, M. Tsukamoto, and N. Abe, Journal of the American Ceramic Society **89,** 1736-1738 (2006).
[17] A. Daunois and D. E. Aspnes, Physical Review B **18,** 1824 (1978).
[18] R. W. Whatmore, Reports on Progress in Physics **49** (1986).

7 Conclusions and Future Work

7.1 Conclusions

High frequency ultrasound devices in the 50 MHz-1 GHz range can be used for imaging tissues such as the eye or skin, as well as for nondestructive evaluation of microelectronic devices. This work is concerned with fabricating such a high frequency piezoelectric transducer arrays using thin film processing techniques in order to reduce the driving voltage, which would enable the device to be integratable with a CMOS chip

Both one and two dimensional arrays were investigated. The geometry utilized for one dimensional transducer arrays is a comb - like structure. This is a layered structure of the dielectric layer (SiO_2), the sputtered Ti/Pt bottom electrodes, PZT, and finally the top electrode. The PZT for this structure is deposited by spin-coating a 2-Methoxyethanol based solution. After patterning the wafer to define the high aspect ratio structures, and creating the vias to contact the bottom electrodes to large contact pads, the structures are partially released from the underlying substrate by etching to form a T-bar shaped transducer. The dielectric properties measured on the device show a dielectric constant of 800-1500 at 1KHz. The measured hysteresis loop shows values of polarization to be P_r^+~23.5 μC/cm^2, P_r^-~36 μC/cm^2, and the coercive field E_c^+~60 kV/cm, E_c^-~37 kV/cm. Both finite element modeling and experimental data have shown that the impedance signature of the resonance of such structures is too small and too broad to be detected using an impedance analyzer. Pulse echo measurements on the first generation transducers were complicated by poor quality electrical leads which did not carry large currents at high frequency.

The two dimensional prototype consisted of either tube structures or post structures. In order to isolate the needed resonance mode the structures were designed to be high aspect ratio structures. The tube structures were fabricated using vacuum assisted infiltration of PZT and electrode solutions into a silicon mold. In order to improve the mechanical stability of the structures and to simplify the individual element top/bottom contact the design evolved into the post structures. This device consisted of metal posts on a Si substrate which were coated with the piezoelectric material. In order to fabricate the high aspect ratio inner electrodes, SU-8 resist was patterned to create a mold into which Ni was electroplated. The resulting pillars were about 40 μm in height and 10 μm in diameter with a 15μm pitch. The metal cores act as the inner electrodes and are addressed via electrical interconnects on the substrate. $PbZr_{0.52}Ti_{0.48}O_3$ (PZT) was chosen as the driving material, and was deposited using mist deposition. Because, the thermodynamics does not allow for co-processing of PZT on Ni due to formation of NiO and Pb there was a need to develop a technique to overcome this.

In order to achieve high quality crystalline PZT on Ni pillars, the processing conditions which minimize of the formation of NiO or Pb were investigated. For this purpose Ni foils were coated with a Pt barrier layers using electroless deposition and sputtering. The optimum heat treatment conditions for crystallization of PZT on the Ni/Pt substrates were investigated. It was found that use of a 100 nm thick Pt passivation layer on the Ni enabled perovskite PZT films to be deposited without second phases, as determined by X-ray diffraction and transmission electron microscopy.

The processing procedures developed in this thesis enable the creation of very high aspect ratio piezoelectric structures with fine pitches. A much wider range of

geometries can be obtained using this approach than can be achieved using available techniques for patterning bulk piezoelectric ceramics or single crystals. Thus, it is expected that the general approach presented here could be enable preparation of a wide variety of piezoelectric sensors and actuators that have heretofore been difficult to fabricate.

7.2 Future Work

One of the key elements of future work would be to demonstrate pulse-echo responses for the thin film array transducers. There are several avenues that should be pursued here. First, it would be very interesting to look at the transmit and receive functions of the MEMS transducer separately using a bulk single element transducer as a reference. It is suggested that the experiment be set up in water in such a way that at least one of the transducers can be moved in a controlled fashion. In this way the distance between hydrophone and the projector can be manipulated to see the shift in the time domain of the response signal.

It would also be important to increase the field level at which the MEMS transducers can be driven at high frequencies. Because the traces running from the voltage source to the transducer failed during the impedance measurement at 0.5 V, all the measurements had to be done at 5mV. This greatly decreased the amplitude of the motion expected. A new transducer should be fabricated with lower resistance electrodes with high current carrying capabilities. This can be done by masking with a resist all the area of the device except the metal wiring and plating metal onto the existing traces.

Of the two proposed two-dimensional array fabrication strategies, the post arrays appear to be superior for ultrasonic array applications. It is recommended that the Pt plating process developed for Ni foils be implemented on the post arrays. The imaging behavior of such transducers should then be compared to the 1D arrays.

For both 1D and 2D arrays, after imaging is demonstrated, the next important step would be to do in-vitro and finally in-vivo imaging on small animals for testing. The resulting parameters can the compared to the modeled results.

There are several areas in which additional materials characterization should be performed. In particular, additional TEM specimens for PZT films on Ni foils should be prepared. Of particular interest would be an investigation of the oxygen stoichiometry near the Pt/PZT interface, as well as the possibility of any lead diffusion into the electrode.

Further, in this thesis, no electrical measurements of PZT films on passivated Ni foils were made, because of a combination of rough foil surfaces and PZT film cracking. The cracking is probably caused due to the incomplete burn out of the organics during the pyrolysis and the thermal expansion mismatch of the substrate with the film. A study to optimize the pyrolysis conditions for these samples should be undertaken. These conditions will also need to avoid oxidation of the Ni and reduction of the lead in the PZT.

Appendix A

FEA Xylophones (Dimensions)

Longitudinal wave velocity (m/s)	1524
Frequency (MHz)	50
Number of elements	9
Water thickness (mm)	2
Width of Si backing (microns)	36
Width of PZT (microns)	10
Width SiO_2 post (microns)	8
Length (microns)	300
Ti Thickness (microns)	0.03
Platinum Bottom Thickness (microns)	0.1
Platinum Top Thickness (microns)	0.1

FEA Posts (Dimensions)

Longitudinal wave velocity (m/s)	1524
Frequency (MHz)	50
Matching Layer Thickness (μm)	12
Ceramic Thickness (μm)	41
Outer Diameter microns	10
Inner Diameter microns	8
Wall Thickness Micron	1

Constants Used for FEA

K^s_{33}	1310
K^s_{31}	1200
Density Kg/m^3	7820
Mech. Q at 1MHz	90

Stiffness coefficients (Pa)	
c11	1.37×10^{11}
c33	1.26×10^{11}
c44	2.23×10^{10}
c12	8.79×10^{10}
c13	9.23×10^{10}

Piezoelectric stress Coefficient C/m^2	
e_{15}	16.054
e_{31}	-9.44
e_{33}	22.495

	Bulk Modulus (Pa)	**Sheer Modulus (Pa)**
Pt	230×10^9	61×10^9
Ti	1.10×10^{11}	4.40×10^{10}
Cr	1.60×10^{11}	1.15×10^{11}
SiO_2	4.10×10^{10}	3.10×10^{10}
SiN_x	3.15×10^{11}	1.19×10^{11}

	Density (Kg/m$^{2)}$	**Speed of sound (m/s)**
Stainless steel	7900	5790
parylene	1289	2306
SU 8	1190	1940
Si	2330	2200
Matching Layer	2600	2800
Polymer	1200	2565
Water	1000	1500